UNIVERSITÄT GÖTTINGEN
FAKULTÄT FÜR PHYSIK

PHYSICS MASTER OF SCIENCE

MASTER THESIS IN
BIOPHYSICS/COMPLEX SYSTEMS

MESOSCALE MODELING OF ACTIVE NEMATICS

Joscha Tabet

`joscha.tabet@stud.uni-goettingen.de`

`matriculation number: 21228376`

Supervisor:	Dr. Marco G. Mazza
Second assessor:	PD Dr. Salvatore R. Manmana

February 18, 2019

Max-Planck-Institute for
Dynamics and Self-Organization

Department Dynamics of
Complex Fluids

Nonequilibrium
Soft Matter

NESM

Abstract

Nematic liquid crystals are fluids whose anisotropic molecules have long range orientational order, but no positional order. When the particles are driven by some chemical or biological mechanism, the system is called active. The energy supplied at the microscopic scale is transformed into organized motion at the large scale. The coupling of the orientation field to the hydrodynamic and active forces leads to rich, dynamical behaviors. We develop a framework for simulating such active liquid crystals, based on the multiparticle collision dynamics algorithm for hydrodynamics. The solver captures thermal fluctuations, is highly tunable, and suited for complex boundary conditions. It is successfully validated against analytical and numerical results of the isotropic-nematic phase transition, defect annihilation, and activity. We use it to study the behavior of an active NLC in cylindrical confinement, as well as in a deformed capillary with an elliptical cross-section. Applying four different types of boundary conditions across a wide range of activity magnitudes, we find a new non-equilibrium steady state. It is characterized by two disclination lines orbiting the capillary center in ellipses of varying aspect ratios. We find large asymmetries between extensile and contractile active stresses for all steady states. The results are discussed in the context of current research.

Contents

Symbols

X	scalar quantity
$\mathbf{X}$	vector quantity
$\boldsymbol{X}$	tensor or matrix quantity
$\boldsymbol{X}^T$	transpose of a matrix
$\hat{\mathbf{e}}$	unit vector
X_i	vector in index notation; summation over repeated indices
$X_{i,j}$	partial derivative $X_{i,j} \equiv \partial_j X_i \equiv \partial X_i / \partial r_j$
ϵ_{ijk}	Levi-Civita symbol
$\frac{\mathrm{d}}{\mathrm{d}t}$	material derivative $\frac{\mathrm{d}}{\mathrm{d}t} \equiv \frac{\partial}{\partial t} + \mathbf{v} \cdot \nabla$
$\langle X \rangle$	mean of quantity X
$\otimes$	dyadic product (implied for the gradient $\boldsymbol{\nabla}\mathbf{X}$)
$\equiv$	defined as
S_2	the 2-sphere
t	time coordinate
$\mathbf{r}$	position vector $\mathbf{r} = (x, y, z)^T$
$\mathbf{v}$	convective velocity field
ρ	density
p	pressure
T	temperature
F	free energy density
k_{B}	Boltzmann constant
$\mathbf{n}$	local director of a nematic liquid crystal
$\boldsymbol{Q}$	local order parameter of a nematic liquid crystal
S	local scalar order parameter of a nematic liquid crystal
Δt	small discrete time step
$\mathbf{r}_i$	position of particle i
$\mathbf{v}_i$	velocity of particle i
$\mathbf{v}^\alpha$	center of mass velocity of cell α

Abbreviations

LC	liquid crystal
NLC	nematic liquid crystal
MPCD	multiparticle collision dynamics
SRD	stochastic rotation dynamics
ATP	adenosine-triphosphate

Chapter 1

Introduction

In between liquids and solids there exists another state of matter, the liquid crystal (LC). Of particular interest are LCs consisting of rigid, rod-like molecules. Like liquids, they have no long-range positional order. However, their molecules tend to align parallel to each other. The degree of alignment, quantified by the scalar order parameter S, depends on the temperature and material properties. Given a low enough temperature, many LCs enter the nematic phase. A dominant local director emerges, that molecule orientations are distributed around, closely. It has the distinctive feature that it does not define a direction, but an axis with arbitrary sign. This sets it topologically apart from ordinary vector fields. When a phase transition occurs, the director field develops singularities. Elastic forces within the nematic liquid crystal (NLC) seek to smooth the field and rectify these defects. However, the boundaries may impose topological constraints that guarantee their continued existence. In this way, the elastic forces come in conflict with the boundaries and find a high-energy equilibrium. When the particles are driven by some chemical or biological mechanism, the system is called active. The energy supplied at the microscopic scale is transformed into organized motion at the large scale, and acts mostly on the regions surrounding defects. In this thesis we study such systems and find that their symmetries may not allow for the existence of equilibria. Instead we discover an oscillating steady state. Similar observations have been made in experiments with different topological constraints [1].

The mathematical models describing these active NLCs reach far beyond molecular media. Many systems with similar ordering interactions behave in the same way. Examples include mixtures of cytoskeletal filaments and associated motor proteins [2] (see section 2.1), bacterial suspensions [3], and monolayers of vibrated granular rods [4]. These active systems experience phenomena, such as spontaneous flow [5,6], large density fluctuations [7], self-organization [8,9], and low Reynolds number turbulence [10,11].

The additional degrees of freedom, relating to the molecules' orientations make molecular dynamics simulations unfeasible at the length scale of microns or larger. To simulate NLCs at the mesoscopic scale we, instead, employ a modified version of the multiparticle collision dynamics (MPCD) algorithm. It uses a bottom-up approach to reproduce hydrodynamics, and we extended it to include the additional interactions present in NLCs.

We start the thesis by giving biological background information, and motivating the study of active NLCs (section 2.1). Chapter 2 continues with a detailed characterization of the NLC, and an investigation of its properties. After presenting a theory of nematic elasticity and its interplay with topology, we discuss the significance of topological defects, in both passive, and active systems. We examine the isotropic-nematic phase transition from multiple points of view. Much attention is given to the derivation of a model of 'nematodynamics', the branch of hydrodynamics describing the flow of NLCs. The chapter concludes with a review of how activity in nematic systems is treated in current research. In chapter 3, we present the MPCD algorithm, and our adaptation that models active NLCs. We employ it, to explore the behavior of a NLC confined to a cylindrical pore (chapter 4). The dynamics are heavily influenced by the boundary conditions, for which our algorithm offers high flexibility. Our study includes parameter regimes, that have been studied in the recent literature. This allows us to verify the validity of our model. Beyond that, we examined systems with tilted director anchoring. A configuration, that has not been studied in this context. In our simulations, this confinement causes the NLC to enter a non-equilibrium steady state. The disclination lines enforced by the boundary perform orbits around the capillary center at a tunable frequency. Properties, such as aspect ratio, and dispersion of the trajectories vary, depending on the activity parameter. Finally, we discuss these results and give an outlook in chapters 5 and 6.

Chapter 2

Theoretical Background

"The cytoplasm, the substratum of life, is the most extraordinary substance we know."

— Albert Frey-Wyssling

2.1 Biological Motivation

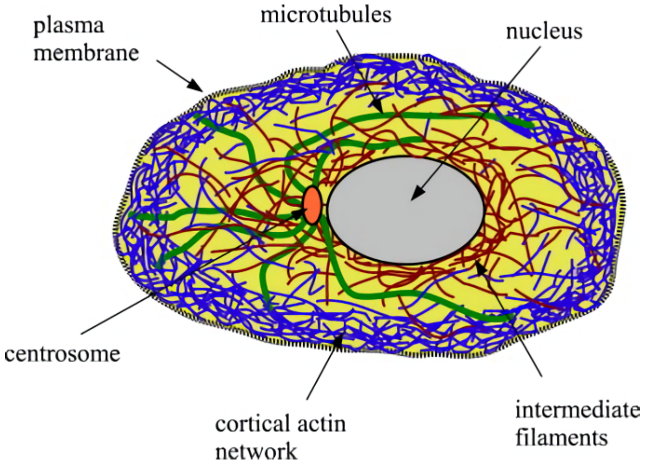

Figure 2.1: Schematic depiction of the cytoskeleton's arrangement within a eukaryotic cell. The cell cortex (or actin cortex) is especially visible with the blue filaments densely packed on the inner side of the plasma membrane. Image credits: [12].

A very important setting where LC physics plays a key role is the cytoskeleton, which is formed by a network of rigid molecules immersed in the cytoplasm. The cytoplasm is a gel-like substance that makes up all of the cell's content, except for the nucleus. It has important elastic properties and behaves in many respects like a non-Newtonian fluid [13]. In this way its viscosity depends not only on

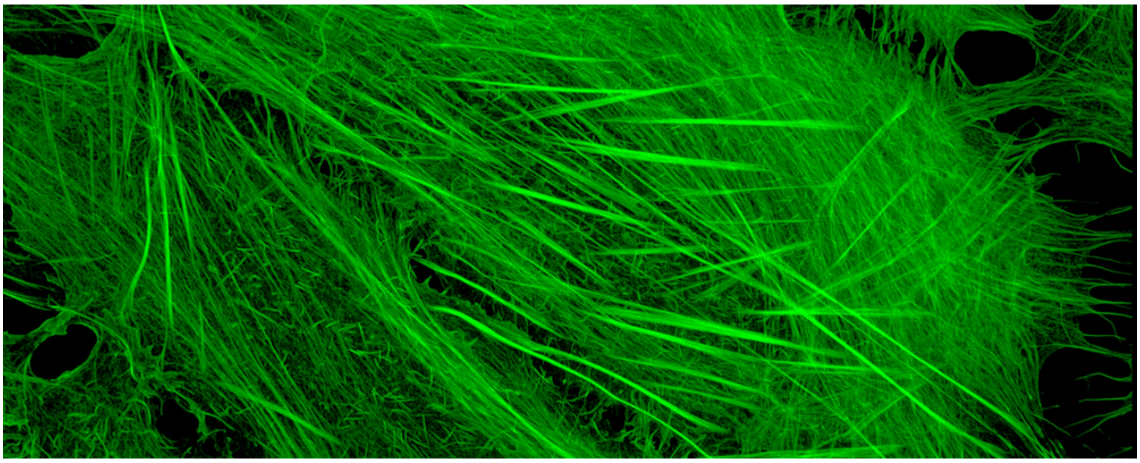

Figure 2.2: Confocal microscope image of the actin filaments within a cancer cell, stained with a fluorescent peptide.[1]

the temperature, but also on the gradient of the flow rate (structural viscosity). Experiments have shown that Stokes' law for the frictional force does not apply in the cytoplasm [14]. Small, passive particles in a constant force field do not reach a terminal velocity. Instead, their movement is erratic. Furthermore, the cytoplasm is anomalous in its optical properties. It is anisotropic and displays double refraction under certain conditions [15, 16].

Since it includes the cell substance and the organelles (apart from the nucleus) a comprehensive model of the cytoplasm is still out of reach. One of its most intriguing constituents is the cytoskeleton, a network of linked microfilaments and microtubules, that connects the organelles and gives the cell its structure and shape [17]. Figure 2.1 shows the organization of the cytoskeleton inside a cell. Depending on the type of cell, the cytoskeleton's function and behavior change radically [18]. Rapid disassembly and recomposition of actin and tubulin, the proteins that make up most of the cytoskeleton, allow for arbitrary deformations of the cell. This mechanism enables muscle contraction [19] and cell motility [20]. The cytoskeleton is also involved in extracellular transport [21], intracellular transport, cellular division [17], and cytokinesis [18].

Of these functions the deformative, mechanical aspect is the most independent, making it one of the cell's features that is more accessible to physics. The actin filaments and tubulin microtubules can be considered flexible, but strong rods, as figure 2.2 illustrates. In addition to the aforementioned treadmilling (disassembly on one end and reassembly at the other) the filaments and microtubules are driven by kinesin, a molecular motor that is fueled by ATP (adenosine triphosphate) and moves along the tubules [22]. Kinesin clusters may bind to two neighboring microtubules and induce sliding forces between them, if they move in opposite directions, i.e. have opposite polarity [23, 24]. Actin filaments and the tubulin

---

[1] Image credits: Howard Vindin `https://commons.wikimedia.org/wiki/File:Phalloidin_staining_of_actin_filaments.tif`, retrieved on 2018-06-04

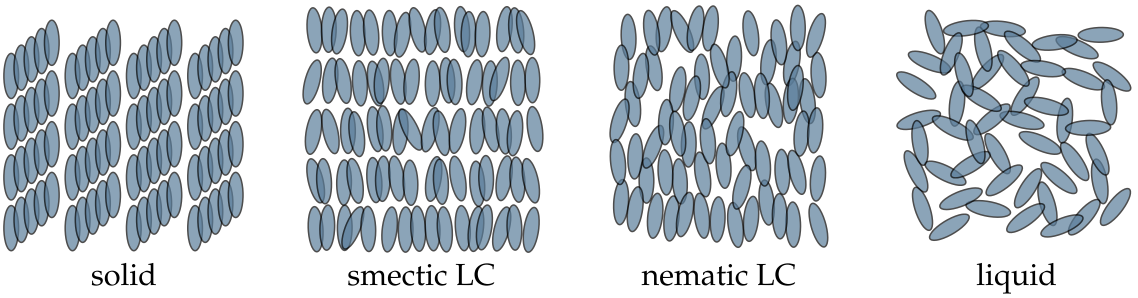

Figure 2.3: Schematic representation of the thermodynamic phases an anisotropic material may go through at low temperatures.

microtubules form a system that behaves in many ways like an active NLC. Therefore, a better understanding of active nematics could advance the physical model of the cell.

2.2 Nematic Liquid Crystals

Many organic materials are composed of molecules with rigid cores, and large aspect ratios, having for example, prolate (rod-like) or oblate (disc-like) shapes. It is observed that these kinds of substances exhibit different, intermediate (mesomorphic) phases during a thermodynamic transition from the solid state to the disordered liquid.

In crystalline solids the composing molecules are arranged on a regular lattice. The thermodynamic phase is characterized by a long-range three-dimensional order of position and orientation. For molecules with large aspect ratios there exists a temperature range at which the particles are packed densely enough to make steric interaction dominant, but retain sufficient kinetic energy to flow. They can form short-range positional order in one or more directions with an anisotropic correlation length $\boldsymbol{\mu}$ that depends on their shape. The orientational correlation length $\boldsymbol{\xi}$ also remains high in some directions. In the smectic phase, for example, two-dimensional liquid layers are formed, that each have orientational alignment. At a higher temperature the correlation length μ becomes very small and the liquid isotropic. The material enters a state of positional disorder. In contrast, the orientational order correlation length ξ also tends toward isotropy, but maintains a relatively large magnitude. The result is the nematic phase in which the randomly positioned molecules are locally aligned. As the temperature is increased further, ξ becomes smaller and the orientational alignment is lost. The material turns into a macroscopically isotropic liquid, in spite of its microscopic anisotropy. Figure 2.3 gives a schematic representation of a possible phase transition at low temperature.

The word nematic is derived from the ancient Greek νῆμα (nêma) meaning *thread*. The name is motivated by the appearance of thread-like defects (disclination lines) that are commonly observed in these LCs. The cylindrically symmetric

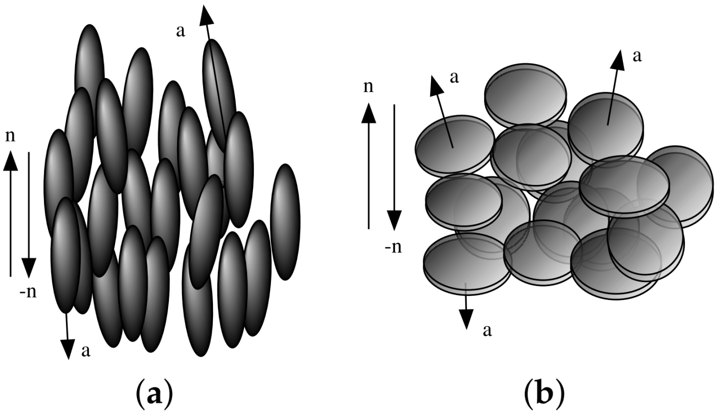

Figure 2.4: The two classes of nematic liquid crystals, (**a**) calamitic and (**b**) discotic with orientations **a** and director **n** (see section 2.3.1). Image credits: [25].

molecules that form NLCs can be classified as members of two categories. If they are elongated along the rotational symmetry axis they are called calamitic. If they are instead contracted along this axis, i.e. disk-like, they are called discotic (fig. 2.4). In the present work we focus on the calamitic variant. Usually, the inner part of the molecule is rigid and the outer part is flexible [25]. This structure drives the molecules toward parallel alignment, while retaining a fluidity that can be described in the hydrodynamic limit. The common axis of alignment is called the director and denoted by **n**.

2.3 Nematic Order Parameter

2.3.1 Director

At the most basic level NLCs can be modeled by assuming that their molecules are rigid rods. Each rod has an orientation, described by a unit vector **a**, identical to its axis of rotational symmetry. Clearly, if the rods have a cylindrical shape, **a** and $-\mathbf{a}$ refer to the same orientation. Even in materials within which individual molecules only have rotational symmetry, nematic properties may be recovered, if in any small volume there are just as many molecules with orientation **a** as with orientation $-\mathbf{a}$ [25]. The rods tend to align parallel with one another, due to steric and electrical interactions (see section 2.3.2). We introduce a dimensionless unit vector **n**, called the (Frank) director, that represents the average of the molecular orientation over a small volume element of material, taking into account the equivalence of **a** and $-\mathbf{a}$. Transitively, in NLCs **n** and $-\mathbf{n}$ are always equivalent descriptions of the system

$$\mathbf{n} \Leftrightarrow -\mathbf{n}. \tag{2.1}$$

In the absence of external fields the individual symmetries about the axes $\mathbf{a}_i$ result in a collective, statistical symmetry about **n**, i.e. the plane perpendicular to **n** is locally isotropic. Because in this case, geometrically, **n** gives the only relevant directions, the NLC is said to be uniaxial. Unconstrained NLCs will always equilibrate in a uniaxial phase, but boundary conditions and external fields may impose stresses that break the rotational symmetry about the director. The additional preferred axis $\hat{\mathbf{m}}^1$ is perpendicular to $\mathbf{n}$ and imposes a local orthonormal basis $(\mathbf{n}, \hat{\mathbf{m}}^1, \hat{\mathbf{m}}^2)$ on the system, with $\hat{\mathbf{m}}^2 = \pm\mathbf{n} \times \hat{\mathbf{m}}^1$. This describes the most general case. The coordinate basis $(\mathbf{n}, \hat{\mathbf{m}}^1, \hat{\mathbf{m}}^2)$ need not be right-handed, since $\hat{\mathbf{m}}^1$ and $\hat{\mathbf{m}}^2$, like $\mathbf{n}$, represent undirected axes ($\hat{\mathbf{m}}^1 \Leftrightarrow -\hat{\mathbf{m}}^1$ and $\hat{\mathbf{m}}^2 \Leftrightarrow -\hat{\mathbf{m}}^2$). Biaxial systems can be approximated as uniaxial. In most cases this approximation gives a good description, but, depending on the details of the system, the biaxiality may have to be taken into account.

2.3.2 Order Parameter

We can use the symmetry properties of nematics to derive a suitable order parameter. Using the director as a basis for the construction of a spherical coordinate system. Given the polar angle θ relative to $\mathbf{n}$ and the azimuthal angle ϕ the distribution function $f(\theta, \phi)\,\mathrm{d}\Omega$ yields the probability of finding a rod oriented in the small angle $\mathrm{d}\Omega = \sin\theta\,\mathrm{d}\theta\,\mathrm{d}\phi$. As described in section 2.3.1 the defining nematic property is the equivalence $\mathbf{a} \Leftrightarrow -\mathbf{a}$, and consequently $\mathbf{n} \Leftrightarrow -\mathbf{n}$. This implies for the distribution function

$$f(\theta, \phi) = f(\pi - \theta, \phi). \tag{2.2}$$

In uniaxial nematic materials the angular distribution function must also satisfy

$$f(\theta, \phi) = f(\theta). \tag{2.3}$$

The alignment of a molecule with the director is given by the inner product $\mathbf{a} \cdot \mathbf{n} = \cos\theta$. We can expand the orientational distribution function in terms of the alignment using the Legendre polynomials $P_n(x)$

$$f(\theta) = \sum_{n=0}^{\infty} f_n P_n(\cos\theta) = \sum_{n=0}^{\infty} (2n+1)\,\langle P_n(\cos\theta)\rangle\, P_n(\cos\theta), \tag{2.4}$$

where we rewrote the coefficients

$$f_n \equiv \frac{2n+1}{2} \int_{-1}^{1} f(\theta) P_n(\cos\theta)\,\mathrm{d}(\cos\theta) \tag{2.5}$$

as

$$f_n = (2n+1) \int f(\theta) P_n(\cos\theta)\,\mathrm{d}\Omega = (2n+1)\,\langle P_n(\cos\theta)\rangle\,. \tag{2.6}$$

Examining this multipole expansion, we find that all terms with odd n vanish, because of eq. (2.2). Since the monopole term

$$\langle P_0(\cos\theta)\rangle = \langle 1 \rangle = \int f(\theta)\,\mathrm{d}\Omega = 1 \tag{2.7}$$

is trivial and only gives the normalization, the lowest order non-zero term with descriptive power is the quadrupole term

$$S \equiv \langle P_2(\cos\theta)\rangle = \left\langle \frac{1}{2}\left(3\cos^2\theta - 1\right)\right\rangle = \int f(\theta)\frac{1}{2}\left(3\cos^2\theta - 1\right)\mathrm{d}\Omega\,, \tag{2.8}$$

which we call the order parameter S. It has the properties that we expect from an order parameter. In the isotropic case $\langle\cos^2\theta\rangle = 1/3$ and S vanishes. If the molecules are perfectly aligned, $\langle\cos^2\theta\rangle = 1$ and S reaches unity. However, perfect alignment is only possible at vanishing temperature. Therefore, S only approaches 1 asymptotically. Molecular LCs at room temperature typically have $S \approx 0.6$. This order parameter was first introduced by Tsvetkov in 1942 [26].

The coefficient S gives the scalar order, corresponding to the charge in the multipole expansion of electrodynamics. To get information about the geometrical configuration of the orientational distribution we need to look at the quadrupole moment tensor. It captures not only the charge, but also the principal axes, in this case, the director. Expanding $f(\theta)$ to the lowest descriptive order

$$\begin{aligned} f(\theta) &\approx \sum_{n=0}^{2}(2n+1)\langle P_n(\cos\theta)\rangle P_n(\cos\theta) = 1 + 5SP_2(\cos\theta) && (2.9)\\ &= 1 + \frac{15}{2}S\left[(\mathbf{a}\cdot\mathbf{n})^2 - \frac{1}{3}\right] = 1 + \frac{15}{2}Sa_ia_j\left(n_in_j - \frac{1}{3}\delta_{ij}\right) && (2.10)\\ &= 1 + 5Q^U_{ij}a_ia_j && (2.11)\end{aligned}$$

yields the traceless, symmetric tensor order parameter Q^U_{ij}. In the uniaxial case that we considered here it has the form

$$\boldsymbol{Q}^U \equiv \frac{3}{2}S\left(\mathbf{n}\otimes\mathbf{n} - \frac{1}{3}\boldsymbol{I}\right). \tag{2.12}$$

From a small calculation

$$\boldsymbol{Q}^U\mathbf{n} = \frac{3}{2}S\left(\mathbf{n} - \frac{1}{3}\mathbf{n}\right) = S\mathbf{n} \tag{2.13}$$

we see, that its largest eigenvalue is S and the corresponding eigenvector is $\mathbf{n}$. The other two eigenvectors are perpendicular to $\mathbf{n}$ and have eigenvalues $-S/2$.

The tensor order parameter can also be constructed without a priori knowledge of the director $\mathbf{n}$. Because of the $\mathbf{a} \Leftrightarrow -\mathbf{a}$ symmetry, any nematic order parameter has to be even in the particle orientations $\mathbf{a}$. Considering the average $\langle\cdot\rangle$ over a volume, the lowest order tensor parameter that is even in $\mathbf{a}$ is the dyadic $\langle a_ia_j\rangle$. It contains exactly the same information as $\mathbf{n}$, except for the sign of the direction. The order parameter should measure the deviation from isotropy. Therefore, we must remove the isotropic part (i.e. the trace), again, arriving at the tensor order parameter

$$\boldsymbol{Q} \equiv \frac{3}{2}\left\langle \mathbf{a}\otimes\mathbf{a} - \frac{1}{3}\boldsymbol{I}\right\rangle. \tag{2.14}$$

The normalization constant 3/2 is arbitrary and ensures that the definition matches eq. (2.12) for uniaxial nematics. This approach of constructing the order parameter generalizes to any macroscopic response (see appendix A.1).

It is easily seen that the definition in eq. (2.14) reduces to eq. (2.12) in the uniaxial case. Choosing a coordinate system with the z-axis parallel to the director, $\hat{\mathbf{e}}_z \parallel \mathbf{n}$, we have

$$\begin{aligned}\boldsymbol{Q}\hat{\mathbf{e}}_z &= \frac{3}{2}\left\langle \mathbf{a}\otimes\mathbf{a} - \frac{1}{3}\boldsymbol{I}\right\rangle \hat{\mathbf{e}}_z = \frac{3}{2}\left\langle \cos(\theta)\mathbf{a} - \frac{1}{3}\hat{\mathbf{e}}_z\right\rangle = \frac{3}{2}\left\langle \cos^2(\theta)\hat{\mathbf{e}}_z - \frac{1}{3}\hat{\mathbf{e}}_z\right\rangle \\ &\quad + \frac{3}{2}\left\langle \cos(\phi)\sin(\theta)\cos(\theta)\hat{\mathbf{e}}_x + \sin(\phi)\sin(\theta)\cos(\theta)\hat{\mathbf{e}}_y\right\rangle = S\hat{\mathbf{e}}_z.\end{aligned}$$

If the NLC is not uniaxial, i.e. biaxial, the order parameter's symmetry and tracelessness leave five degrees of freedom. Three are taken up by the scalar order parameter S and the director $\mathbf{n}$. As discussed in section 2.3.1, biaxial systems have one additional directional degree of freedom, the direction of $\hat{\mathbf{m}}^1 \perp \mathbf{n}$. The final free parameter must describe the deviation from uniaxiality. This deviation is quantified by the difference between the smaller eigenvalues of $\boldsymbol{Q}$, which we call the biaxiality

$$P = \left\langle \sin^2\theta\cos 2\phi \right\rangle. \tag{2.15}$$

The biaxial order parameter has to be expressed in terms of $\mathbf{n}\otimes\mathbf{n}$, $\hat{\mathbf{m}}^1\otimes\hat{\mathbf{m}}^1$, and $\hat{\mathbf{m}}^2\otimes\hat{\mathbf{m}}^2$ (see section 2.3.1), be traceless, reduce to $\boldsymbol{Q}$ in the uniaxial case and have P as the only additional degree of freedom. Barring arbitrary scaling of P, the only such order parameter is[2]

$$\boldsymbol{Q} \equiv \frac{3}{2}S\left(\mathbf{n}\otimes\mathbf{n} - \frac{1}{3}\boldsymbol{I}\right) + \frac{1}{2}P\left(\hat{\mathbf{m}}^1\otimes\hat{\mathbf{m}}^1 - \hat{\mathbf{m}}^2\otimes\hat{\mathbf{m}}^2\right). \tag{2.16}$$

With our choice of P the eigenvalue-eigenvector pairs are $(S, \mathbf{n})$, $(-[S+P]/2, \hat{\mathbf{m}}^1)$ and $(-[S-P]/2, \hat{\mathbf{m}}^2)$ with $P \in [-3/2, 3/2]$. Since $\boldsymbol{Q}$ is invariant under the transformation $(P, \hat{\mathbf{m}}^1, \hat{\mathbf{m}}^2) \mapsto (-P, \hat{\mathbf{m}}^2, \hat{\mathbf{m}}^1)$, P can always be chosen as positive. Note, that not only P, but also S and $\boldsymbol{Q}$ may be scaled arbitrarily, since any constants can be absorbed by the coefficient in eq. (2.4). In uniaxial systems the scalar order parameter is easily obtained, either from the diagonalization of $\boldsymbol{Q}$, or from the second trace invariant

$$S^2 = \frac{2}{3}\operatorname{Tr}\left[\left(\boldsymbol{Q}^U\right)^2\right] = \frac{2}{3}Q^U_{ij}Q^U_{ij}, \tag{2.17}$$

directly. This generalizes to biaxial systems as

$$S^2 + \frac{1}{3}P^2 = \frac{2}{3}\operatorname{Tr}\boldsymbol{Q}^2 = \frac{2}{3}Q_{ij}Q_{ij}, \tag{2.18}$$

---

[2] Equivalently, one can take a purely mathematical approach. The order parameter $\boldsymbol{Q}$ is symmetric. Every real, symmetric matrix has an orthonormal eigenbasis. Calling the largest eigenvalue S, the sum of the smaller ones is fixed at $-S$, because $\boldsymbol{Q}$ is traceless. This leaves their difference, which we define as P, as the last free parameter. Associating the eigenvalues with their eigenvectors and invoking the definition of P, one arrives at this representation.

so that the third trace invariant

$$\operatorname{Tr}\boldsymbol{Q}^3 = Q_{ij}Q_{jk}Q_{ki} = \frac{3}{4}S\left(S^2 - P^2\right) \tag{2.19}$$

is needed to calculate S.

2.4 Elasticity of Nematic Liquid Crystals

In an ideal, unconstrained LC at constant temperature the order parameter is constant in space and time. Under the influence of external fields and boundary conditions, however, the director $\mathbf{n}$ undergoes local deformations. Assuming the deformations happen on a large enough scale

$$l\, n_{j,i} \ll 1, \tag{2.20}$$

with molecular scale typically $l \approx 20\,\text{Å}$, the distortions can be modeled in the continuum limit. In this case the position-dependence of the order parameter Q_{ij} can be described entirely by the spatial derivatives of the director $n_{j,i}$. Making use of the symmetries in uniaxial nematics we can find the general lowest-order approximation of the distortion free energy density F_d. With knowledge of this free energy density the task of finding the director configurations reduces to a minimization problem of F_d for given boundary conditions.

Since nematic systems are invariant under the transformation $\mathbf{n} \mapsto -\mathbf{n}$, F_d must be even in $\mathbf{n}$. We also require that our description be invariant under rotations of the coordinate system. This rules out terms linear in $n_{j,i}$, except for $n_{i,i}$ and $\epsilon_{ijk}n_i n_{k,j}$ [27]. Neither conforms to eq. (2.1). In fact, terms of the form $y_{i,i}$ for any vector field $\mathbf{y}(\mathbf{r})$ may be omitted. By Stokes' law they only describe contributions to the surface energy and not to the volume energy. At the lowest order we are left with terms quadratic in $n_{j,i}$. We may separate this tensor into a symmetric part

$$u_{ij} = \frac{1}{2}\left(n_{j,i} + n_{i,j}\right) \tag{2.21}$$

and an antisymmetric part

$$m_{ij} = \frac{1}{2}\left(n_{j,i} - n_{i,j}\right). \tag{2.22}$$

They are related to the divergence of the director by

$$u_{ii} = \boldsymbol{\nabla} \cdot \mathbf{n} \tag{2.23}$$

and to the curl by

$$m_{ij} = -\frac{1}{2}\epsilon_{ijk}(\boldsymbol{\nabla} \times \mathbf{n})_k. \tag{2.24}$$

The symmetric part u_{ij} is constrained by the normalization of $\mathbf{n}$. In the coordinate system introduced in section 2.3.2 the z-axis is parallel to the director. A simple consideration of

$$0 = \boldsymbol{\nabla} \mathbf{n}^2 = \boldsymbol{\nabla} \left(n_x^2 + n_y^2 + n_z^2 \right) = 2 n_z \boldsymbol{\nabla} n_z . \tag{2.25}$$

shows that the gradient of n_z vanishes in all components. This implies for the components of u_{ij}

$$\begin{cases} u_{zx} = \frac{1}{2} (\boldsymbol{\nabla} \times \mathbf{n})_y \,, \\ u_{zy} = -\frac{1}{2} (\boldsymbol{\nabla} \times \mathbf{n})_x \,, \\ u_{zz} = 0. \end{cases} \tag{2.26}$$

If we want to consider the contributions of u_{ij} and m_{ij} to F_{d}, separately, we need to take into account cross terms $F_\times$, since the distortion free energy is quadratic in $n_{j,i}$. We can in general write

$$F_{\mathrm{d}} \equiv F_u + F_m + F_\times , \tag{2.27}$$

where F_u is the free energy term depending on u_{ij}, and F_m the one depending on m_{ij}. Since we are studying uniaxial nematics, finding F_u is equivalent to finding the free energy for a system of continuous rotational symmetry C_∞ around $\hat{\mathbf{e}}_z$. In a hexagonal crystal (class C_6) with symmetry axis $\hat{\mathbf{e}}_z$ the free energy is [28]

$$F_u = \chi_1 u_{zz}^2 + \chi_2 \left(u_{xx} + u_{yy} \right)^2 + \chi_3 u_{ij} u_{ji} + \chi_4 u_{zz} \left(u_{xx} + u_{yy} \right) + \chi_5 \left(u_{xx}^2 + u_{yy}^2 \right) \tag{2.28}$$

where the χ_i are arbitrary material constants. Here, a deformation in the xy-plane, i.e. a deformation with vanishing z-components in u_{ij} is determined by only two elastic constants. Since this describes the elasticity of an isotropic body, the elastic properties of the hexagonal system are isotropic in the xy-plane. Therefore, eq. (2.28) also describes systems with C_∞-symmetry. The properties in eq. (2.26) imply that two of the terms vanish

$$F_u = \chi_2 (\boldsymbol{\nabla} \cdot \mathbf{n})^2 + \chi_3 u_{ij} u_{ji} + \chi_5 \frac{1}{4} (\mathbf{n} \times \boldsymbol{\nabla} \times \mathbf{n})^2 . \tag{2.29}$$

Using the identity

$$u_{ij} u_{ji} = (\boldsymbol{\nabla} \cdot \mathbf{n})^2 + \frac{1}{2} (\boldsymbol{\nabla} \times \mathbf{n})^2 + \partial_i \left(n_j \partial_j n_i \right) - \partial_j \left(n_i \partial_i n_j \right) \tag{2.30}$$

for the double dot product, and dropping its last two terms because they represent surface contributions, we are left with

$$F_u = \chi_2 (\boldsymbol{\nabla} \cdot \mathbf{n})^2 + \chi_3 \left[(\boldsymbol{\nabla} \cdot \mathbf{n})^2 + \frac{1}{2} (\boldsymbol{\nabla} \times \mathbf{n})^2 \right] + \chi_5 \frac{1}{4} (\mathbf{n} \times \boldsymbol{\nabla} \times \mathbf{n})^2 .$$

Separating the curl into a part parallel to and a part perpendicular to $\mathbf{n}$ we can re-parametrize this to

$$F_u = \chi_1' (\boldsymbol{\nabla} \cdot \mathbf{n})^2 + \chi_2' (\mathbf{n} \cdot \boldsymbol{\nabla} \times \mathbf{n})^2 + \chi_3' (\mathbf{n} \times \boldsymbol{\nabla} \times \mathbf{n})^2 , \tag{2.31}$$

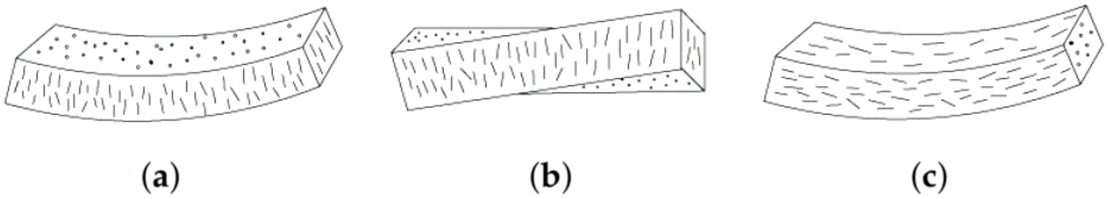

Figure 2.5: The three types of deformations that occur in nematic liquid crystals: (**a**) splay, (**b**) twist, and (**c**) bend. Each can be attained independently. The black dashes represent the local director. Image credits: [29].

where we used the fact that **n** is a unit vector. The contribution F_m can be given purely in quadratic terms of the curl $\boldsymbol{\nabla} \times \mathbf{n}$, as eq. (2.24) states. Isotropy in the xy-plane demands the form

$$\begin{aligned} F_m &= \kappa_1 (\boldsymbol{\nabla} \times \mathbf{n})_z^2 + \kappa_2 \left[(\boldsymbol{\nabla} \times \mathbf{n})_x^2 + (\boldsymbol{\nabla} \times \mathbf{n})_y^2 \right] \\ &= \kappa_1' (\mathbf{n} \cdot \boldsymbol{\nabla} \times \mathbf{n})^2 + \kappa_2' (\mathbf{n} \times \boldsymbol{\nabla} \times \mathbf{n})^2, \end{aligned} \tag{2.32}$$

where, just as in eq. (2.31), we separated the curl into a part parallel to and a part perpendicular to **n**.

Considering the contributions of m_{ij} to the cross term $F_\times$, the only term linear in $(\boldsymbol{\nabla} \times \mathbf{n})_z$ allowed by the continuous rotational symmetry is

$$(\boldsymbol{\nabla} \times \mathbf{n})_z (u_{xx} + u_{yy}) = (\mathbf{n} \cdot \boldsymbol{\nabla} \times \mathbf{n}) \boldsymbol{\nabla} \cdot \mathbf{n}, \tag{2.33}$$

which must vanish because it is odd in **n**. The only terms linear in the components within the isotropic plane $(\boldsymbol{\nabla} \times \mathbf{n})_x$ and $(\boldsymbol{\nabla} \times \mathbf{n})_y$ are

$$(\boldsymbol{\nabla} \times \mathbf{n})_x u_{xz} + (\boldsymbol{\nabla} \times \mathbf{n})_y u_{yz} = 0, \tag{2.34}$$

$$(\boldsymbol{\nabla} \times \mathbf{n})_y u_{zx} - (\boldsymbol{\nabla} \times \mathbf{n})_x u_{zy} = \frac{1}{2} (\mathbf{n} \times \boldsymbol{\nabla} \times \mathbf{n})^2. \tag{2.35}$$

Because of the constraints on the symmetric tensor u_{ij} in eq. (2.26), the first term vanishes. Therefore, the most general form of the cross term is

$$F_\times = \nu_1 (\mathbf{n} \times \boldsymbol{\nabla} \times \mathbf{n})^2. \tag{2.36}$$

Combining the contributions in eqs. (2.31), (2.32) and (2.36) yields the complete formulation of the distortion energy

$$F_\mathrm{d} = \frac{K_1}{2} (\boldsymbol{\nabla} \cdot \mathbf{n})^2 + \frac{K_2}{2} (\mathbf{n} \cdot \boldsymbol{\nabla} \times \mathbf{n})^2 + \frac{K_3}{2} (\mathbf{n} \times \boldsymbol{\nabla} \times \mathbf{n})^2. \tag{2.37}$$

It was first proposed by Frank [30]. The three terms can be physically interpreted as the splay (K_1), the twist (K_2), and the bend (K_3) of the medium. They are visualized in figure 2.5. Since each of the three distortions can be generated independently, they must all have positive coefficients in the free energy. The elastic constants K_i are strongly temperature dependent. They scale roughly as the square of the order parameter S [27].

We may also express the free energy density in terms of $\boldsymbol{Q}$. Analogously to eq. (2.37) it should only contain terms that are quadratic products of the gradient $\boldsymbol{\nabla Q}$. Expanding the free energy density in $\boldsymbol{Q}$ as the sum of all possible variations to the same order as before, we get

$$F_{\mathrm{d}}^{Q} = \frac{\kappa_{ijklmn}}{2} Q_{ij,k} Q_{lm,n} + \mathcal{O}\Big((Q_{ij} Q_{kl,m})^2 \Big) \tag{2.38}$$

$$= \frac{\kappa_1}{2} Q_{ii,k} Q_{jj,k} + \frac{\kappa_2}{2} Q_{ij,k} Q_{ij,k} + \frac{\kappa_3}{2} Q_{ik,i} Q_{jk,j} + \frac{\kappa_4}{2} Q_{ik,j} Q_{jk,i} + \mathcal{O}\Big((Q_{ij} Q_{kl,m})^2 \Big). \tag{2.39}$$

Because of the (ij)-, the (lm)- and the $((ijk)(lmn))$-symmetries of κ_{ijklmn}, the terms can be grouped to have four effective constants. Through integration by parts over the bulk, it can be shown that the κ_4-term can be absorbed into the other terms [31]. Almost all of the next-higher order terms can also be absorbed into the present ones; only one of them can not [32]

$$\frac{\kappa_5}{2} Q_{ij} Q_{kl,i} Q_{kl,j}.$$

Including it, F_{d}^{Q} can be mapped to F_{d}, exactly. Assuming uniaxiality [see eq. (2.12)] the terms transform to

$$\frac{\kappa_1}{2} Q_{ii,k} Q_{jj,k} = 0, \tag{2.40}$$

$$\frac{\kappa_2}{2} Q_{ij,k} Q_{ij,k} = \kappa_2 S^2 n_{i,k} n_{i,k}, \tag{2.41}$$

$$\frac{\kappa_3}{2} Q_{ik,i} Q_{jk,j} = \kappa_3 S^2 \big(n_i n_j n_{k,i} n_{k,j} + n_{i,i} n_{j,j} \big), \tag{2.42}$$

$$\frac{\kappa_5}{2} Q_{ij} Q_{kl,i} Q_{kl,j} = \kappa_5 S^3 \left(n_i n_j n_{l,i} n_{l,j} - \frac{1}{3} n_{i,j} n_{i,j} \right). \tag{2.43}$$

The final form of F_{d}^{Q} is therefore

$$F_{\mathrm{d}}^{Q} = \frac{L_1}{2} Q_{ij,k} Q_{ij,k} + \frac{L_2}{2} Q_{ik,i} Q_{jk,j} + \frac{L_3}{2} Q_{ij} Q_{kl,i} Q_{kl,j}. \tag{2.44}$$

Comparing it to eq. (2.37) in index form

$$F_{\mathrm{d}} = \frac{K_1}{2} n_{i,i} n_{j,j} + \frac{K_2}{2} \big(n_{i,j} n_{i,j} - n_{i,i} n_{j,j} - n_i n_j n_{k,i} n_{k,j} \big) + \frac{K_3}{2} n_i n_j n_{k,i} n_{k,j} \tag{2.45}$$

using eqs. (2.40)-(2.43) we see that $F_{\mathrm{d}}^{Q} = F_{\mathrm{d}}(\boldsymbol{Q})$ if [33]

$$L_1 = \frac{3K_2 - K_1 + K_3}{6S^2}, \tag{2.46}$$

$$L_2 = \frac{K_1 - K_2}{S^2}, \tag{2.47}$$

$$L_3 = \frac{K_3 - K_1}{2S^3}. \tag{2.48}$$

The elastic constants depend on density and temperature of the medium, increasing with density and decreasing with temperature. The splay constant K_1 decreases exponentially with temperature. The decrease of K_2 and K_3 is approximately linear [34]. For lyotropic chromonic LCs at room temperature the splay and bending constants have similar magnitudes of about 20 pN [34]. The twisting constant is smaller by a factor of 10. Low molecular weight thermotropic LCs have negligible variation in the elastic constants. This justifies the so-called one-constant approximation $K \equiv K_1 = K_2 = K_3$, which greatly simplifies theoretical considerations and practical applications, while maintaining qualitative behavior. In the one-constant approximation the distortion free energy simplifies to

$$F_{\mathrm{d}}^{K} = \frac{1}{2}K\left|n_{j,i}\right|^2 \tag{2.49}$$

$$= \frac{1}{2}L\left|Q_{ij,k}\right|^2 \tag{2.50}$$

with the relation

$$L = K/2S^2 \tag{2.51}$$

between the elastic constants. Already, given $K_1 = K_3$, L_3 vanishes and no higher order terms are needed in $F^{\mathrm{d}}(\boldsymbol{Q})$.

The potential in eq. (2.49) is pairwise additive. This property was used in combination with the Maier-Saupe mean-field approximation (see section 2.6.1) by Lebwohl and Lasher [35, 36]. They introduced a lattice model of NLCs that considered an interaction potential of the form

$$U = -\epsilon \sum_{\langle i,j \rangle} \left(\mathbf{a}_i \cdot \mathbf{a}_j\right)^2 \tag{2.52}$$

for the orientations of neighboring molecules $\langle i, j \rangle$ with interaction constant ϵ. This description is equivalent to the one derived here in the one-constant approximation [37]. The Lebwohl-Lasher model has since also been used in continuum theory of NLCs [27].

In the presence of boundaries the total deformation energy differs by extra surface terms from eq. (2.37). However, in most cases these extra terms dominate only within their short range of influence [27]. The result is a strong anchoring at the confining surface. In these cases the director configuration can be found by minimizing F_{d} according to eq. (2.37) with $\mathbf{n}(\mathbf{r})$ fixed at the boundaries or anchored to the direction $\mathbf{n}_0(\mathbf{r})$ by an extra surface term [6]

$$F_{\mathrm{d}}^{A} = \frac{1}{2}W_A(\mathbf{n} - \mathbf{n}_0)^2 \tag{2.53}$$

that is only present at the boundaries and has anchoring strength W_A. Analogously, $\boldsymbol{Q}$ may be fixed at the boundaries or anchored by an additional surface term [6]

$$F_{\mathrm{d}}^{A} = \frac{1}{2}W_A(\boldsymbol{Q} - \boldsymbol{Q}_0)^2 \tag{2.54}$$

with

$$\boldsymbol{Q}_0(\mathbf{r}) \equiv S_0(\mathbf{r})\left(\mathbf{n}_0(\mathbf{r}) \otimes \mathbf{n}_0(\mathbf{r}) - \frac{1}{3}\boldsymbol{I}\right). \tag{2.55}$$

This, unavoidably, anchors not only the director to $\mathbf{n}_0$, but also the scalar order parameter to S_0 at that location. Depending on the chemical properties of both the nematic and the confinement material the surface alignment may take any kind of orientation. Two important cases are the homeotropic (orthogonal to the boundary) and homogeneous (parallel to the boundary) anchoring.

2.5 Topological Defects

(a) with defect **(b)** without defect

Figure 2.6: A defect in 2 dimensions with winding number 0 can be remediated by a local transformation. Such transformations are brought about, automatically, by the elastic forces of a nematic. Image credits [38].

The director characterizes the nematic properties of a system locally. For a nematic model to be valid we require that deformations happen on a large scale relative to the molecule size (see section 2.4). The director field should therefore be continuous almost everywhere. We call the connected subsets of $\mathbb{R}^d$ where $\mathbf{n}$ is not continuous defects. Simple defects, such as the one shown in figure 2.6, can be rectified by a change of $\mathbf{n}$ within an arbitrarily small neighborhood of the defect. Since they represent a large distortion, such defects will normally be prevented, as the free energy is minimized (see section 2.4).

Unlike the one shown in figure 2.6, defects may have non-local structural impact on a system. Consider a point $\mathbf{y} \in \mathbb{R}^2$ with undetermined director that has a neighborhood within which the director is continuous. If we look at the angle θ between the director and a global coordinate axis and integrate in a closed loop C around $\mathbf{y}$

$$\oint_C \frac{\mathrm{d}\theta}{\mathrm{d}s}\mathrm{d}s = 2\pi n, \tag{2.56}$$

the result has to be a multiple of π, $n \in \mathbb{N}/2$, due to continuity of $\mathbf{n}$ and $\mathbf{n} \equiv -\mathbf{n}$ equivalence. If $n \neq 0$, there cannot exist a field $\mathbf{n}(\mathbf{x})$ that is continuous in $\mathbf{y}$

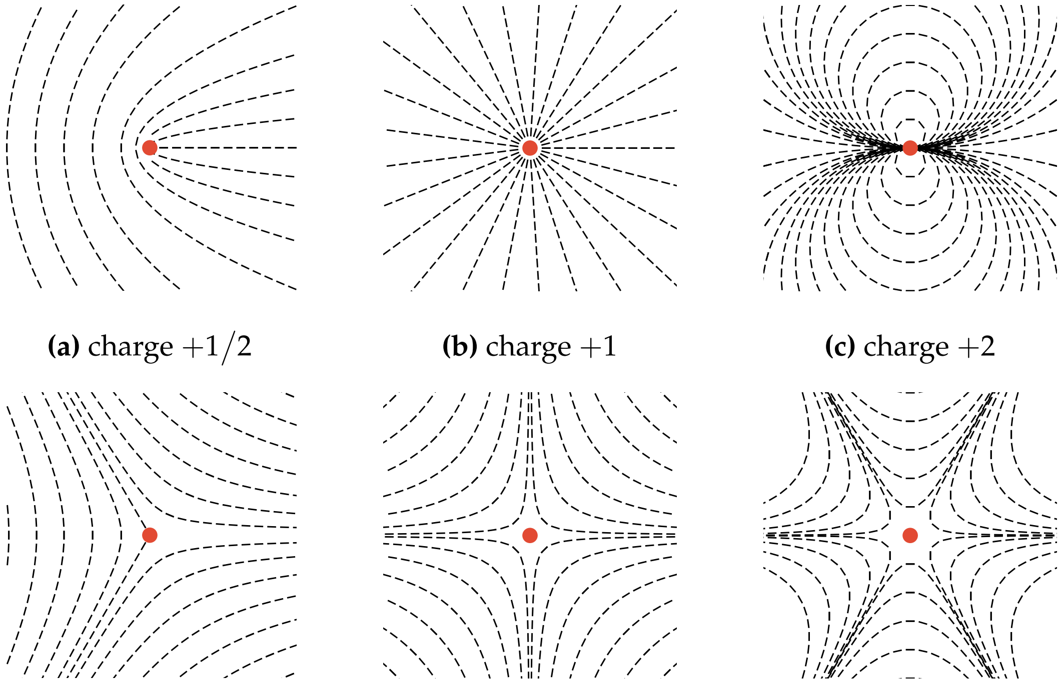

Figure 2.7: Commonly encountered topological defects and their charges. The singularities are marked in red. The director field is indicated by the black dashes.

(imagine choosing C arbitrarily close to $\mathbf{y}$). The factor n is called the winding number. The topology of a region is completely determined by the sum of the winding numbers of all defects inside. This is analogous to Gauss's law

$$\int_{\partial V} \mathbf{E} \cdot \mathrm{d}\mathbf{A} = \frac{1}{\epsilon_0} \int_V \rho \, \mathrm{d}V \tag{2.57}$$

where the electrical field $\mathbf{E}$ on a boundary depends on the sum of electrical charges $\int \rho \, \mathrm{d}V$ inside. Therefore, n is also referred to as the topological charge of a defect. Examples of defects with low $|n|$ are displayed in figure 2.7. Note, that non-integer values are only possible in nematic systems. Like their electrical counterparts, topological charges of equal sign are repelled and charges of opposite sign are attracted by one another.

Typically, global rotations of the director field are identical to some transformation of the coordinate system. An exception is the $+1$-charge defect. In equilibrium there exist three different kinds of charge +1 defects. Figure 2.7 **(b)** shows an aster. The remaining types, vortex and spiral are shown in figure 2.8.

Considering rotationally symmetric fields, it is convenient to introduce polar coordinates r and θ. In two dimensions, the orientation of the field may be parametrized by the angle ψ between the radial vector $\hat{\mathbf{e}}_r$ and the director $\mathbf{n}$. With this notation the aster in figure 2.7 **(b)** corresponds to a constant $\psi = 0$. The vortex and spiral in figure 2.8 are described by $\psi = \pi/2$, and $\psi = \pi/4$, respectively.

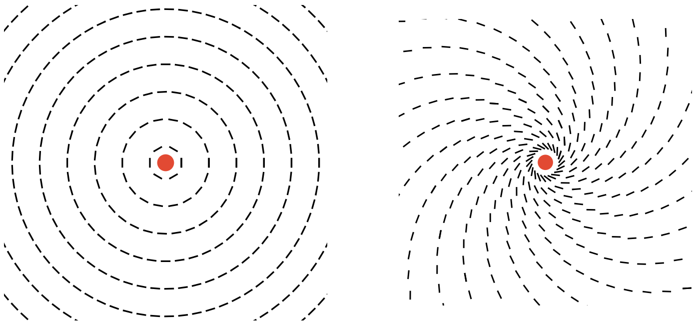

(a) Vortex **(b)** Spiral

Figure 2.8: Variations of the topological defect with charge +1.

For rotationally symmetric director fields $\psi = \psi(r)$ the free energy density in eq. (2.37) yields

$$F = 2\pi r \left[\frac{K_1}{2} \left(\frac{1}{r} \frac{\mathrm{d}}{\mathrm{d}r} r \cos\psi \right)^2 + \frac{K_3}{2} \left(\frac{1}{r} \frac{\mathrm{d}}{\mathrm{d}r} r \sin\psi \right)^2 \right], \tag{2.58}$$

assuming no twist (guaranteed in two dimensions), and neglecting the spontaneous splay which leads to a boundary term. Kruse *et al.* did a linear stability analysis for constant ψ [39]. In equilibrium and two dimensions asters are stable for $\delta K \equiv K_3 - K_1 > 0$. In the opposite case $\delta K < 0$, vortices are stable. If K_1 and K_3 are equal (given in the one-constant approximation), all constant solutions $\psi(r) = \psi_0$ are stable. This includes asters, vortices, and all spirals.

Kruse *et al.* also studied the stability of defects in driven systems. They found that outside of equilibrium the same configurations are stable, depending on δK, as in equilibrium, if the active stress is extensile $\overline{\zeta \Delta \mu} > 0$ ($\overline{\zeta \Delta \mu}$ is an activity parameter). This behavior also holds true for small contractile stresses ($\overline{\zeta \Delta \mu} < 0$). At a critical value $\overline{\zeta \Delta \mu}_C$, that is linear in K_3, spirals become more stable. They become the energetically optimal solution for growing intervals around $\delta K = 0$. The phase diagram is given in figure 2.9.

The arguments by Kruse *et al.* only hold in 2 dimensions. In 3 dimensions, the director at the core of defects with winding number ±1 escapes into the third dimension in order to lower the defect's energy [40]. Still, the general tenets of this section extend to 3 dimensions, where systems often form disclination lines. When looked at in two dimensions these singular lines have exactly the same appearance as the ordinary defects discussed here. From a topological point of view they are periodic in the third dimension. Of course, this means that they can exhibit all kinds of deformations along the third axis.

When a NLC experiences a sudden change in temperature or pressure and goes from the isotropic to a nematic state, the elastic forces need some time to take effect. Small regions with independent order parameters fuse together and form defects to make the director field locally smooth. This process is called the Kibble mechanism [41].

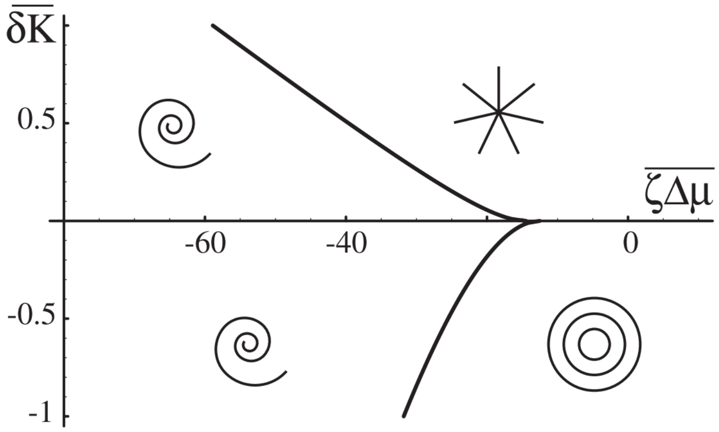

Figure 2.9: Stability diagram of spirals (left), asters (top right), and vortices (bottom right) in terms of elastic constant $\overline{\delta K} \equiv (K_3 - K_1)/K_1$ and activity parameter $\overline{\zeta\Delta\mu}$. For extensile, and for small contractile active stresses spirals are only stable at $\overline{\delta K} = 0$; asters are stable for $\overline{\delta K} > 0$; vortices are stable for $\overline{\delta K} < 0$. With increasing contractile stress the stable region for spirals grows. Image credits: [39].

As the system evolves towards equilibrium, most of the newly formed defects annihilate. In a simplified picture with only a $+1/2$ and a $-1/2$ defect, the potential energy is [42]

$$E_{+,-} = d' \log \frac{s}{s_c}, \tag{2.59}$$

where d' is a proportionality constant, $s \equiv |\mathbf{r}_+ - \mathbf{r}_-|$ is the separation of the defects, and s_c is the radius of the defect's core. The force balance

$$0 = F_{\text{friction}} - \frac{\mathrm{d}}{\mathrm{d}s} E_{+,-} = \mu_d \dot{s} - \frac{d'}{s}, \tag{2.60}$$

with friction coefficient μ_d, implies the differential equation [43]

$$\frac{\mathrm{d}s}{\mathrm{d}t} \propto \frac{1}{s}. \tag{2.61}$$

The solutions

$$s = d_0 \sqrt{t_0 - t}, \tag{2.62}$$

with proportionality constant d_0, are commonly used in nematics. There exist, however, more precise models of defect annihilation. In experiments, the friction coefficient μ_d is not a constant. Assuming a logarithmic increase in s [42,44]

$$\mu_d = \mu_0 \log \frac{s}{s_c}, \tag{2.63}$$

eq. (2.60) implies

$$\frac{\mathrm{d}s}{\mathrm{d}t} \propto \left[s \ln\left(\frac{s}{s_c}\right)\right]^{-1}. \tag{2.64}$$

This ordinary differential equation has solutions

$$s(t) = \frac{d_1\sqrt{t_0 - t}}{W\big(d_1^2(t_0 - t)/s_c^2\mathrm{e}\big)} \tag{2.65}$$

with the product log function $W(x)$, Euler's number e, and proportionality constant d_1. Since eq. (2.65) is much harder to deal with than eq. (2.62), and gives only marginally more accurate results, the simpler solution is often preferred.

The study of topological defects has many practical applications. They play a large role in the behavior of NLCs inside complex environments, as they reflect the topological properties of the boundaries. For example, defects have been used to facilitate the self-assembly of colloidal particles. Muševič *et al.* [45] showed, how these particles, when embedded in a few-micrometer-thick layer of a NLC, arrange to 2-dimensional crystal structures bound by topological defects. For more applications see the end of section 2.8.

2.6 Isotropic-Nematic Phase Transition

LCs can exist in many different phases, that differ in thermal energy, mass density, and, most importantly, in the type of order (see section 2.2). We focus on the nematic phase, which forms as an isotropic LC is cooled down. Phase transitions such as these are characterized by the local behavior of thermodynamic potentials around the transition point. Depending on whether the temperature T and pressure p, or the temperature T and volume V are being kept constant, the significant thermodynamic potential will be the Gibbs free energy or the Helmholtz free energy. The phase transition is called first order, if the first derivative of this free energy is discontinuous at the transition point. This implies coinciding discontinuities of the entropy and of the order parameter. A second-order phase transition has an exactly once differentiable thermodynamic potential, meaning that the heat capacity (the second derivative of the free energy) diverges. The isotropic-nematic phase transition is of first order, but the involved discontinuity in the first derivative is small. The transition is therefore called weakly first-order.

There exist vastly differing theories that model this phase transition. We will introduce two of them. The Maier-Saupe model focuses on anisotropic van-der-Waals-forces of attraction in a mean field approximation. Landau-de Gennes theory takes a phenomenological approach, expanding the free energy near the transition point in powers of the order parameter, and leveraging symmetries.

The specific choice of thermodynamic potential under examination is insignificant. In practice, typically, the temperature and pressure are kept constant, leading to a minimization of the Gibbs free energy. Computer simulations are much easier at constant temperature and volume, describing minima of the Helmholtz free energy. In the case of the isotropic-nematic transition the density or volume change around the transition point is small (0.3% at atmospheric pressure), making the derivatives of the Gibbs and the Helmholtz free energy practically identical [25].

We will therefore use an abstract free energy that may be substituted for one of the aforementioned at will.

2.6.1 Maier-Saupe Mean Field Theory

The mean field theory proposed by Maier and Saupe [46] models the transition between the isotropic and the nematic phase. It has been very successful in spite of completely ignoring short-range interactions [47]. The approach is analogous to the molecular field approximation Weiss employed in 1906 for ferromagnets [48]. The theory yields the angular distribution function at different temperatures. This allows for the calculation of the order parameter $S(T)$ as a function of temperature. We start from the free energy, which may be expressed as

$$F(p,T) = F_{\mathrm{iso}}(p,T) - F_{TS} + F_1(p,T,S) \tag{2.66}$$

with the entropic term

$$F_{TS} = -k_{\mathrm{B}}T \int_{S_2} f(\theta) \log[4\pi f(\theta)] \, \mathrm{d}\Omega \tag{2.67}$$

where F_{iso} is the free energy in the isotropic phase and F_1 describes the effects of intermolecular interactions. Since we are dealing with uniaxial nematics, f only depends on the polar angle θ (see eq. (2.3)). Maier and Saupe postulated that the orientational energy per molecule be

$$u_i \propto -\frac{1}{2}\left(3\cos^2\theta_i - 1\right) \left\langle \frac{1}{2}\left(3\cos^2\theta_i - 1\right) \right\rangle = -\frac{1}{2}\left(3\cos^2\theta_i - 1\right) S, \tag{2.68}$$

because it must have an orientational dependence varying as $-P_2(\cos\theta)$ (i.e. exhibiting a minimum for $\theta = 0$, and a maximum for $\theta = \frac{\pi}{2}$) and because the strength of the molecular interaction should be proportional to the global amount of nematic order, that is $S = \langle P_2(\cos\theta) \rangle$. We may use this in expressing F_1 as

$$F_1 = -\frac{1}{2} U(p,T) S^2 \tag{2.69}$$

where U has to be a positive coefficient which depends on the material properties. Minimizing F with respect to variations in the angular distribution f we obtain

$$\delta F = \lambda \int \delta f(\theta) \, \mathrm{d}\Omega \tag{2.70}$$

which is further constrained by the normalization of f. The constituents of the variation δF are

$$\delta F_1 = -US\,\delta S = -US \int \frac{1}{2}\left(3\cos^2\theta - 1\right) \delta f \, \mathrm{d}\Omega \tag{2.71}$$

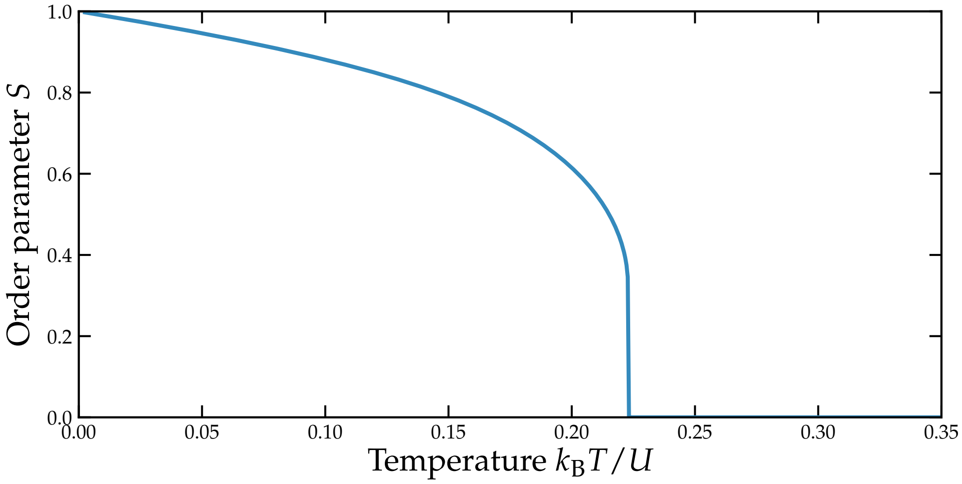

Figure 2.10: The order parameter S as a function of temperature T in the Maier-Saupe mean field theory.

and the entropic term

$$\delta F_{TS} = -k_\mathrm{B}T \int \frac{\partial[f\log(4\pi f)]}{\partial f}\,\delta f\,\mathrm{d}\Omega = -k_\mathrm{B}T \int \left[\log(4\pi f) + \frac{1}{4\pi}\right]\delta f\,\mathrm{d}\Omega\,. \tag{2.72}$$

The isotropic term F_iso is of course independent of f. Equation (2.70) yields

$$\log[4\pi f(\theta)] = \frac{\lambda}{k_\mathrm{B}T} - \frac{1}{4\pi} + \frac{1}{2}\frac{US}{k_\mathrm{B}T}\left(3\cos^2\theta - 1\right). \tag{2.73}$$

The normalized solution is

$$f(\theta) = \frac{1}{4\pi Z}\exp\left(\frac{3}{2}\frac{US}{k_\mathrm{B}T}\cos^2\theta\right) \tag{2.74}$$

with

$$Z \equiv \int_0^1 \exp\left(mx^2\right)\mathrm{d}x = \frac{1}{2i}\sqrt{\frac{\pi}{m}}\,\mathrm{erf}\left(i\sqrt{m}\right) \tag{2.75}$$

and

$$m \equiv \frac{3}{2}\frac{US}{k_\mathrm{B}T}. \tag{2.76}$$

Since S must satisfy both eqs. (2.8) and (2.74), it is necessarily a solution of

$$\begin{aligned} S &= \int f(\theta)\frac{1}{2}\left(3\cos^2\theta - 1\right)\mathrm{d}\Omega \\ &= -\frac{1}{2} + \frac{3}{2Z}\int_0^1 x^2\exp\left(mx^2\right)\mathrm{d}x \qquad (2.77)\\ &= -\frac{1}{2} + \frac{3}{2Z}\frac{\partial Z}{\partial m}. \qquad (2.78)\end{aligned}$$

One way of solving this equation for $S(T)$ is interpreting eq. (2.77) as the map

$$g(S) = -\frac{1}{2} + \frac{3}{2Z(S,T)} \int_0^1 x^2 \exp\Big(m(S,T)x^2\Big)\,\mathrm{d}x \tag{2.79}$$

with Z and m according to eqs. (2.75)–(2.76) and calculating the stable fixed points within $S \in [0,1]$ numerically. The results are plotted in figure 2.10. At critical temperature $k_\mathrm{B}T_\mathrm{c} \approx 0.22\,U$ the order parameter drops to 0.

2.6.2 Landau-De Gennes Theory

The isotropic-nematic transition may be modeled purely in terms of the tensor order parameter. The Landau-de Gennes theory is based on a mean field analysis and assumes that the order parameter is constant in space and small in the nematic phase close to the phase boundary. In the isotropic phase it should vanish on average, but may be subject to significant fluctuations. We can, therefore, expand the difference in bulk free energy density in terms of the order parameter. Assuming that there are no external fields impacting the alignment, the expansion reads [27]

$$F_\mathrm{B} = \frac{1}{2}a(T)Q_{ij}Q_{ji} - \frac{1}{3}b(T)Q_{ij}Q_{jk}Q_{ki} + \frac{1}{4}c(T)(Q_{ij}Q_{ji})^2 + \mathcal{O}\Big(Q_{ij}^5\Big). \tag{2.80}$$

The linear term vanishes, since Q_{ij} is traceless. NLCs are not invariant under transformations $S \mapsto -S$ and equivalently $Q_{ij} \mapsto -Q_{ij}$. This makes an odd power term necessary. It needs to be negative, because the equilibrium order parameter is positive. With the presence of a third order term we require a fourth order term to bound the free energy from below. Note, that other third and fourth order terms are either linearly dependent on the ones present in eq. (2.80) or vanish. Consider as an example the identity $2Q_{ij}Q_{jk}Q_{kl}Q_{li} = (Q_{ij}Q_{ji})^2$. Higher orders may be taken into account, but are not needed for uniaxial nematics [27,49]. Since we did the series expansion in terms of the order parameter, this expression for the free energy is invariant under all transformations permitted by nematic symmetry, as required. de Gennes postulated that both b and c are mostly independent of temperature and the transition is driven by $a = A(T - T^*)$, which vanishes at the supercooling temperature T^*.

In uniaxial nematics we can substitute $\boldsymbol{Q}$ with its expression in terms of S [eq. (2.12)] so that eq. (2.80) reduces to

$$F_\mathrm{B} = \frac{3}{4}aS^2 - \frac{1}{4}bS^3 + \frac{9}{16}cS^4. \tag{2.81}$$

The minimum is the root of a quadratic polynomial and gives the equilibrium order parameter

$$S_\mathrm{eq} = \begin{cases} \frac{b}{6c} + \frac{1}{2}\sqrt{\left(\frac{b}{3c}\right)^2 - \frac{8a}{3c}} & \text{if } a < a_c \\ 0 & \text{if } a > a_c \end{cases} \tag{2.82}$$

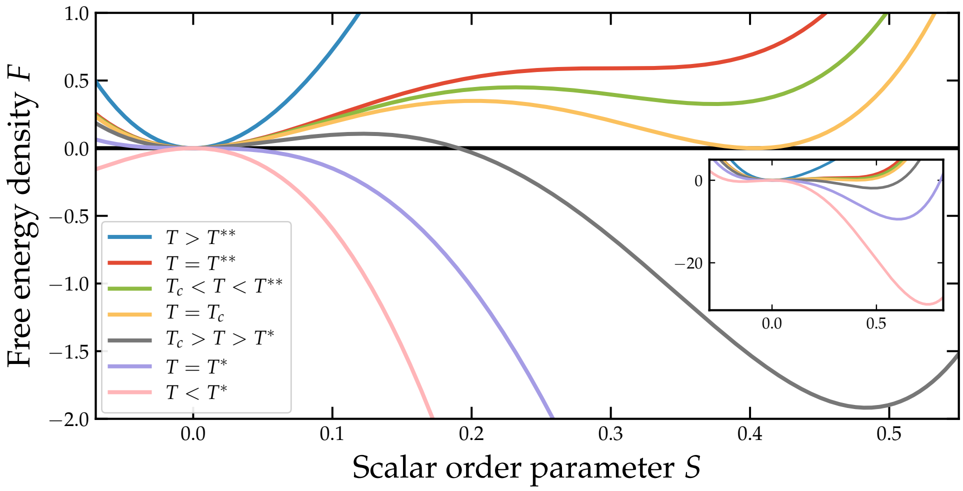

Figure 2.11: The free energy density F as a function of the order parameter S at different temperatures close to the critical point. F is given in arbitrary dimensionless units.

for the critical parameter $a_c = b^2/27c$, or, equivalently, the critical temperature $T_c = T^* + b^2/27Ac$. These solutions correspond to the isotropic phase ($S_{\text{eq}} = 0$) and the nematic phase ($S_{\text{eq}} > 0$).

Figure 2.11 shows the free energy minima at various temperatures. As the system cools down from the isotropic state, at first, a metastable, nematic solution $S > 0$ appears. This happens at the superheating temperature

$$T^{**} = T_c + \frac{B^2}{32aC}. \tag{2.83}$$

At critical temperature T_c the solution $S > 0$ becomes stable. The change of the absolute energy minimum from the isotropic state to the nematic state is discontinuous. The figure makes apparent how the first-order nature of the transition arises from the presence of the third order term in the free energy. Below T_c the isotropic state remains metastable, until the supercooling temperature T^* is reached. In this way the isotropic-nematic transition exhibits hysteresis.

2.7 Nematodynamics

So far we have discussed the equilibrium phase transition between the isotropic and the nematic state. We now introduce the principle of a hydrodynamic theory to study the flow of NLCs: the so-called nematodynamics.

The most commonly used macroscopic model of nematodynamics was developed by Ericksen [50, 51] and Leslie [52, 53] in the early 1960s. It was based on the static theory of NLCs established by Oseen [54] and Zöcher [55] 30 years earlier.

The dynamics of NLCs can be described using the Navier-Stokes equations

$$\rho \frac{\mathrm{d}}{\mathrm{d}t} v_i = \frac{\rho \tau_f}{3} \partial_j \left[\delta_{ij} \left(1 - 3\partial_\rho P_0 \right) \partial_k v_k + 2D_{ij} \right] + \sigma_{ij,j}, \tag{2.84}$$

modified by an extra stress tensor σ_{ji} that is defined up to a transformation $\sigma_{ji} \mapsto \sigma_{ji} + \nu_{ji}$ with $\nu_{ji,j} \equiv 0$. Here, τ_f is the kinematic viscosity. The stress is generally separated into the equilibrium or Ericksen stress $\boldsymbol{\sigma}^{\mathrm{e}}$ and the viscous stress $\boldsymbol{\sigma}'$

$$\sigma_{ji} = \sigma^{\mathrm{e}}_{ji} + \sigma'_{ji}. \tag{2.85}$$

There have been multiple approaches to expressing the stress tensor that arrive at equivalent descriptions of the observables. The approach described below is based on F.M. Leslie's [52, 53], I.W. Stewart's [56], and S. Chandrasekhar's [57] works. Unlike Ericksen and Leslie we assume the temperature to be constant in this examination. The model explored here uses the director as the fundamental quantity and is only valid in the absence of topological defects [27]. In section 2.7.4 we will discuss the approach by Beris and Edwards [33, 58] that is based on the tensor order parameter that is capable of modeling large variations in S, including defects.

Compared to ordinary liquids, NLCs have additional degrees of freedom in the director $\mathbf{n}$. Forces in the fluid not only influence its velocity field, but also cause rotations of the director. For this reason it is useful to study the local angular velocity of the director $\mathbf{w}$, defined such that $\dot{\mathbf{n}} = \mathbf{w} \times \mathbf{n}$. As we will see later, a Lagrangian perspective of this angular velocity is often more useful. We, therefore, define the relative angular velocity

$$\mathbf{W} = \mathbf{w} - \widehat{\mathbf{w}} \tag{2.86}$$

with respect to the local angular velocity

$$\widehat{\mathbf{w}} = \frac{1}{2} \boldsymbol{\nabla} \times \mathbf{v}, \tag{2.87}$$

which describes the rotation of the fluid element. This motivates the definition of the co-rotational time flux of the director

$$\mathbf{N} = \mathbf{W} \times \mathbf{n} = \dot{\mathbf{n}} - \boldsymbol{\omega} \mathbf{n}. \tag{2.88}$$

Here, we separated the velocity gradient tensor into the vorticity tensor $\boldsymbol{\omega}$ (anti-symmetric)

$$\omega_{ij} = \frac{1}{2} \left(v_{i,j} - v_{j,i} \right), \tag{2.89}$$

and rate of strain tensor $\boldsymbol{D}$ (symmetric)

$$D_{ij} = \frac{1}{2} \left(v_{i,j} + v_{j,i} \right), \tag{2.90}$$

and used the identity

$$\boldsymbol{\omega} \mathbf{x} = \widehat{\mathbf{w}} \times \mathbf{x}, \quad \forall \mathbf{x} \in \mathbb{R}^3. \tag{2.91}$$

2.7.1 Conservation Laws

The conservation laws of NLCs are very similar to the familiar equations of hydrodynamics for an ordinary fluid. They deviate only in terms of the director $\mathbf{n}$. We will consider a volume V of incompressible LCs, bounded by the surface A. Incompressibility requires

$$v_{i,i} = 0 \tag{2.92}$$

of the velocity $\mathbf{v}(\mathbf{r})$. Within the volume we have conservation of mass

$$\frac{\mathrm{d}}{\mathrm{d}t}\int_V \rho \,\mathrm{d}V = 0, \tag{2.93}$$

and conservation of momentum

$$\frac{\mathrm{d}}{\mathrm{d}t}\int_V \rho v_i \,\mathrm{d}V = \int_V f_i \,\mathrm{d}V + \oint_A \sigma_{ji} \,\mathrm{d}A_j\,, \tag{2.94}$$

where ρ is the density, f_i is the body force per unit volume. Under the assumption that there are no heat sources or sinks, conservation of energy states that [50]

$$\frac{\mathrm{d}}{\mathrm{d}t}\int_V \left(\frac{1}{2}\rho v_i v_i + \frac{1}{2}\rho_I \dot{n}_i \dot{n}_i + U\right) \mathrm{d}V = \int_V \left(f_i v_i + G_i \dot{n}_i\right) \mathrm{d}V + \oint_A \left(t_i v_i + s_i \dot{n}_i\right) \mathrm{d}A\,, \tag{2.95}$$

where ρ_I is a material constant representing a moment of inertia density, U is the internal energy density, G_i is the external director body force due to external magnetic fields, $t_i = \sigma_{ji} e_j$ the surface force per unit area acting across the plane with unit normal e_j, $s_i = \pi_{ji} e_j$ the director surface force, and π_{ji} the elasticity tensor. The left hand side represents the time derivative of the total energy with a term for kinetic energy related to linear movement, kinetic energy of rotation, and internal energy. The right hand side lists the external forces. These either fall in the category of body forces acting on the whole volume, or surface forces, causing stresses that originate at the interface of the volume. For both categories there is the standard hydrodynamic term including the convective velocity field v_i and a nematic term for forces that act on the orientations of the molecules. Since $\mathbf{n}$ is defined to be a unit vector, the latter forces only manifest as torques $\boldsymbol{\tau}_G \,\mathrm{d}V$, $\boldsymbol{\tau}_s \,\mathrm{d}A$, with $G_i \dot{n}_i = \mathbf{G} \cdot (\mathbf{w} \times \mathbf{n}) = \mathbf{w} \cdot (\mathbf{n} \times \mathbf{G}) \equiv \mathbf{w} \cdot \boldsymbol{\tau}_G$ and analogously $s_i \dot{n}_i \equiv \mathbf{w} \cdot \boldsymbol{\tau}_s$. Conservation of angular momentum states that [50]

$$\begin{aligned}\frac{\mathrm{d}}{\mathrm{d}t}\int_V &\left(\rho \epsilon_{ijk} r_j v_k + \rho_I \epsilon_{ijk} n_j \dot{n}_k\right) \mathrm{d}V \\ &= \int_V \left(\epsilon_{ijk} r_j f_k + \epsilon_{ijk} n_j G_k\right) \mathrm{d}V + \oint_A \left(\epsilon_{ijk} r_j t_k + \epsilon_{ijk} n_j s_k\right) \mathrm{d}A\,. \end{aligned} \tag{2.96}$$

Similarly to the energy balance, the left hand side gives the time derivative of the total angular momentum. It has a component related to the bulk movement of the fluid and a component related to the rotation of the individual molecules. The right hand side lists both the hydrodynamic torques, as well as $\boldsymbol{\tau}_G \,\mathrm{d}V$ and $\boldsymbol{\tau}_s \,\mathrm{d}A$. Finally, we have Oseen's equation [54]

$$\int_V \rho_I \ddot{n} \,\mathrm{d}V = \int_V (G_i + h_i) \,\mathrm{d}V + \oint_A \pi_{ji} \,\mathrm{d}A_j \,, \tag{2.97}$$

where h_i is the internal director body force, also called the molecular field. It is the torque balance for NLCs. Equation (2.97) includes viscous terms with G_i and h_i and an elastic term, determined by π_{ji}. Applying Stokes' law, equations (2.93)–(2.97) simplify to

$$\dot{\rho} = 0, \tag{2.98}$$

$$\rho \dot{v}_i = f_i + \sigma_{ji,j}, \tag{2.99}$$

$$\dot{U} = \sigma_{ji} D_{ij} + \pi_{ji} N_{ij} - h_i N_i, \tag{2.100}$$

$$\rho_I \ddot{n}_i = G_i + h_i + \pi_{ji,j}, \tag{2.101}$$

$$\sigma_{ji} - \pi_{kj} n_{i,k} + h_j n_i = \sigma_{ij} - \pi_{ki} n_{j,k} + h_i n_j, \tag{2.102}$$

in their differential forms. Here, we used the definition in eq. (2.90) for D_{ij} and the definition in eq. (2.88) for N_i. N_{ij} is analogously defined by

$$\boldsymbol{N} = \boldsymbol{\nabla} \dot{\mathbf{n}} - \boldsymbol{\omega}(\boldsymbol{\nabla} \mathbf{n}). \tag{2.103}$$

Changes in the orientation of the director are related to deformations of the LC. Hence, $n_{i,k}$ is called the curvature strain tensor.

2.7.2 Constitutive Equations

Let us now consider thermodynamic arguments that will provide us with another relation. The free energy density is

$$F = U - TS \tag{2.104}$$

with entropy S. The second law of thermodynamics may be stated as

$$\frac{\mathrm{d}}{\mathrm{d}t} \int_V S \,\mathrm{d}V \geq 0. \tag{2.105}$$

Applying this inequality to the internal energy density U in eq. (2.100) we obtain the condition

$$\sigma_{ji} D_{ij} + \pi_{ji} N_{ij} - h_i N_i - \dot{F} \geq 0 \tag{2.106}$$

for a system in isothermal equilibrium.

In order to arrive at constitutive equations for F, t_{ji}, π_{ji}, and h_i, some assumptions have to be made. If these quantities are single-valued in n_i, $n_{i,j}$, $\dot{n}_i$, and $v_{i,j}$, and are smooth enough, a first order expansion can be carried out with validity. Since $\dot{n}_i$ and $v_{i,j}$ are affected by superimposed rigid body rotations, they must be replaced by the reference-frame invariant N_i and D_{ij}. Therefore, our parameters are

$$n_i, \quad n_{i,j}, \quad N_i, \quad D_{ij}. \tag{2.107}$$

The expansion of the free energy density's temporal derivative with respect to these parameters is

$$\dot{F} = \frac{\partial F}{\partial n_i}\frac{\mathrm{d}n_i}{\mathrm{d}t} + \frac{\partial F}{\partial n_{i,j}}\frac{\mathrm{d}n_{i,j}}{\mathrm{d}t} + \frac{\partial F}{\partial N_i}\frac{\mathrm{d}N_i}{\mathrm{d}t} + \frac{\partial F}{\partial D_{ij}}\frac{\mathrm{d}D_{ij}}{\mathrm{d}t}. \tag{2.108}$$

Using eqs. (2.88) and (2.103) we can eliminate n_i and $n_{i,j}$

$$\begin{aligned}\dot{F} = \frac{\partial F}{\partial n_i}N_i + \frac{\partial F}{\partial n_i}n_j\omega_{ij} + \frac{\partial F}{\partial n_{i,j}}N_{ij} + \frac{\partial F}{\partial n_i}\dot{N}_i + \frac{\partial F}{\partial D_{ij}}\dot{D}_{ij} \\ - \frac{\partial F}{\partial n_{i,k}}n_{j,k}\omega_{ji} - \frac{\partial F}{\partial n_{k,j}}n_{ki}D_{ij} - \frac{\partial F}{\partial n_{k,i}}n_{k,j}\omega_{ji}.\end{aligned} \tag{2.109}$$

Subjecting this expansion to the entropy inequality (eq. (2.106)) and grouping coefficients we get

$$\begin{aligned}\left(\sigma_{ji} + \frac{\partial F}{\partial n_{k,j}}n_{ki}\right)D_{ij} + \left(\pi_{ji} - \frac{\partial F}{\partial n_{i,j}}\right)N_{ij} - \left(h_i + \frac{\partial F}{\partial n_i}\right)N_i \\ + \left(n_j\frac{\partial F}{\partial n_i} + n_{j,k}\frac{\partial F}{\partial n_{i,k}} + n_{k,j}\frac{\partial F}{\partial n_{k,i}}\right)\omega_{ji} - \left(\frac{\partial F}{\partial N_i}\right)\dot{N}_i - \left(\frac{\partial F}{\partial D_{ij}}\right)\frac{\mathrm{d}D_{ij}}{\mathrm{d}t} \geq 0.\end{aligned} \tag{2.110}$$

Since N_{ij} and $\dot{N}_i$ can be varied arbitrarily and independently, their coefficients must vanish, therefore,

$$\frac{\partial F}{\partial N_i} = 0, \quad \text{and} \quad \pi_{ji} - \frac{\partial F}{\partial n_{i,j}} = 0. \tag{2.111}$$

The symmetries of D_{ij} and ω_{ji} make the constraints on their coefficients less stringent

$$\frac{\partial F}{\partial D_{ij}} + \frac{\partial F}{\partial D_{ji}} = 0, \tag{2.112}$$

$$\left(n_j\frac{\partial F}{\partial n_i} + n_{j,k}\frac{\partial F}{\partial n_{i,k}} + n_{k,j}\frac{\partial F}{\partial n_{k,i}}\right) - \left(n_i\frac{\partial F}{\partial n_j} + n_{i,k}\frac{\partial F}{\partial n_{j,k}} + n_{k,i}\frac{\partial F}{\partial n_{k,j}}\right) = 0. \tag{2.113}$$

By using $\pi_{ji} = \frac{\partial F}{\partial n_{i,j}}$ [eq. (2.111)] and the $n_{i,k}$-symmetry in eq. (2.113) we may reduce eq. (2.102) to

$$\sigma_{ji} + h_j n_i = \sigma_{ij} + h_i n_j. \tag{2.114}$$

Eqs. (2.110)–(2.113) leave us with the inequality

$$\left(\sigma_{ji} + \frac{\partial F}{\partial n_{k,j}}n_{k,i}\right)D_{ij} - \left(h_i + \frac{\partial F}{\partial n_i}\right)N_i \geq 0. \tag{2.115}$$

We now separate the stress tensor [eq. (2.85)], and analogously the internal director body force into an equilibrium part and a viscous part

$$h_i = h_i^{\mathrm{e}} + h_i'. \tag{2.116}$$

Plugging both into eq. (2.115) yields

$$\left(\sigma_{ji}^{\mathrm{e}} + \frac{\partial F}{\partial n_{k,j}} n_{k,i}\right) D_{ij} - \left(h_i^{\mathrm{e}} + \frac{\partial F}{\partial n_i}\right) N_i + \left(\sigma_{ji}' D_{ij} - h_i' N_i\right) \geq 0. \tag{2.117}$$

Since this inequality must hold under any circumstances and D_{ij} as well as N_i can be varied arbitrarily, independently of σ_{ji}^{e} and h_i^{e}, the respective coefficients must vanish

$$\sigma_{ji}^{\mathrm{e}} = -\frac{\partial F}{\partial n_{k,j}} n_{k,i}, \tag{2.118}$$

$$h_i^{\mathrm{e}} = -\frac{\partial F}{\partial n_i}. \tag{2.119}$$

The hydrodynamic parts σ_{ji}' and h_i' are not involved, because they, D_{ij}, and N_i are interdependent. Plugging eqs. (2.118) and (2.119) into eq. (2.117), the inequality states

$$\sigma_{ji}' D_{ij} - h_i' N_i \geq 0. \tag{2.120}$$

As we established at the beginning of section 2.7, equation (2.84) is invariant under certain transformations of the stress tensor. Specifically, σ is defined irrespective of an arbitrary pressure p. Analogously, eq. (2.100) shows that the temporal change rate in free energy density $\dot{F}$ is invariant under transformations

$$\left(g_0^{\mathrm{e}}, \pi_{ij}\right) \mapsto \left(g_0^{\mathrm{e}} + \gamma n_i - n_{i,j}\beta_j, \pi_{ij} + \beta_i n_j\right),$$

with arbitrary constants γ and β_i. Thus, the generalized versions of eqs. (2.111), (2.118), and (2.119) read

$$\pi_{ji} = \beta_i n_j + \frac{\partial F}{\partial n_{i,j}}, \tag{2.121}$$

$$\sigma_{ji}^{\mathrm{e}} = -p\delta_{ji} - \frac{\partial F}{\partial n_{k,j}} n_{k,i}, \tag{2.122}$$

$$h_i^{\mathrm{e}} = \gamma n_i - n_{i,j}\beta_j - \frac{\partial F}{\partial n_i}. \tag{2.123}$$

2.7.3 Coefficients of Viscosity

The remaining parts of the stress tensor and the intrinsic director body force contain the viscous contributions. Like the free energy density in section 2.7.2, Ericksen expanded them in terms of n_i, N_i, and D_{ij}. Due to the symmetries of uniaxial nematics σ'_{ji} and h'_i have to be isotropic in these variables and even in $\mathbf{n}$. The required reference-frame independence implies that σ'_{ji} is a hemitropic function (invariant relative to a proper orthogonal group) of n_i, N_i, and D_{ij} [56]. Experiments by Miesowicz [59] and Zwetkoff [60] suggested linearity in N_i and D_{ij}, motivating Ericksen's ansatz [50]

$$\sigma'_{ji} = A^0_{ji} + A^1_{jik} N_k + A^2_{jikm} D_{km}, \tag{2.124}$$

$$h'_i = B^0_i + B^1_{ij} N_j + B^2_{ijk} D_{jk}. \tag{2.125}$$

The A^p and B^p are functions of n_i. Assuming that these equations are invariant under reflections through all planes containing n_i implies that the A^p and B^p are transversely isotropic tensors with respect to n_i [50]. Tensors with this property can be expressed as a linear combination of dyadic products of n_i and δ_{ij} [61]. Therefore in their most general forms the coefficients read

$$\begin{aligned}
A^0_{ji} &= \mu_0 \delta_{ji} + \mu_1 n_j n_i, \\
A^1_{jik} &= \mu_2 \delta jin_k + \mu_3 \delta_{jk} n_i + \mu_4 \delta_{ik} n_j + \mu_5 n_i n_j n_k, \\
A^2_{jikm} &= \mu_6 \delta_{ji} n_k n_m + \mu_7 n_j n_m \delta_{ik} + \mu_8 n_i n_j \delta_{km} + \mu_9 \delta_{jk} n_i n_m \\
&\quad + \mu_{10} \delta_{jm} n_i n_k + \mu_{11} \delta_{im} n_j n_k + \mu_{12} \delta_{ji} \delta_{km} \\
&\quad + \mu_{13} \delta_{jk} \delta_{im} + \mu_{14} n_i n_j n_k n_m, \\
B^0_i &= \gamma_0 n_i, \\
B^1_{ij} &= \gamma_1 \delta_{ij} + \gamma_2 n_i n_j, \\
B^2_{ijk} &= \gamma_3 \delta_{ij} n_k + \gamma_4 \delta_{ik} n_j + \gamma_5 \delta_{jk} n_i + \gamma_6 n_i n_j n_k.
\end{aligned}$$

Invoking the $\mathbf{n} \Leftrightarrow -\mathbf{n}$ symmetry or, more specifically, that the transformation

$$(n_i, N_i) \mapsto -(n_i, N_i)$$

implies

$$\sigma'_{ji} \to \sigma'_{ji} \quad \text{and} \quad h'_i \to -h'_i$$

and using $n_i N_i = 0$ as well as incompressibility $D_{ii} = 0$, we can reduce the number of coefficients

$$\begin{aligned}
\sigma'_{ji} &= (\mu_0 + \mu_6 D_{km} n_k n_m) \delta_{ji} + (\mu_1 + \mu_{14} D_{km} n_k n_m) n_i n_j + \mu_{13} D_{ji} \\
&\quad + \mu_{15} D_{kj} n_i n_k + \mu_{16} D_{ki} n_j n_k + \mu_3 n_i N_j + \mu_4 n_j N_i,
\end{aligned} \tag{2.126}$$

$$h'_i = \big(\gamma_0 + \gamma_6 D_{kj} n_k n_j\big) n_i + \gamma_9 D_{ik} n_k + \gamma_1 N_i, \tag{2.127}$$

where

$$\mu_{15} = \mu_9 + \mu_{10}, \quad \mu_{16} = \mu_7 + \mu_{11}, \quad \text{and} \quad \gamma_9 = \gamma_3 + \gamma_4. \tag{2.128}$$

Another constraint is given by eq. (2.114)

$$\gamma_6 = \mu_{16} - \mu_{15}, \quad \gamma_1 = \mu_4 - \mu_3. \tag{2.129}$$

The entropy inequality (2.120) dictates that

$$\mu_1 n_i n_j D_{ij} + h(D_{ij}, N_i, n_i) \geq 0, \tag{2.130}$$

where h is a function quadratic in D_{ij} and N_i. Since D_{ij} can be varied independently, the coefficient μ_1 must vanish. Because of the imposed incompressibility the coefficient of δ_{ji} (that is $-p$) in σ'_{ji} and the coefficient of n_i (that is γ) in h'_i are arbitrary. They do not contribute to the hydrodynamics and may be included in the equilibrium parts σ^{e}_{ji} and h^{e}_i, instead. Renaming to coefficients

$$\begin{aligned} \alpha_1 &= \mu_{14} & \alpha_2 &= \mu_4 \\ \alpha_3 &= \mu_3 & \alpha_4 &= \mu_{13} \\ \alpha_5 &= \mu_{16} & \alpha_6 &= \mu_{15} \\ \lambda_1 &= \gamma_1 & \lambda_2 &= \gamma_9 \end{aligned}$$

we arrive at our final description of the viscous stress tensor and intrinsic director body force

$$\sigma'_{ji} = \alpha_1 n_k D_{km} n_m n_j n_i + \alpha_2 n_j N_i + \alpha_3 n_i N_j + \alpha_4 D_{ji} + \alpha_5 n_j n_k D_{ki} + \alpha_6 n_i n_k D_{kj}, \tag{2.131}$$

$$h'_i = \lambda_1 N_i + \lambda_2 n_j D_{ji}. \tag{2.132}$$

The full quantities then combine to

$$\begin{aligned} \sigma_{ji} = -p\delta_{ji} - \frac{\partial F}{\partial n_{k,j}} n_{k,i} + \alpha_1 n_k n_m D_{km} n_i n_j + \alpha_2 n_j N_i \\ + \alpha_3 n_i N_j + \alpha_4 D_{ji} + \alpha_5 n_j n_k D_{ki} + \alpha_6 n_i n_k D_{kj}, \end{aligned} \tag{2.133}$$

$$h_i = \gamma n_i - \beta_j n_{i,j} - \frac{\partial F}{\partial n_i} + \lambda_1 N_i + \lambda_2 n_j D_{ji}. \tag{2.134}$$

From the time-reversal invariance of the equations of motion of individual particles, in 1969, Parodi [62] derived the relation

$$\alpha_2 + \alpha_3 = \alpha_6 - \alpha_5 \tag{2.135}$$

between the viscosity coefficients. Thus, the viscosity of NLCs is described by five independent coefficients. They must conform to the entropy inequality [eq. (2.120)]. Substituting eqs. (2.131) and (2.132) in (2.120) we get an inequality that implies [52]

$$\begin{cases} \alpha_4 \geq 0, \\ 2\alpha_1 + 3\alpha_4 + 2\alpha_5 + 2\alpha_6 \geq 0, \\ 2\alpha_4 + \alpha_5 + \alpha_6 \geq 0, \\ \alpha_3 - \alpha_2 \geq 0, \\ 4(\alpha_3 - \alpha_2)(2\alpha_4 + \alpha_5 + \alpha_6) \geq (\alpha_2 + \alpha_3 + \alpha_6 - \alpha_5)^2. \end{cases} \tag{2.136}$$

The coefficients α_i are called Leslie viscosities and can—to varying degrees—be interpreted physically. α_4 corresponds to the ordinary dynamic viscosity, also found in isotropic Newtonian fluids. The other coefficients have no counterparts in isotropic fluids and give rise to the non-Newtonian properties of LCs. $\gamma_1 \equiv \alpha_3 - \alpha_2$ is called the rotational or twist viscosity and is a measure of the director's relaxation rate. $\gamma_2 \equiv \alpha_2 + \alpha_3$ is called the torsion coefficient and characterizes the coupling between the director and the shear flow.

2.7.4 Beris-Edwards Formulation

A generalization of nematodynamics that captures nematic behavior in the proximity of topological defects is the Beris-Edwards model. It uses the free energy density given in sections 2.4 and 2.6. In the one-constant approximation we can sum the distortion term [eq. (2.37)] and the bulk contribution [eq. (2.80)] to obtain

$$F = \frac{a}{2} Q_{ij} Q_{ji} - \frac{b}{3} Q_{ij} Q_{jk} Q_{ki} + \frac{c}{4} \left(Q_{ij} Q_{ji} \right)^2 + \frac{L}{2} Q_{ij,k}^2 \tag{2.137}$$

with material constants b and c, as well as temperature dependent a. The total free energy density is given by

$$F_{\text{tot}} = \frac{1}{2} v_i^2 + \Psi_{\text{ext}} + F, \tag{2.138}$$

where Ψ_{ext} represents the influence of outside fields. A magnetic field B_i and magnetic susceptibility χ, for example, imply $\Psi_{\text{ext}} = -\chi B_i B_j Q_{ij}/2$ [33]. The order parameter $\boldsymbol{Q}$ minimizes the free energy over time. In the absence of flow, its time derivative $\dot{\boldsymbol{Q}}$ is therefore proportional to the negative gradient of F with respect to $\boldsymbol{Q}$. We define this negative gradient as the molecular field

$$H_{ij} = -\frac{\delta F}{\delta Q_{ij}} + \frac{1}{3} \delta_{ij} \operatorname{Tr} \frac{\delta F}{\delta Q_{ij}}. \tag{2.139}$$

Analogously to $\mathbf{h}$ in Ericksen-Leslie theory, it gives the internal director body force. In addition, however, it also contains the internal force acting on the scalar order parameter S. Since $\boldsymbol{Q}$ remains traceless in time, transitively $\boldsymbol{H}$ has to be defined as traceless. In the one-constant approximation the molecular field is

$$\boldsymbol{H} = -a\boldsymbol{Q} + b\left(\boldsymbol{Q}^2 - \boldsymbol{I} \frac{1}{3} \operatorname{Tr} \boldsymbol{Q}^2 \right) - c\boldsymbol{Q} \operatorname{Tr} \boldsymbol{Q}^2 + L\nabla^2 \boldsymbol{Q}. \tag{2.140}$$

In the absence of flow the order parameter evolves in time according to $\dot{\boldsymbol{Q}} = \Gamma \boldsymbol{H}$ with collective rotational diffusion constant Γ. Through the use of a generalized Poisson bracket Beris, Edwards, and Grmela [33] were able to show that, for the full free energy, that takes flow into account, the time evolution of the order parameter is given by

$$\frac{\mathrm{d}}{\mathrm{d}t} \boldsymbol{Q} - \boldsymbol{S} = \Gamma \boldsymbol{H} \tag{2.141}$$

with a generalized advection term

$$S_{ij} = (\xi D_{ik} + \omega_{ik})(Q_{kj} + \delta_{kj}/3) + (Q_{ik} + \delta_{ik}/3)(\xi D_{kj} - \omega_{kj}) \\ - 2\xi(Q_{ij} + \delta_{ij}/3)Q_{kl}v_{l,k}. \quad (2.142)$$

It couples the order parameter to the flow, allowing it to be rotated and stretched by flow gradients. For a passive nematic they calculated the stress tensor, obeying the momentum equation [eq. (2.84)]

$$\rho \frac{\mathrm{d}}{\mathrm{d}t} v_i = \frac{\rho \tau_f}{3} \partial_j \left[\delta_{ij} (1 - 3\partial_\rho P_0) \partial_k v_k + 2D_{ij} \right] + \sigma_{ij,j}, \quad (2.143)$$

to be

$$\sigma_{ij} = \lambda_{ij} + \tau_{ij}. \quad (2.144)$$

with symmetric part

$$\lambda_{ij} = -P_0 \delta_{ij} - \xi H_{ik}(Q_{kj} + \delta_{kj}/3) - \xi(Q_{ik} + \delta_{ik}/3)H_{kj} \\ + 2\xi(Q_{ij} + \delta_{ij}/3)Q_{kl}H_{kl} - Q_{kl,j}\frac{\delta F}{\delta Q_{kl,i}}, \quad (2.145)$$

and antisymmetric part

$$\tau_{ij} = \left(Q_{ik}H_{kj} - H_{ik}Q_{kj} \right). \quad (2.146)$$

The hydrostatic pressure is given by

$$P_0 = \rho T - \frac{L}{2} Q_{ij,k}^2. \quad (2.147)$$

We will show that these equations reduce to Ericksen Leslie nematodynamics for a uniaxial NLC, if the scalar order parameter S is constant. For reasons of simplicity, here, we only consider elastic forces in the one-constant approximation. In section 2.4 we already saw that the descriptions of the elastic free energy, and consequently, the equilibrium molecular field are equivalent, if the elastic constants fulfill eq. (2.51) $L = K/2S^2$. Throughout the comparison we make use of this condition, and neglect terms proportional to n_i, since they only regulate the normalization and don't contribute to the dynamics. Applying eq. (2.141) to a uniaxial NLC, which has order parameter $\boldsymbol{Q}$ according to eq. (2.12), yields the molecular field

$$\Gamma H_{ij} = S\left(n_j N_i + n_i N_j\right) - S\xi\left(D_{ik}n_k n_j + n_i n_k D_{kj}\right) \\ + \frac{2}{3}(S-1)\xi D_{ij} + 2S^2 \xi n_i n_j D_{kl} n_l n_k + \frac{2}{3} S(1-S)\xi \delta_{ij} D_{kl} n_l n_k. \quad (2.148)$$

Its relationship to the Ericksen Leslie molecular field is given by the chain rule

$$h_i \equiv -\frac{\delta F}{\delta n_i} = -\frac{\delta F}{\delta Q_{jk}} \frac{\delta Q_{jk}}{\delta n_i} = S\left(H_{ij} n_j + n_j H_{ji}\right). \quad (2.149)$$

Plugging eq. (2.148) into eq. (2.149), we get the expression

$$h_i = \frac{2S^2}{\Gamma} N_i - \frac{2}{3\Gamma} S(S+2)\xi n_j D_{ji}, \tag{2.150}$$

which has the same form as the viscous part of the Ericksen-Leslie molecular field. Comparison with eq. (2.132) yields the correspondence

$$\lambda_1 = \frac{2S^2}{\Gamma}, \tag{2.151}$$

$$\lambda_2 = -\frac{2}{3}\frac{S(S+2)\xi}{\Gamma}, \tag{2.152}$$

for the Ericksen-Leslie coefficients.

Lastly, we consider the stress tensor's components, individually. The isotropic part maps trivially between the two theories. From section 2.4 we also know the mapping of the elastic part proportional to $\delta F/\delta Q_{ij}$. The remaining, viscous, components of λ_{ij} are with the molecular field $\boldsymbol{H}$ according to eq. (2.148) for a uniaxial NLC

$$\begin{aligned} \Gamma\lambda_{ij} = & -\frac{S\xi}{3}(S+2)\left(n_j N_i + n_i N_j\right) + \frac{S\xi^2}{3}(4-S)\left(D_{ik}n_k n_j + n_i n_k D_{kj}\right) \\ & + \frac{2\xi^2}{3}(S-1)^2 D_{ij} - \frac{8S^2\xi^2}{3}\left(\frac{3}{4} + S - S^2\right)\xi n_i n_j D_{kl} n_l n_k. \end{aligned} \tag{2.153}$$

The antisymmetric part is under these conditions

$$\Gamma\tau_{ij} = S^2(n_i N_j - N_i n_j) - \frac{S(S+2)}{3\xi(n_i n_k D_{kj} - D_{ik} n_k n_j)}. \tag{2.154}$$

We see that their sum directly corresponds to eq. (2.131). Comparing the coefficients, we find the Leslie viscosities

$$\alpha_1 = -\frac{2}{3}\frac{S^2}{\Gamma}\left(3 + 4S - 4S^2\right)\xi^2 \tag{2.155}$$

$$\alpha_2 = \frac{1}{\Gamma}\left[-\frac{1}{3}S(2+S)\xi - S^2\right] \tag{2.156}$$

$$\alpha_3 = \frac{1}{\Gamma}\left[-\frac{1}{3}S(2+S)\xi + S^2\right] \tag{2.157}$$

$$\alpha_4 = \frac{4}{9}\frac{(1-S)^2}{\Gamma}\xi^2 + \eta \tag{2.158}$$

$$\alpha_5 = \frac{1}{\Gamma}\left[\frac{1}{3}S(4-S)\xi^2 + \frac{1}{3}S(2+S)\xi\right] \tag{2.159}$$

$$\alpha_6 = \frac{1}{\Gamma}\left[\frac{1}{3}S(4-S)\xi^2 - \frac{1}{3}S(2+S)\xi\right]. \tag{2.160}$$

2.8 Active Nematics

Cellular organisms store energy in the form of adenosine-triphosphate (ATP). This energy is used to generate motion in the cytoskeleton by molecular motors such as kinesin and myosin. They catalyze the hydrolysis to adenosine-diphosphate (ADP) and a freed inorganic phosphate. Though the bonds in ATP are weak and require little energy to break, the total energy of ATP is much higher than that of the ADP+P pair [63]. On the length scale that our model operates on, we do not need to concern ourselves with the biochemical origin of the forces the molecular motors exert on the fluid, and can simply represent this additional source of force as an active stress tensor to include in the hydrodynamic balance of momentum [64–66]

$$\boldsymbol{\sigma}^{\mathrm{a}} \propto \boldsymbol{Q}. \tag{2.161}$$

with

$$\boldsymbol{\sigma} = \boldsymbol{\sigma}^{\text{passive}} + \boldsymbol{\sigma}^{\mathrm{a}}. \tag{2.162}$$

Since the energy producing hydrolysis is predicated on a chemical potential difference between ATP and ADP+P pairs, we may either quantify this potential through a local concentration c [67]

$$\boldsymbol{\sigma}^{\mathrm{a}} = -\Lambda c^2 \boldsymbol{Q} \tag{2.163}$$

that diffuses and is used up in the force production according to

$$\frac{\mathrm{d}}{\mathrm{d}t} c = \partial_i \Big(\mathcal{D}_{ij} \partial_j c + \Lambda' c^2 \partial_j Q_{ij} \Big) \tag{2.164}$$

with anisotropic diffusion tensor $\mathcal{D}_{ij} = \mathcal{D}_0 \delta_{ij} + \mathcal{D}_1 Q_{ij}$ and coefficient Λ', or assume global abundance

$$\boldsymbol{\sigma}^{\mathrm{a}} = -\Lambda \boldsymbol{Q}. \tag{2.165}$$

The active stress may be chosen as extensile ($\Lambda > 0$), as in suspensions of microtubule bundles and in most bacteria [68], or contractile ($\Lambda < 0$), as in actomyosin networks and in migrating cell layers [69].

In a uniaxial NLC the force that arises due to activity is

$$\begin{aligned} F_i^{\mathrm{a}} &\equiv -\partial_j \Lambda Q_{ij} = -\partial_j \Lambda \frac{3}{2} S \left(n_i n_j - \frac{1}{3} \delta_{ij} \right) \\ &= -\frac{3}{2} \Lambda \left[n_i n_j \partial_j S - \frac{1}{3} \partial_i S + S \big(n_i n_{j,j} + n_{i,j} n_j \big) \right]. \end{aligned} \tag{2.166}$$

It obviously vanishes in regions where $\boldsymbol{Q}$ is homogeneous. If the curvature strain tensor $n_{i,j}$ is large, and $\boldsymbol{\nabla} S$ is small, as is the case in very close proximity to defects, the active force is

$$\mathbf{F}^{\mathrm{a}} \Big|_{\boldsymbol{\nabla} S = 0} = -\frac{3 \Lambda S}{2} [\mathrm{Tr}(\boldsymbol{\nabla} \otimes \mathbf{n}) \mathbf{n} + (\boldsymbol{\nabla} \otimes \mathbf{n}) \cdot \mathbf{n}], \tag{2.167}$$

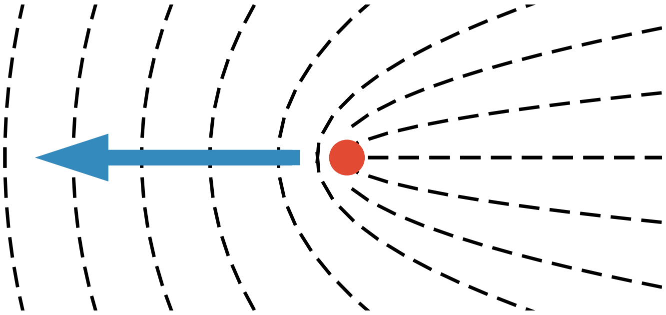

Figure 2.12: A $+1/2$ defect affected by extensile stress is propelled towards its head.

and acts predominantly parallel to $\mathbf{n}$. If, on the other hand, $n_{i,j}$ is small, i.e. the director only changes slowly in space, there is a force

$$\mathbf{F}^{\mathrm{a}}\Big|_{\boldsymbol{\nabla}\mathbf{n}=0} = -\frac{3\Lambda|\boldsymbol{\nabla}S|}{4}\left\{\left[\cos(2\vartheta)+\frac{1}{3}\right]\mathbf{q}+\sin(2\vartheta)\mathbf{p}\right\}, \tag{2.168}$$

which we decomposed into a component parallel to $\mathbf{q} \equiv \boldsymbol{\nabla}S/|\boldsymbol{\nabla}S|$ and an orthogonal component with $\mathbf{p} \perp \mathbf{q}$. It will tend to act parallel to $\boldsymbol{\nabla}S$, if the angle $\vartheta = \angle(\mathbf{n}, \boldsymbol{\nabla}S)$ is around 0, $\pi/2$, or π. If $\vartheta \approx \pi/4$ or $\vartheta \approx 3\pi/4$, the force $\mathbf{F}^{\mathrm{a}}$ and $\boldsymbol{\nabla}S$ are close to orthogonal. The active stress produces the greatest advective force in the presence of $+1/2$ defects. They are driven in a direction along their symmetry axis; for extensile stresses towards their 'heads', and for a contractile stress in the direction of their 'tails' (see figure 2.12).

There are multiple symmetry-based propositions for extra terms. In studying the rheology of active-particle suspensions, Hatwalne *et al.* found that higher order contributions to the stress tensor of the form $\boldsymbol{\sigma}^{\mathrm{a}} - 1/3\,\mathrm{Tr}(\boldsymbol{\sigma}^{\mathrm{a}})\boldsymbol{I} = -\Lambda\boldsymbol{Q} + \Lambda_2\boldsymbol{Q}^2 + \dots$ are allowed [65]. However, across the literature, these have mostly been neglected [6, 67, 69–72]. Secondly, the activity contributes directly to the time evolution of the order parameter through extra terms in eq. (2.141) [6, 65, 66]

$$\frac{\mathrm{d}}{\mathrm{d}t}\boldsymbol{Q} = \boldsymbol{S} + \Gamma\boldsymbol{H} + \lambda\boldsymbol{Q} + D_{\mathrm{a}}\nabla^2\boldsymbol{Q} + k_0\boldsymbol{D}. \tag{2.169}$$

Here, λ is an additional activity parameter, that is suggested to take the negative value $\lambda = -1/\tau_{\mathrm{a}}$ with activity correlation time τ_{a} in dilute bacterial suspensions [65], or negative values when describing concentrated actomyosin gels and other self-aligning systems [6, 66], similarly to Λ. This parameter is incorporated into some models of active nematics [6, 70]. The active diffusivity D_{a} and kinetic coefficient k_0 are generally ignored. The neglect of these terms is well-founded. For all three of them, terms of the same form are already present in the passive equations [65]. Therefore, including them only corresponds to a rescaling of the free energy [70]. The term $\lambda\boldsymbol{Q}$ is in principle present in our model and in our

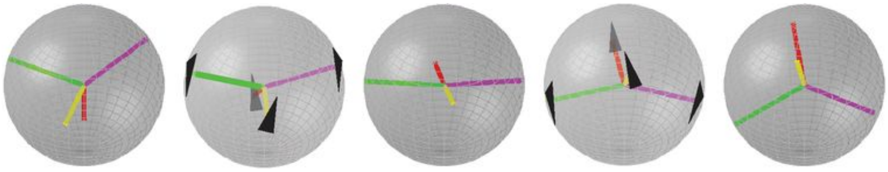

(a) Transition between tetrahedral (left, right) and planar (center) defect configurations.

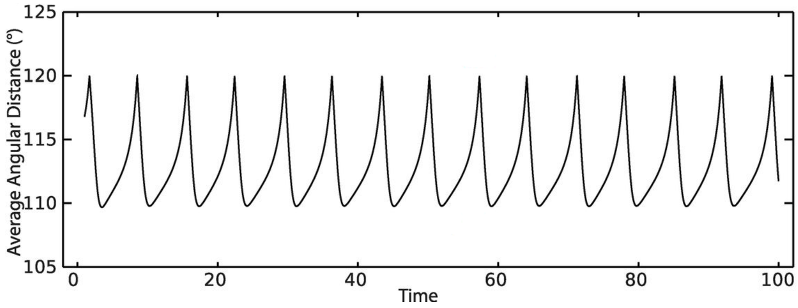

(b) The angular distance between the defects is taken pair-wise and averaged over.

Figure 2.13: An active NLC constrained to the surface of a lipid vesicle oscillates between a tetrahedral (109.5°) and a planar (120°) defect configuration. Image credits: [1].

algorithm (see chapter 3), but for the scope of this thesis we choose $\lambda = 0$, which matches the limit of infinite activity correlation time.

For large enough values of the activity, active nematic fluids exhibit the remarkable properties of spontaneous generation of topological defects. In such systems defects have been observed to move spontaneously and behave like self-propelled particles (see figure 2.12). In their seminal 2014 paper Keber *et al.* showed, how an active nematic film encapsulated by a shape-changing lipid vesicle can form a biomimetic material [1]. The initially spherical vesicle has a net topological charge of 2 and distributes it in the form of four $+1/2$ defects. Since they are repelled by one another, in equilibrium, they are positioned at the corners of an inscribed tetrahedron, maximizing their separation. When the microtubules comprising the nematic were supplied with an energy source in the form of ATP, the defects began to move. However, no new defects were formed, annihilated or fused, since the vesicle's diameter was below the length scale at which the system is unstable to bend deformations. The asymmetric shape of the $+1/2$ defects caused active stresses, that could not be compensated in the confinement while keeping the relative defect distances constant. As a result, the system oscillated between a tetrahedral and a planar defect configuration (see figure 2.13). The corresponding period time matched the time it would take a defect to orbit the vesicle. When they deflated the vesicle slightly, it started to fluctuate around a mean spherical shape, characterized by the extension and contraction of the major and minor axis of an ellipse. The period was, again, proportional to the activity. Additionally, four protrusions grew out of the vesicle. They became larger, as the bubble was deflated

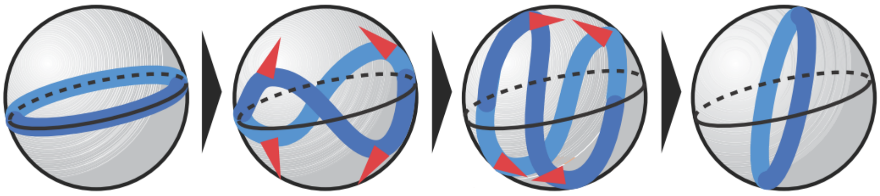

Figure 2.14: Schematic representation of the oscillation between an equatorial +2 defect and four +1/2 defects (orange triangles). Image credits: [1]

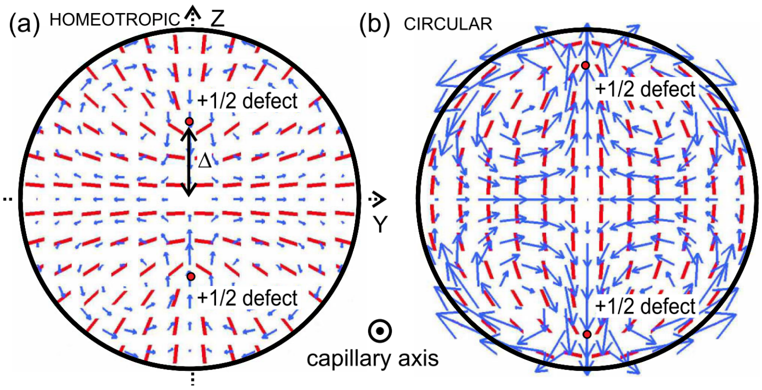

Figure 2.15: Local director (red) and active flow (blue) of a NLC in a cylinder with (**a**) homeotropic and (**b**) circular anchoring. Image credits: [70]

further. After a re-inflation, the original shape could be recovered. The dynamics were mainly governed by the activity parameter (ATP concentration), but switched between different dynamical modes, depending on the vesicle diameter. For small radii, for example, the microtubules formed a rotating, singular equatorial ring. The ring grew due to the active stresses and deformed, giving rise to four +1/2 defects. They collided in pairs, initiating the collapse into a new ring, that was rotated by $\pi/2$, compared to the original one (see figure 2.14).

Using a modified lattice Boltzmann algorithm, Ravnik and Yeomans [70] studied active nematic flows in a periodic cylindrical capillary. Similarly to the vesicle, a cylinder's topological properties can cause stable defects to emerge naturally, depending on the boundary conditions. Specifically, if the director is anchored parallel to the periodic (capillary) axis, no defects form. For any orthogonal type of anchoring the equilibrium configuration includes exactly two defects with charge +1/2. Their orientation depends on the angle between the anchoring direction and the surface. If the anchoring is homeotropic, their heads face inward. With parallel (circular) anchoring, their heads face outward (fig. 2.15). For homogeneous anchoring along the capillary axis, Ravnik and Yeomans observed three distinct active flow regimes. At low activity there was no flow at all, at medium activity a unidirectional flow formed along the capillary axis, and at high activity the flow became bidirectional (fig. 2.16). In the cylinder-plane a secondary flow, about two orders of magnitude weaker, emerged. In the second flow regime it showed 8 distinct vortices, and in the third one 4 vortices. For in-plane anchoring

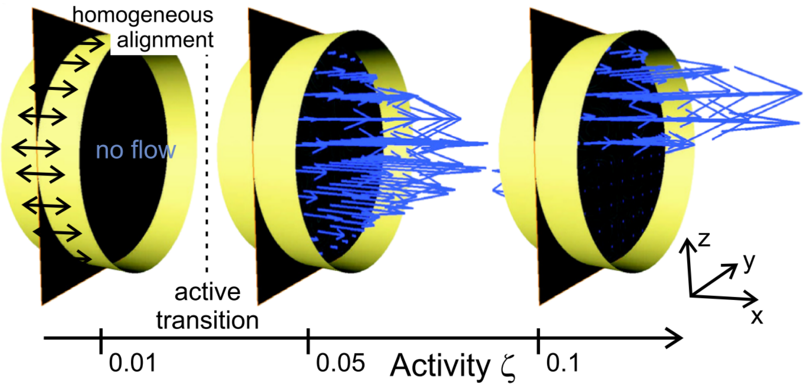

Figure 2.16: Regimes of active flow in a cylinder with homogeneous boundary conditions along the periodic axis. For increasing activity there are three different modes. A basic state with no flow (left), an excited state with unidirectional flow (middle), and a second excited state with bidirectional flow (right). The blue arrows indicate the flow velocity within the capillary (yellow). Image credits: [70]

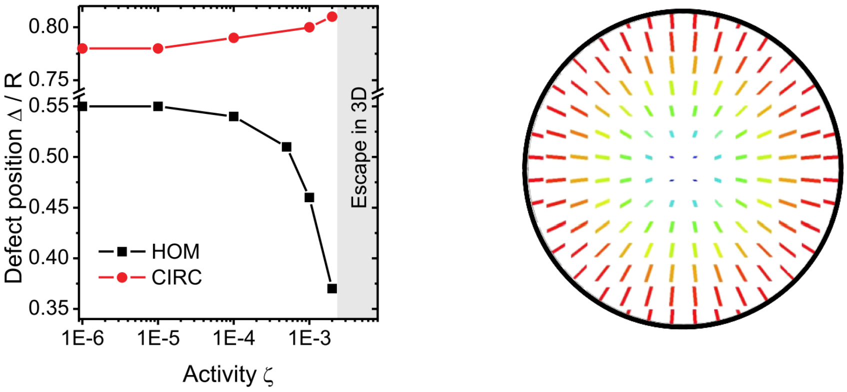

Figure 2.17: Position of the defects Δ compared to the capillary radius R as a function of the activity ζ for homeotropic and circular anchoring (left). At high activity the defects escape in the third dimension (right). Image credits: [70]

the in-plane flow began to form at much lower activity. The extensile active stress drove the defects in the directions of their heads. This deformed the director field, increasing the opposed elastic stress, and balancing out the system. The net effect was a change in the defects' stationary positions (see figure 2.17 on the left). As the activity rose higher, a globally, slowly deformed configuration became energetically favorable to the two local, severe deformations, and the defects escaped in the third dimension (fig. 2.17 on the right).

Chapter 3

Multiparticle Collision Dynamics

The computational complexity of particle dynamics can be greatly reduced, if the calculation of pair-wise interactions is avoided. On the basis of this idea Malevanets and Kapral proposed a new computational method in 1999 [73], that is now referred to as multiparticle collision dynamics (MPCD) or stochastic rotation dynamics (SRD).

The MPCD algorithm uses a bottom-up approach to reproduce fluid dynamics. Mass, momentum and energy are transported in the form of MPCD-'particles'. These particles are subjected to two alternating steps. In the streaming step they move ballistically. In the collision step they stochastically exchange velocities, conserving momentum and energy locally. Since particles are used, the positions and velocities take on continuous values. Only time and mass are discretized. The algorithm is well suited for mesoscale modeling, since it incorporates both the macroscopic hydrodynamic fields and thermal fluctuations, while remaining computationally efficient. We extended the algorithm to the domain of NLCs, using the Beris-Edwards formulation of nematodynamics.

3.1 Basic MPCD

We will start with a description of the basic MPCD algorithm for hydrodynamics. In a simulation there are $N \cdot L_x \cdot L_y \cdot L_z$ MPCD-particles i with positions $\mathbf{r}_i$, velocities $\mathbf{v}_i$, and unit masses. Initially, they are positioned uniformly at random within the simulation domain of dimensions $L_x \cdot L_y \cdot L_z$ and have Boltzmann-distributed velocities with dimensionless thermal energy E_{kT}. Time is discretized into time steps Δt. Each step is further separated into two stages. In the streaming step, each particle i moves balistically

$$\mathbf{r}_i(t + \Delta t) = \mathbf{r}_i(t) + \mathbf{v}_i(t)\Delta t, \tag{3.1}$$

only deviating from its straight path, if it encounters a domain boundary. This allows for the transport of mass, momentum and energy. Critically, in this step, the particles do not interact with one another.

The streaming step is complemented by the collision step. Here, the system is coarse grained into cells of unit length. In the resulting $L_x \cdot L_y \cdot L_z$ grid every cell is treated independently. There exist two main variations of the MPCD algorithm. We call the first one 'standard MPCD' or simply MPCD, and the second one SRD. In both, first, the center of mass velocity

$$\mathbf{v}^\alpha = \frac{1}{N_\alpha} \sum_{j \in \mathrm{cell}} \mathbf{v}_j, \tag{3.2}$$

is calculated. To conserve momentum, it has to be kept constant. The two algorithms differ in how they deal with the relative velocities $\mathbf{v}_i - \mathbf{v}^\alpha$. In standard MPCD an Andersen thermostat is applied. New relative velocities $\mathbf{v}_i^{\mathrm{ran}}$ are randomly generated from a normal distribution with variance E_{kT}. They are shifted to have exactly 0 mean, and substituted for the old ones

$$\mathbf{v}_i(t+\Delta t) = \mathbf{v}^\alpha(t) + \mathbf{v}_i^{\mathrm{ran}} - \frac{1}{N_C} \sum_{j \in \mathrm{cell}} \mathbf{v}_j^{\mathrm{ran}}. \tag{3.3}$$

In SRD the computationally costly generation of the N random numbers $\mathbf{v}_i^{\mathrm{ran}}$ is avoided. Instead, the relative velocities are rotated around a random axis $\mathbf{b}^\alpha$ by a fixed angle β. Defining $\boldsymbol{R}^\alpha$ as the corresponding rotation matrix, the SRD collision step is given by

$$\mathbf{v}_i(t+\Delta t) = \mathbf{v}^\alpha(t) + \boldsymbol{R}^\alpha(\mathbf{b}^\alpha, \beta)[\mathbf{v}_i(t) - \mathbf{v}^\alpha(t)]. \tag{3.4}$$

The angle β needs to have a value different from 0 and π (commonly $\pi/2$ or $2\pi/3$).

To keep particles from accumulating artificial correlations with their neighbors, the cell grid is shifted randomly for each collision step [74]. Figure 3.1 gives a schematic representation of the algorithm's core operations in a 2-dimensional system.

3.2 Angular Momentum Conservation

Both standard MPCD and SRD can be modified to conserve angular momentum in the collision step. In 2-dimensional SRD this is accomplished by choosing the rotation angle β in accordance to [75,76]

$$\sin\beta = -\frac{2AB}{A^2+B^2}, \quad \text{and} \quad \cos\beta = \frac{A^2-B^2}{A^2+B^2}, \tag{3.5}$$

where

$$A = \sum_{i=1}^{N_C} [\mathbf{r}_i \times (\mathbf{v}_i - \mathbf{u}_C)] \cdot \mathbf{m}, \quad \text{and} \quad B = \sum_{i=1}^{N_C} \mathbf{r}_i \cdot (\mathbf{v}_i - \mathbf{u}_C). \tag{3.6}$$

In 3 dimensions the calculation of the center of mass

$$\mathbf{r}^\alpha = \frac{1}{N_\alpha} \sum_{j \in \mathrm{cell}} \mathbf{r}_j \tag{3.7}$$

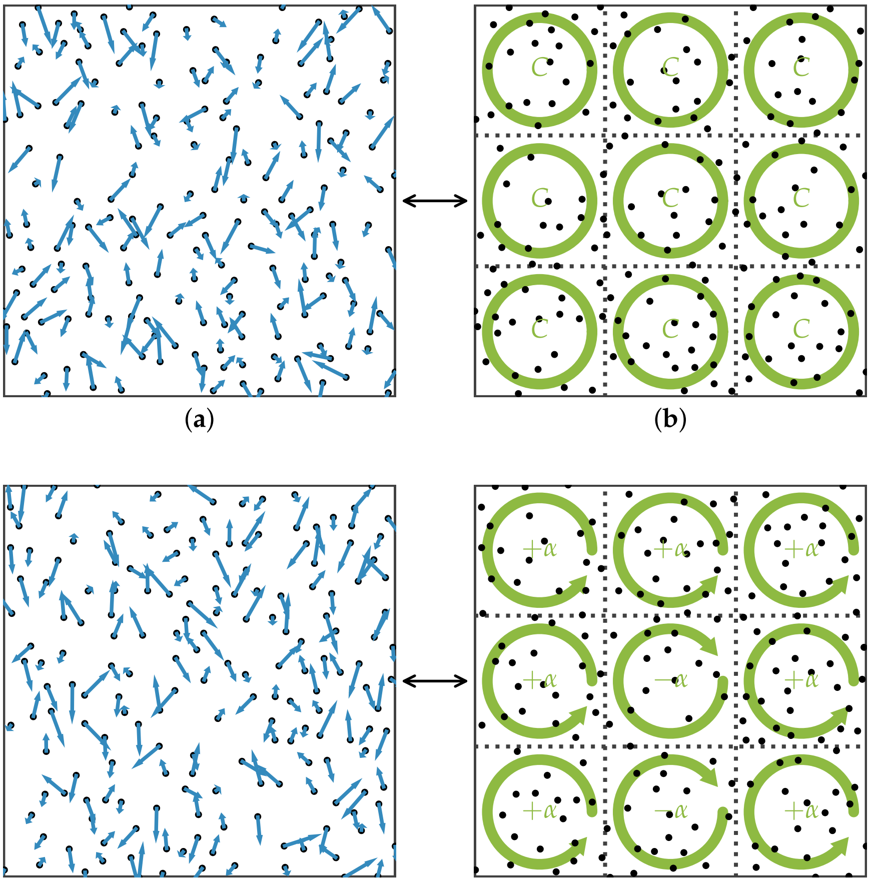

(**a**) (**b**)

(**c**) (**d**)

Figure 3.1: The standard MPCD algorithm includes two steps. (**a**) In the free streaming step the particles move ballistically. (**b**) In the collision step the fluctuating part of their velocities is generated randomly from a Boltzmann distribution. The SRD variant of MPCD has the same streaming step (**c**), but in the collision step a stochastic rotation is applied to the fluctuating velocity components (**d**). In both cases, the collision step is surrounded by a coordinate shift and its inverse.

for every cell α is required. Defining

$$\mathbf{r}_i^\alpha \equiv \mathbf{r}_i - \mathbf{r}^\alpha, \tag{3.8}$$

we can compute the angular momentum of cell α before the collision step

$$\mathbf{L}^\alpha_{\text{Before}} = m \sum_{i \in \text{cell}} \mathbf{r}_i^\alpha \times (\mathbf{v}_i - \mathbf{v}_C) = m \sum_{i \in \text{cell}} \mathbf{r}_i^\alpha \times \mathbf{v}_i, \tag{3.9}$$

and after the collision step

$$\mathbf{L}^\alpha_{\text{After}} = m \sum_{i \in \text{cell}} \mathbf{r}_i^\alpha \times (\mathbf{v}_i^{\text{ran}} + \mathbf{v}_C) = m \sum_{i \in \text{cell}} \mathbf{r}_i^\alpha \times \mathbf{v}_i^{\text{ran}}. \tag{3.10}$$

The difference in angular momentum, that needs to be compensated is therefore

$$\Delta \mathbf{L}^{\alpha} = \mathbf{L}^{\alpha}_{\text{After}} - \mathbf{L}^{\alpha}_{\text{Before}} = m \sum_{i \in \text{cell}} \mathbf{r}_i^{\alpha} \times (\mathbf{v}_i^{\text{ran}} - \mathbf{v}_i). \tag{3.11}$$

We may revert it by applying an angular velocity $\mathbf{\Omega}^{\alpha}$, satisfying

$$\begin{aligned} \boldsymbol{t}\mathbf{\Omega}^{\alpha} &= -\Delta \mathbf{L}^{\alpha} \\ \Leftrightarrow \mathbf{\Omega}^{\alpha} &= -\boldsymbol{t}^{-1} \Delta \mathbf{L}^{\alpha} \end{aligned} \tag{3.12}$$

with moment of inertia tensor $\boldsymbol{t} \equiv \boldsymbol{t}(\alpha)$. For the MPCD algorithm with angular momentum conservation, called MPCD+a, this implies the collision rule [76]

$$\mathbf{v}_i(t + \Delta t) = \mathbf{v}^{\alpha}(t) + \mathbf{v}_i^{\text{ran}} - \frac{1}{N_C} \sum_{j \in \text{cell}} \mathbf{v}_j^{\text{ran}} + \mathbf{\Omega}^{\alpha} \times \mathbf{r}_i. \tag{3.13}$$

For SRD+a we have [77]

$$\mathbf{v}_i(t + \Delta t) = \mathbf{v}^{\alpha}(t) + \boldsymbol{R}^{\alpha}[\mathbf{v}_i(t) - \mathbf{v}^{\alpha}(t)] + \mathbf{\Omega}^{\alpha} \times \mathbf{r}_i. \tag{3.14}$$

3.3 Nematic Adaptation

We incorporate nematodynamics into MPCD by giving every particle extra properties that describe the medium's nematic characteristics. Using the Beris-Edwards model described in section 2.7.4, it is most convenient to directly equip every particle with its own order parameter $\boldsymbol{Q}_i$. We introduce new 'nematic' step to the scheme, in which we work out the nematodynamics of the system.

3.3.1 Initialization

Our algorithm is capable of dealing with boundaries of arbitrary shape. The spatial derivatives appearing in the free energy make the values of the order parameter outside of the LC's domain important, and the free energy gains additional terms close to the boundary. Therefore, we start the initialization process by establishing the computation area. Here, all of the cells are classified. Most of them are completely contained within the LC and are classified as normal. Cells that are intersected by a domain boundary we call 'border' cells. They contain normal and ghost particles. The free energy of these cells includes boundary terms, leading to an anchoring of the director. Cells, that are outside the domain, but tangential to the boundary are classified as ghost cells. They contain only ghost particles and are anchored in the same way as border cells. Since they are not a part of the LC, they don't couple to the flow, directly. If any cells are left, they are classified as 'outside'. They are less significant and their local order parameter $\boldsymbol{Q}$ is kept constant. Figure 3.2 gives a schematic representation of the computational grid.

Afterwards N particles are positioned randomly within every cell. Similarly to the computational grid particles positioned outside of the domain are assigned

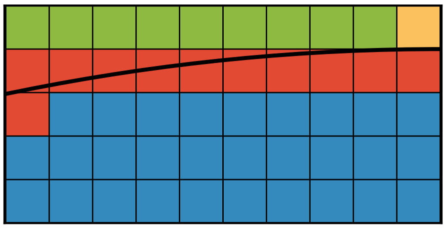

Figure 3.2: The computational grid is determined by the shape of the boundary (black line) and includes normal cells (blue), border cells (red), ghost cells (yellow), and outside cells (green).

'ghost' status. This discrimination is based on the exact shape of the bounding surface, not on the cell type. However, ghost particles in 'outside' cells only play a role in the collision step, where they exchange (angular) momentum with other particles. The rest of the ghost particles also interact via their order parameters $\boldsymbol{Q}_i$.

Next, the ordinary particle velocities are initialized according to a Boltzmann distribution. All velocity components are drawn from a standard normal distribution, since we choose $E_{kT} = 1$. Then, the center of mass drift of the system is subtracted and a rescaling is applied, to make sure there is unit variance across all velocity components. Ghost particle velocities, on the other hand, are initialized at zero.

If there are non-periodic boundaries, now S_0 and $\mathbf{n}_0(\mathbf{r})$ are calculated, which are needed for the anchoring of the order parameter $\boldsymbol{Q}$ (see eqs. (2.54) and (2.55)). For S_0 we use the analytical value for the equilibrium-scalar-order-parameter in uniaxial NLCs [eq. (2.82)]

$$S_0 = \frac{b}{6c} + \frac{1}{2}\sqrt{\left(\frac{b}{3c}\right)^2 - \frac{8a}{3c}}. \tag{3.15}$$

The direction of anchoring is calculated at all ghost- and border-cells. Using the unit surface normal $\hat{\mathbf{A}}$ and the geometric center $\mathbf{c}^\alpha$ of cell α, the vector can be expressed as

$$\mathbf{n}_0^\alpha = \boldsymbol{R}\hat{\mathbf{A}}(\mathbf{c}^\alpha) \tag{3.16}$$

with a constant rotation matrix $\boldsymbol{R}$, that depends on the type of boundary condition. For homeotropic boundary conditions $\boldsymbol{R} = 1$, for homogeneous boundary conditions $\boldsymbol{R}$ needs to rotate by an angle $\pi/2$ and has a degree of freedom. Any other rotation matrices are also permissible and correspond to anchoring with a specific angle to the surface.

3.3.2 Algorithm

After the initialization, we loop through the time steps. At the start of every step, we set all ghost particle positions to zero and randomize their positions. This randomization process keeps them within the same cell, and outside of the domain.

Then, the particle positions are shifted randomly. This is equivalent to a shift of the coordinate system. Before the particles are shifted back, the collision step is performed. It requires no adaptation to LCs. In this step, ghost particles are treated in the same way as ordinary particles, leading to a change in their velocities.

After the second shift, a stage new to the MPCD-algorithm is executed. We will call this the nematic step. In the nematic step we want to calculate the internal force, that arises due to the nematic properties of the medium, and we want to evolve the order parameter $\boldsymbol{Q}$ in time. Since the Beris-Edwards theory is a macroscopic model, we need to apply it to macroscopic quantities. Therefore, we discretize the system in the same way as in the collision step. Cell averages yield the macroscopic order parameter

$$\boldsymbol{Q}^{\alpha} = \frac{1}{N_{\alpha}} \sum_{j \in \text{cell}} \boldsymbol{Q}_j, \tag{3.17}$$

and velocity (see eq. (3.2)) for every cell α. Calculating the gradients of the order parameter $Q^{\alpha}_{ij,k}$ and of the velocity $v^{\alpha}_{i,j} \leftrightarrow (D^{\alpha}_{ij}, \omega^{\alpha}_{ij})$ across the grid allows us to construct elastic and advective terms. All spatial derivatives are performed symmetrically, if the boundary conditions allow. Otherwise we use the second order one-sided finite-difference [78], for example

$$\frac{\mathrm{d}}{\mathrm{d}x}\mathbf{v}(x,y,z) = \mp \frac{3\mathbf{v}(x,y,z) - 4\mathbf{v}(x \pm \Delta x, y, z) + \mathbf{v}(x \pm 2\Delta x, y, z)}{2\Delta x} + \mathcal{O}\left(\Delta x^2\right). \tag{3.18}$$

The upper sign is used, if the simulation domain ends at (x, y, z), facing a boundary in negative x-direction. The lower sign is used, if a boundary is encountered in the positive x-direction.

If we consider the hydrostatic pressure in eq. (2.147), we see a hydrodynamic component ρT and a nematic component $-\frac{L}{2}Q^2_{ij,k}$. The former is implicitly present in the MPCD algorithm. The latter can be calculated on an individual cell level as

$$P^{\alpha}_0 = -\frac{L}{2} Q^{\alpha}_{ij,k} Q^{\alpha}_{ij,k}. \tag{3.19}$$

The system should minimize the free energy in eq. (2.138) with no external field $\Psi_{\text{ext}} = 0$. Employing the one-constant approximation [see eq. (2.140)] we obtain the molecular field for each cell as

$$H^{\alpha}_{ij} = -aQ^{\alpha}_{ij} + b\left[Q^{\alpha}_{ik}Q^{\alpha}_{kj} - \delta_{ij}\frac{1}{3}Q^{\alpha}_{kl}Q^{\alpha}_{kl}\right] - cQ^{\alpha}_{ij}Q^{\alpha}_{kl}Q^{\alpha}_{kl} + L\nabla^2 Q^{\alpha}_{ij}, \tag{3.20}$$

where we used the symmetry of Q^{α}_{ij}. Eqs. (3.17), (3.19), and (3.20) allow us to calculate the stress tensor within each cell according to eqs. (2.144) and (2.165)

$$\begin{aligned}\sigma^{\alpha}_{ij} = &-P^{\alpha}_0\delta_{ij} - \xi H^{\alpha}_{ik}(Q^{\alpha}_{kj} + \delta_{kj}/3) - \xi(Q^{\alpha}_{ik} + \delta_{ik}/3)H^{\alpha}_{kj} \\ &+ 2\xi(Q^{\alpha}_{ij} + \delta_{ij}/3)Q^{\alpha}_{kl}H^{\alpha}_{kl} - LQ^{\alpha}_{kl,i}Q^{\alpha}_{kl,j} + Q^{\alpha}_{ik}H^{\alpha}_{kj} - H^{\alpha}_{ik}Q^{\alpha}_{kj} - \Lambda Q_{ij}.\end{aligned} \tag{3.21}$$

Here, we used the one-constant approximation, again, in which the distortion free energy density F_d is given by eq. (2.50), so that

$$\frac{\delta F}{\delta Q_{kl,i}} = L Q_{kl,i}.$$

The stress tensor field defines a force, that we can apply in the streaming step. In eq. (2.84) we see a hydrodynamic term and a nematic term. The former is, again, implicit in the MPCD algorithm. The latter yields said force

$$\rho^\alpha \frac{\mathrm{d}}{\mathrm{d}t}\mathbf{v}^\alpha = \boldsymbol{\nabla} \cdot \boldsymbol{\sigma}^\alpha. \tag{3.22}$$

Keeping in mind, that $\mathbf{v}^\alpha$ is composed of individual particle motion, we take the time derivative of eq. (3.2) and multiply by N_α. This yields

$$\frac{\rho^\alpha}{\rho_0}\frac{\mathrm{d}}{\mathrm{d}t}\mathbf{v}^\alpha = \sum_{j\in\mathrm{cell}} \frac{\mathrm{d}}{\mathrm{d}t}\mathbf{v}_j, \tag{3.23}$$

with a scaling parameter

$$\rho_0 \equiv \frac{\rho^\alpha}{N_\alpha} = \frac{\rho}{N}. \tag{3.24}$$

It is a material constant and independent of α, because the MPCD-particles represent fluid elements and their number density is proportional to the fluid's local density. Since we chose the cell as the smallest unit of discretization for the force, we have $\frac{\mathrm{d}}{\mathrm{d}t}\mathbf{v}_j = \frac{\mathrm{d}}{\mathrm{d}t}\mathbf{v}_i \ \forall j, i \in$ cell. This simplifies eq. (3.23) to

$$\frac{\rho^\alpha}{\rho_0}\frac{\mathrm{d}}{\mathrm{d}t}\mathbf{v}^\alpha = N_\alpha \frac{\mathrm{d}}{\mathrm{d}t}\mathbf{v}_j \qquad \forall j \in \text{cell}. \tag{3.25}$$

Taking into account eq. (3.22), we see that the acceleration of an individual particle within the cell α is

$$\mathbf{a}^\alpha \equiv \frac{\mathrm{d}}{\mathrm{d}t}\mathbf{v}_j = \frac{1}{\rho_0 N_\alpha}\boldsymbol{\nabla} \cdot \boldsymbol{\sigma}^\alpha. \tag{3.26}$$

It is applied in the streaming step. In the nematic step, with the knowledge of D^α and ω^α, we can calculate the generalized advection term for every cell from eq. (2.142)

$$\begin{aligned} S^\alpha_{ij} = (\xi D^\alpha_{ik} + \omega^\alpha_{ik})(Q^\alpha_{kj} + \delta_{kj}/3) + (Q^\alpha_{ik} + \delta_{ik}/3)(\xi D^\alpha_{kj} - \omega^\alpha_{kj}) \\ - 2\xi (Q^\alpha_{ij} + \delta_{ij}/3) Q^\alpha_{kl} D^\alpha_{lk}, \end{aligned} \tag{3.27}$$

where we substituted $Q_{kl}D_{lk}$ for $Q_{kl}v_{l,k}$, since their difference $Q_{kl}\omega_{lk}$ vanishes due to symmetries. We can now integrate the order parameter according to eq. (2.141)

$$\boldsymbol{Q}^\alpha_i(t + \Delta t) = \boldsymbol{Q}^\alpha_i(t) + \Delta \boldsymbol{Q}(t)\Delta t. \tag{3.28}$$

For the three types of cells inside the medium we have

$$\begin{cases} \Delta \boldsymbol{Q}(t) = \Gamma \boldsymbol{H}^{\alpha}(t) + \boldsymbol{S}^{\alpha}(t), & \text{if } \alpha \in \text{ normal}, \\ \Delta \boldsymbol{Q}(t) = \Gamma \boldsymbol{H}^{\alpha}(t) + \boldsymbol{S}^{\alpha}(t) + W_A(\boldsymbol{Q} - \boldsymbol{Q}_0), & \text{if } \alpha \in \text{ border}, \\ \Delta \boldsymbol{Q}(t) = \Gamma \boldsymbol{H}^{\alpha}(t) + W_A(\boldsymbol{Q} - \boldsymbol{Q}_0), & \text{if } \alpha \in \text{ ghost}, \end{cases} \tag{3.29}$$

where we took into account the additional free energy close to boundaries from eq. (2.54). Additionally, $\boldsymbol{Q}_i$ must be ensured to remain numerically traceless at every time step. We enforce this by substituting $\Delta\boldsymbol{Q}$ with $\Delta\boldsymbol{Q} - \boldsymbol{I}\,\mathrm{Tr}(\Delta\boldsymbol{Q})/3$ in each cell. Even though the underlying equation for the time evolution of $\boldsymbol{Q}$ gives the material derivative $\mathrm{d}\boldsymbol{Q}/\mathrm{d}t$, it can be integrated without being expanded, since we apply the incremental changes to the particles i, which are advected, and not to the cells α. Still, every particle i within a cell α experiences the same change in order parameter.

The time step concludes with the streaming step. Here, position and velocity are integrated. For every particle i in cell α we set

$$\mathbf{r}_i(t + \Delta t) = \mathbf{r}_i(t) + \mathbf{v}_i(t)\Delta t + \frac{1}{2}\mathbf{a}^{\alpha}(t)\Delta t^2, \tag{3.30}$$

$$\mathbf{v}_i(t + \Delta t) = \mathbf{v}_i(t) + \mathbf{a}^{\alpha}(t)\Delta t, \tag{3.31}$$

with acceleration $\mathbf{a}^{\alpha}(t)$ from the nematic step. If periodic boundaries are encountered by a particle, its position is shifted, without affecting the modulus with respect to the corresponding dimension L_k. If non-periodic boundaries are encountered, the bounce-back condition is applied. That is, the particle is propagated until it collides with the surface, then its velocity is reversed, and it is propagated for the remainder of the time step. If an energy concentration c is used, the streaming step ends with the integration of c [see eq. (2.164)]

$$c(t + \Delta t) = c(t) + \partial_i \Big[\mathcal{D}_{ij} c_{,j}(t) + \Lambda' c(t)^2 Q_{ij,j}(t) \Big] \Delta t. \tag{3.32}$$

3.3.3 Dimensionless Parameters

The algorithm presented here has many dimensionless parameters. Principally, there are the three lengths of the cuboid that encloses the system $L_x + G_x$, $L_y + G_y$, and $L_z + G_z$, the number of MPCD-particles per cell $N \equiv \langle N^{\alpha} \rangle$, the length of a time step Δt, and total simulation time $M\Delta t$. The cuboid lengths are divided into the maximal length of the nematic fluid L_i and the length of the remaining ghost cells in the respective dimension i.

The nematodynamics, further, depend on the elastic constant L, the activity parameter Λ, the tumbling constant ξ, and on the collective rotational diffusion constant Γ. There is another set of parameters governing the boundary conditions, namely the shape of the boundary, the anchoring coefficient W_0, and the rotation matrix $\boldsymbol{R}$ used for calculating the anchoring director $\mathbf{n}_0^{\alpha}$ for every cell α. Table 1 gives an overview of the parameters.

parameter	symbol
system dimensions	L_x, L_y, L_z
number of MPCD-particles per cell	N
time step	Δt
Laundau-de Gennes coefficients	a, b, c
collective rotational diffusion constant	Γ
elastic constant	L
anchoring strength	W_A
tumbling parameter	ξ
activity parameter	Λ

Table 1: Primary input parameters for our algorithm.

Within the simulations we fix the dimensionality at $N_D = 3$, the lengths of every cell d_s, as well as the thermal energy E_{kT}, and the mass of every particle m_s at 1. The allows us to relate the dimensionless parameters from the previous paragraph to reality, choosing three reference values: a length d_0, a time τ_0, and a mass m_0. The elastic constant has a unit of force and can be expressed as

$$L = \frac{L^*}{L_0} = L^* \frac{\tau_0^2}{d_0 m_0}. \tag{3.33}$$

We mark dimensional values, such as L^*, with an asterisk and construct the reference quantities (in this case L_0) from d_0, τ_0, and m_0. The collective rotational diffusion constant has units of inverse dynamic viscosity and can be non-dimensionalized as

$$\Gamma = \frac{\Gamma^*}{\Gamma_0} = \Gamma^* \frac{m_0}{d_0 \tau_0}. \tag{3.34}$$

The same holds for the anchoring strength

$$W_A = \frac{W_A^*}{\Gamma_0} = W_A^* \frac{m_0}{d_0 \tau_0}. \tag{3.35}$$

The dimensional coefficients in the Laundau-de Gennes free energy a^*, b^*, and c^*, as well as the activity Λ have units of pressure. By way of example we will consider

$$b = \frac{b^*}{b_0} = b^* \frac{L^* d_0}{k_\mathrm{B} T} = b^* \frac{L^* \tau_0^2}{d_0 m_0}. \tag{3.36}$$

For the time step we simply have

$$\Delta t = \frac{\Delta t^*}{\tau_0}. \tag{3.37}$$

In this thesis, we restrict ourselves to $\xi = 1$, $\Delta t = 0.01$, $N = 60$. As basic reference quantities we choose $d_0 = 1 \times 10^{-5}\,\mathrm{m}$, and $\tau_0 = 1 \times 10^{-2}\,\mathrm{s}$. Since, in MPCD, the viscosity of the fluid depends on the time step Δt, we can calculate a reference mass

$$m_0 = \alpha_4 \frac{\tau_0 d_0}{4\eta_s} \approx 6.67 \times 10^{-12}\,\mathrm{kg}, \tag{3.38}$$

with a Leslie viscosity of $\alpha_4 = 0.0652\,\mathrm{Pa\,s}$. The dimensionless shear viscosity in MPCD is given by a kinetic and a collisional contribution $\eta_s = N(\nu_k + \nu_c) \approx 4.07$ with [79,80]

$$\nu_k = \frac{E_{kT}\Delta t}{m_s}\left(\frac{N}{N - (N_D + 2)/4} - \frac{1}{2}\right), \tag{3.39}$$

$$\nu_c = \frac{d_s^2}{24\Delta t}\frac{N - 7/5}{N}. \tag{3.40}$$

Unless stated otherwise, we use the dimensional parameters $L^* = 40\,\mathrm{pN}$, $\Gamma^* = 730/(\mathrm{Pa\,s})$, $W_A^* = 1000/(\mathrm{Pa\,s})$, and $(a^*, b^*, c^*) = (-0.08\,\mathrm{Pa}, 0.92\,\mathrm{Pa}, 0.76\,\mathrm{Pa})$. The resulting dimensionless parameters are given in table 2.

a	b	c	Γ	L	W_A
−20	230	190	0.05	100	12000

Table 2: Values of the dimensionless input parameters for most simulations.

Chapter 4

Results

Our modified MPCD algorithm is capable of modeling NLCs in the presence of complex boundary conditions on mesoscopic length scales. In this chapter we will first confirm the validity of the simulations, and go on to investigate the behavior of NLCs in cylindrical confinement, a setup with experimental relevance [70].

Although we implemented and tested the algorithm to a high degree of generality, here we naturally restrict ourselves to a narrow set of configurations. To this end, all of the following simulations were done with the angular momentum conserving MPCD collision step, and not the SRD variant. Energy sources are assumed to be abundant, driving the molecules as expressed in eq. (2.165)

$$\boldsymbol{\sigma}^{\mathrm{a}} = -\Lambda \boldsymbol{Q},$$

and requiring no concentration field [cf. eq. (2.163)]. Excluding the verification, the simulations all use the dimensionless parameters given in section 3.3.3. In particular, the second activity parameter λ is fixed at 0. This leaves the system dimensions L_x, L_y, L_z, the activity Λ and the boundary conditions as variables.

4.1 Verification

We start with a passive, uniform, unconstrained NLC and verify its basic hydrodynamic behavior in the presence of a pressure gradient. Then, we examine how the transition between the isotropic and the nematic phase takes place and test how well the dynamics of defects are reproduced in our simulations. The verification concludes with a look at the impact of an active stress on nematodynamics.

4.1.1 Poiseuille Flow

Before studying nematodynamics, it is useful to check the validity of the hydrodynamics produced by our algorithm. If we apply a constant pressure gradient to a system bounded by parallel walls with homogeneous anchoring, we expect a

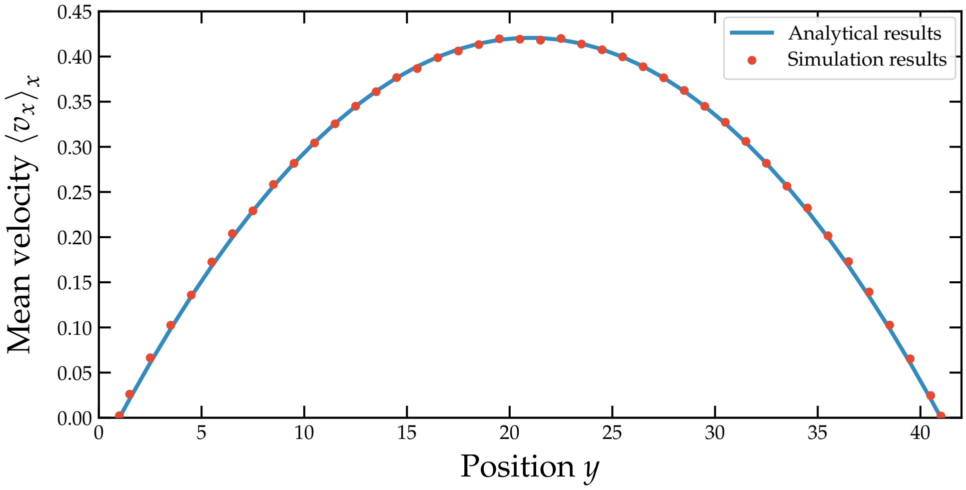

Figure 4.1: Flow profile at constant pressure gradient in x-direction. The simulations were done with walls of thickness $y_0 = 1$ parallel to the xz-plane, $L_x = 15$, $L_y = 40$, $L_z = 4$, $P_{,x} = 0.5$, $\Delta t = 0.01$, $\Gamma = 0.05$, $L = 100$, and $S_{\text{eq}} = 0.633$

Poiseuille flow to form, which has a parabolic profile

$$v(y) = \frac{1}{4\mu} P_{,x} \left[\left(\frac{L_y}{2} \right)^2 - \left(y - y_0 - \frac{L_y}{2} \right)^2 \right], \tag{4.1}$$

with dynamic viscosity μ. In our simulations the director field evolves to be completely homogeneous, fully aligned with the x-axis. Figure 4.1 shows the simulation results and the theoretical profile for the velocity. They match up very well and allow us to calculate the dimensionless viscosity $\mu = 118.8$ for this parameter configuration. The computational grid used for these simulations is given in figure A.1 of the appendix.

4.1.2 Isotropic-Nematic Phase Transition

To explore the isotropic-nematic phase transition, we consider the idealization of an unconstrained NLC on an infinite domain. A common parametrization $a = (1 - \gamma/3)$, $b = c = \gamma$ [58, 81, 82] for the study of the transition makes use of Doi's excluded volume parameter $\gamma = \rho_D q_D \nu_2 / \alpha_D$ [83–85]. Here, ρ_D is the concentration, q_D the molecular aspect ratio, and α_D and ν_2 are geometrical constants. An unconstrained NLC will evolve towards a uniaxial state. We have shown in section 2.6, that, in this case, the Landau-de Gennes free energy reduces to [eq. 2.81]

$$F_{\text{B}} = \frac{3}{4} a S^2 - \frac{1}{4} b S^3 + \frac{9}{16} c S^4,$$

with temperature-dependent parameter $a = A(T - T^*)$. It is minimized for the equilibrium order parameter S_{eq} according to eq. (2.82). Rewriting it in terms of γ

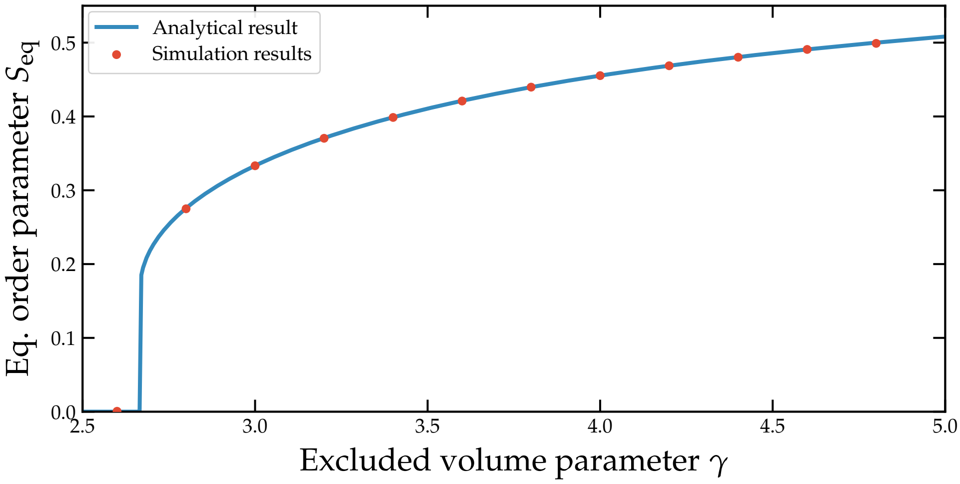

Figure 4.2: Isotropic nematic phase transition. Initialized isotropically. The simulations were done with $\gamma = 1.5$, $\Delta t = 0.01$, $\Gamma = 0.1$, and $L = 100$.

yields

$$S_{\mathrm{eq}}(\gamma) = \begin{cases} \frac{1}{6} + \frac{1}{2}\sqrt{1 - \frac{8}{3\gamma}} & \text{if } \gamma \geq 8/3, \\ 0 & \text{if } \gamma < 8/3. \end{cases} \tag{4.2}$$

The numerical analogue to the infinite, unconstrained NLC is a LC with periodic boundary conditions. Initializing the system isotropically, and evolving it for 3×10^4 time steps, we obtain the equilibrium order parameter values S_{eq} for different γ. The results are plotted in figure 4.2. They match up very well with both the analytics, and the results of different numerical methods, i.e. Denniston *et al.* [81]. As expected in 3D, we find a first-order phase transition from the isotropic to nematic phase. For $S_{\mathrm{eq}}(\gamma) > 0$ the simulations take at most 2×10^4 time steps to equilibrate. Figure 4.3 shows the process in some detail. Order forms slowly and the LC finds a locally favorable biaxial configuration. Then, the biaxiality decreases to zero, as the scalar order parameter reaches a value close to equilibrium at t_{eq}. Afterwards, S_{eq} is approached asymptotically. The system chooses its director freely, as there is no imposition from outside. The final direction is already established by about $t_{\mathrm{eq}}/3$, much earlier than S_{eq}. The figure also demonstrates that nematically initialized systems take about an order of magnitude less time to equilibrate. Of course, this depends on the details of the initialization. Once established, the director is constant. Even as the order changes for the nematically initialized system, there is no change to the director. For $S_{\mathrm{eq}}(\gamma) = 0$ the simulations take much less time to equilibrate (fig. 4.4). Even initialized at complete order, the system is very close to its asymptotic state by about 1×10^4 time steps. The biaxiality is always zero.

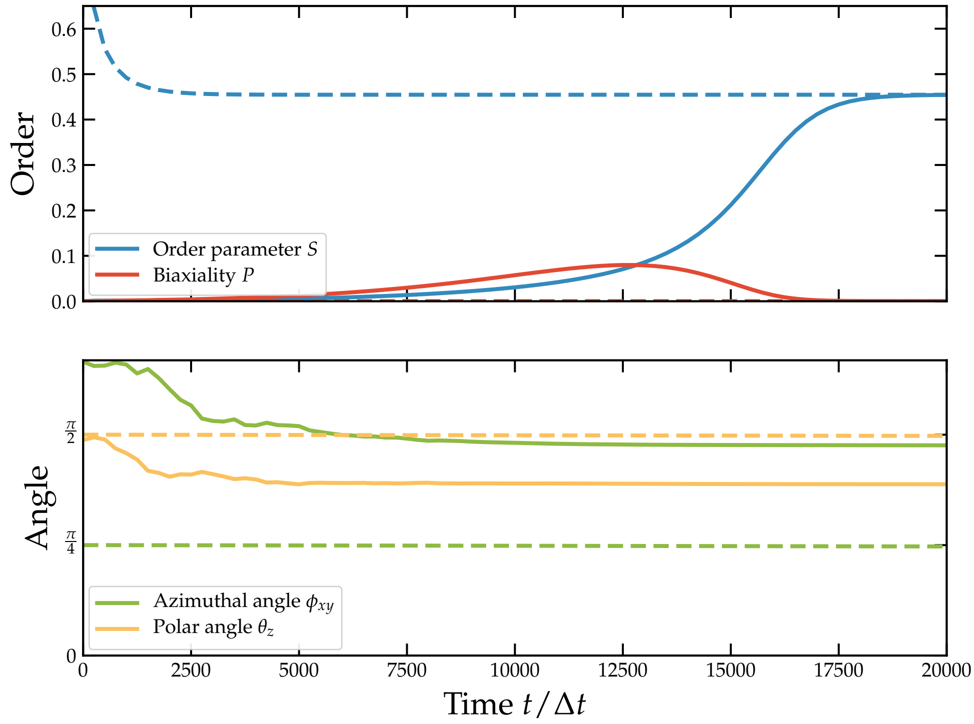

Figure 4.3: Transition to equilibrium from the isotropic state (continuous lines) and from the nematic state $S(t = 0) = 0.8$ (dotted lines). The simulations were done with parameters $\gamma = 4.0$, $\Delta t = 0.01$, $\Gamma = 0.1$, $L = 100$, and $S_{\text{eq}}(\gamma) = 0.455$.

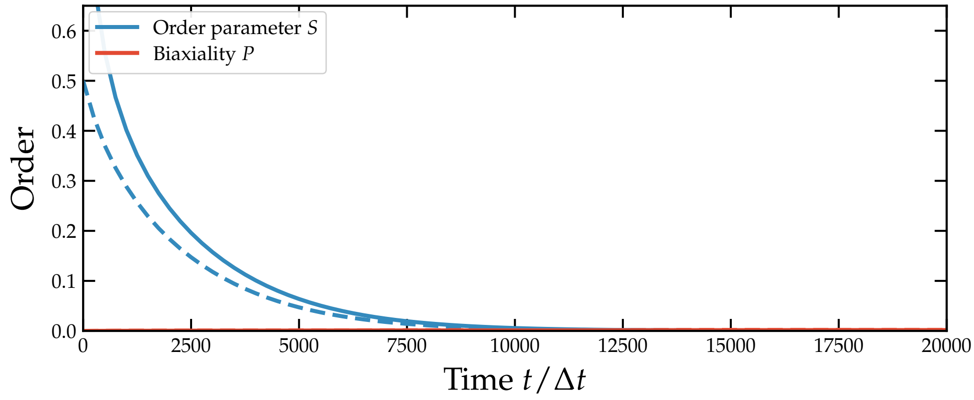

Figure 4.4: Transition to (isotropic) equilibrium from the nematic state $S(t = 0) = 1$ (continuous lines) and from the nematic state $S(t = 0) = 0.5$ (dotted lines). The simulations were done with parameters $\gamma = 1.5$, $\Delta t = 0.01$, $\Gamma = 0.1$, $L = 100$, and $S_{\text{eq}}(\gamma) = 0$.

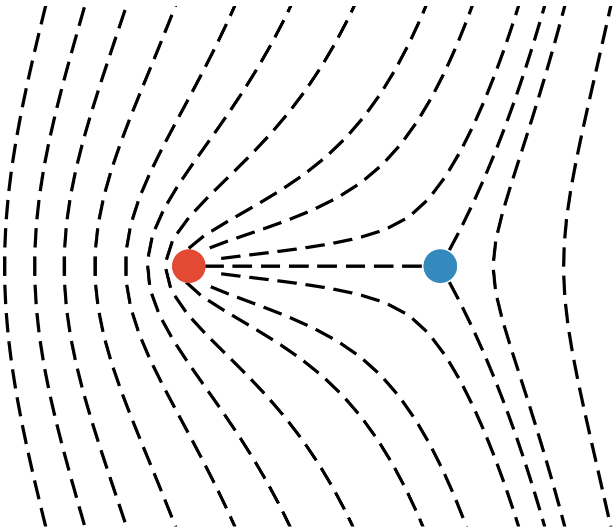

Figure 4.5: Schematic of the director field in our simulations of defect annihilation. The $+1/2$ defect (red) and the $-1/2$ defect (blue) are attracted and converge, until they collide. The resulting director field is singularity-free.

4.1.3 Defect annihilation

By studying how defects annihilate in our simulations, we can verify that a more complex and stringent prediction of nematodynamics is reproduced. We prepare a relatively clean form of this process, by initializing a $+1/2$ and a $-1/2$ disclination line parallel to the z-axis. They are separated by a distance of $s(t=0)=64$ cells along the x-axis, in a domain with periodic boundary conditions. Alternatively, walls could be used in the x- and y-directions, if the anchoring is weak. The simulation domain has dimensions $L_x=160$, $L_y=90$, and $L_z=4$, ensuring minimal interference from the boundaries. Figure 4.5 gives a schematic representation of the setup. As discussed in section 2.5, we expect the distance between the disclination lines to shrink approximately as $s(t)=d_0\sqrt{t_0-t}$ [eq. (2.62)]. Figure 4.6 shows the separation over time in our simulations. In spite of the coarse computational grid, the algorithm is able to resolve the process very well. The data matches eq. (2.62) closely, as can be seen from the fit.

4.1.4 Activity

We model microscopic activity as an additional contribution to the stress tensor [see eq. (2.165)]. Its magnitude is controlled by the parameter Λ, but qualitatively it only produces two kinds of forces. As discussed in section 2.8, values $\Lambda>0$ correspond to extensile stress, while $\Lambda<0$ corresponds to contractile stress. The model applies exclusively to nematic systems and the force is proportional to the divergence of the order parameter $\boldsymbol{Q}$. Therefore, we only need to consider defects to see its effect. As long as the external constraints are not too dominant, NLCs close to their steady state only contain charge $\pm1/2$ disclination lines (see section 2.5). We initialized a low-temperature active system with periodic boundary

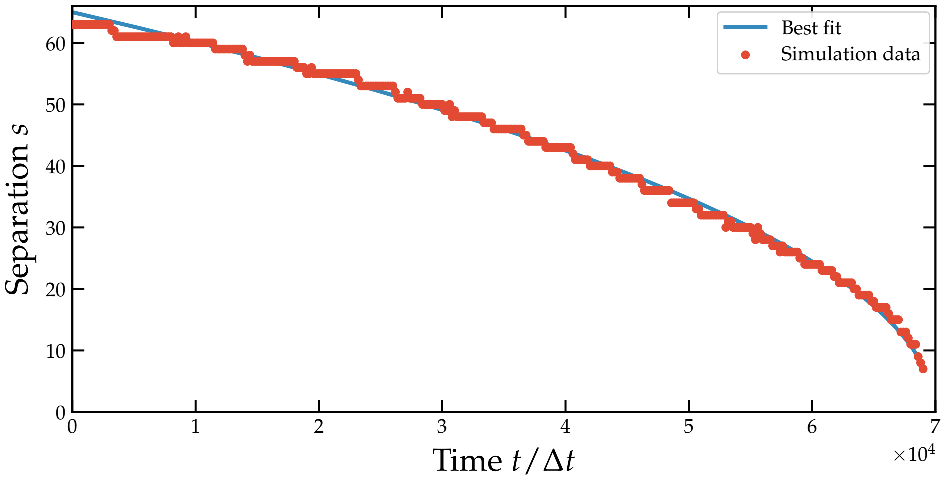

Figure 4.6: The blue line gives the measured distance between a +1/2 and a -1/2 defect over time. The red line gives the best fit $s(t) = d_0\sqrt{t_0 - t}$ with fit parameters $d_0 = 0.245$ and $t_0 = 69910$. The defects annihilate after $t_0 \approx 7 \times 10^4$ time steps. The parameters used were $L_x = 160$, $L_y = 90$, $L_z = 4$, and $N = 50$.

conditions along all axes and small thickness $L_z = 4$ in the isotropic state. It underwent the Kibble mechanism (see section 2.5) and entered the nematic phase with a number of defects. Figure 4.7 shows how they are affected by the extensile active stress. Forces from a contractile stress would act in the exact opposite direction. Clearly, both kinds of defects produce flow fields in their surrounding volumes. However, only the $+1/2$ defect experiences a net force in isolation. This matches up with experiments [1]. In the following section we will see that, in confinement, the elastic force often counteracts the active one. Additionally, the hydrodynamic force and higher order interactions between the order parameter field and the flow field need to be taken into account. The mental picture suggested by figure 4.7 **(a)** is, therefore, very simplified.

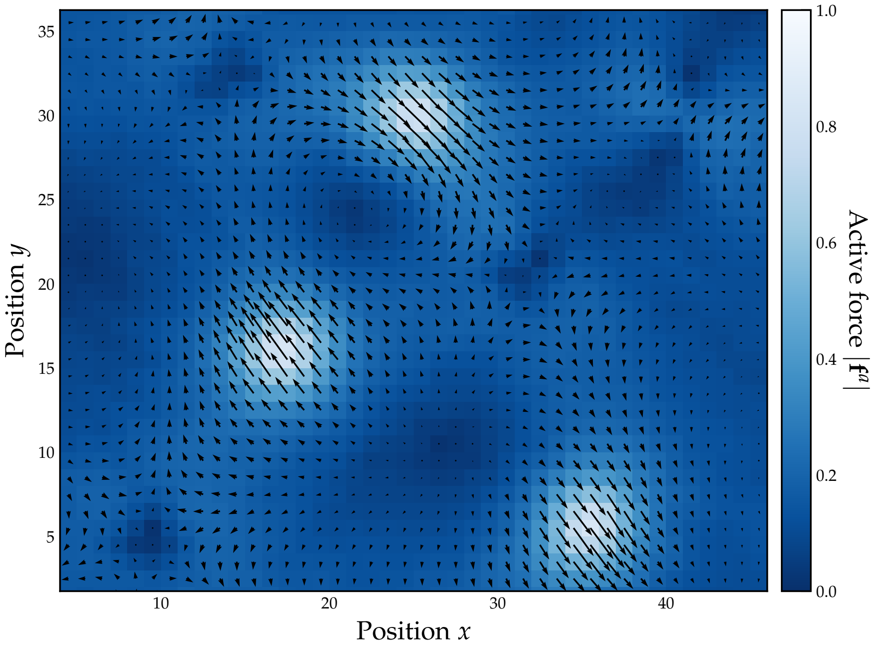

(a) The black arrows give x- and y-components of the force $\mathbf{f}^{\mathrm{a}}$ produced by an extensile active stress with $\Lambda = 0.1$. The color code gives the total magnitude.

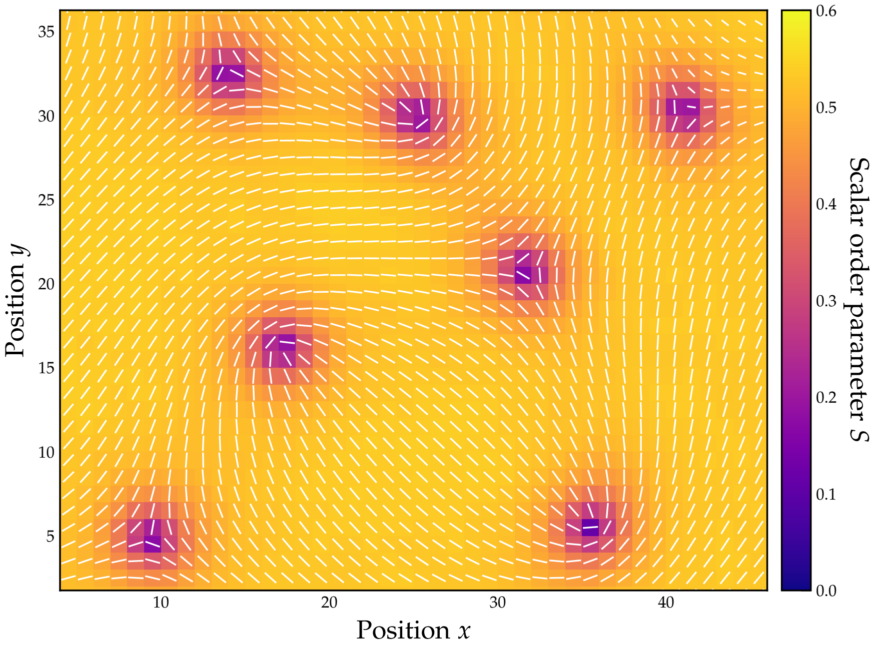

(b) The corresponding order parameter field is represented by the local director $\mathbf{n}$ (white lines) and the scalar order parameter S (color code).

Figure 4.7: In our simulations of active quasi-2D-systems, defects produce force fields, that decay strongly with distance. The positively charged $+1/2$ defects experience a large, directed force, while the forces acting on $-1/2$ defects cancel out. The colored pixels represent the discretized cells. However, in the collision step, they are randomly shifted.

4.2 Active Nematics Inside a Cylindrical Channel

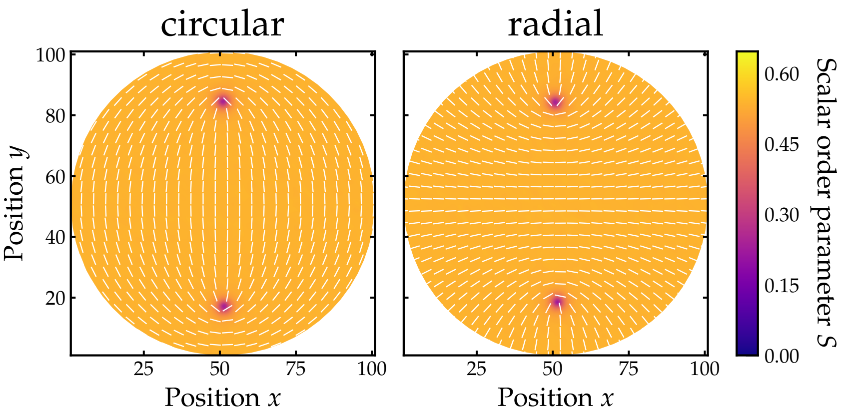

Figure 4.8: Equilibrium order parameter fields (activity $\Lambda = 0$) in our simulations of a cylindrical channel. The director (white lines) and the scalar order parameter (background color) are given for circular and radial anchoring.

The behavior of active NLCs is heavily influenced by their boundary conditions. In this respect, the topological constraints are especially relevant, since they determine the defect configuration. As we saw in the previous section, defects are the force poles of nematic activity. We study the effects of boundary conditions on active NLCs in a 3-dimensional channel. The focus is on a cylindrical channel with circular cross-section, but we also investigate one with elliptical cross-section.

4.2.1 Circular Cross-Section

The channel has a radius of $R_c = 50$. We accommodate it within a simulation domain of $L_x = 102$, $L_y = 102$, that leaves room for ghost cells which represent the walls. Boundary conditions along the capillary z-axis are periodic, to approximate an infinite length. The actual length is fixed at $L_z = 4$. This is computationally economical, but leaves enough cells for the calculation of meaningful finite differences [70]. The computational grid (see section 3.3) is displayed in figure A.2 of the appendix. The MPCD-particles are subject to no-slip boundary conditions on the channel's wall.

We investigate four different anchoring conditions for this geometric setup. Across a wide range of activities $\Lambda \in [-0.135, 0.135]$ we simulate systems with constant Λ for 250 000 time steps and apply either (i) homeotropic anchoring, which we call 'radial', (ii) tangential (homogeneous) anchoring in the polar plane, which we call 'circular', (iii) tangential (homogeneous) anchoring parallel to the cylinder axis, called 'axial', and (iv) 45° anchoring within the polar plane, called 'tilted'. In a 3-dimensional system, these would accommodate an aster (i), a vortex (ii), or a spiral (iv), perfectly (see section 2.5). Every one of the constraints has topological implications for the system. In equilibrium, the axial configuration

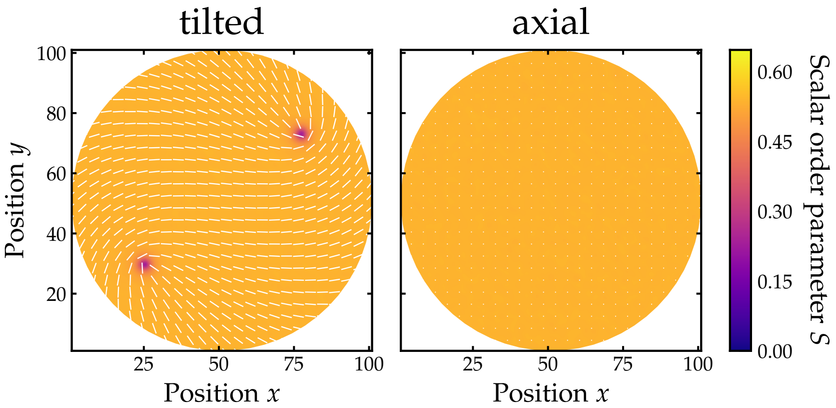

Figure 4.9: Equilibrium order parameter fields (activity $\Lambda = 0$) in our simulations of a cylindrical channel. The director (white lines) and the scalar order parameter (background color) are given for tilted and axial anchoring.

will align the NLC uniformly along the z-axis. The other setups enforce the formation of defects, since loop integrals along the cylinder boundary evaluate to a director angle change of 2π. We observe that the implied charge of $n = 1$ is always distributed in the form of two $+1/2$ disclination lines, even if the system is initialized with a central $+1$ defect and an otherwise smooth order parameter field. This is consistent with experiments (see section 2.5). The position and orientation of the defects depends on the specifics of the system. Figures 4.8 and 4.9 show 2D cross-sections of the equilibrium states our four setups reached. Motivated by the geometry and symmetry of our systems, we use 2D polar coordinates $(\bar{R}, \phi)$. The only positions with mesoscopic relevance are those of the defects $\mathbf{r}_d$. To increase generality, we normalize the distance from the center $\mathbf{r}_c$ with the cylinder radius

$$R \equiv \frac{\bar{R}}{R_c} = \frac{|\mathbf{r}_d - \mathbf{r}_c|}{R_c}. \tag{4.3}$$

The value of R will generally be close to identical for both defects, so we take the average. We find, that independently of the anchoring condition, the equilibrium defect separation is $R_0 = 0.67$. The boundary conditions change the orientations of the defects, which we parameterize via the angle ϑ (see figure 4.10). For circular anchoring the defects face outward ($\vartheta = \pi$), for radial anchoring they face inward ($\vartheta = 0$), and for tilted anchoring their symmetry axes are orthogonal to the radial vector ($\vartheta = \pi/2$).

As minor activity $\Lambda \in (0, 0.02]$ is introduced into the system, the steady state changes. Defects are subjected to new stresses and macroscopic flow fields form. The extensile active force advects them in the direction of their heads. However, this deviation from equilibrium leads to an increase in free energy. The resulting elastic force counteracts the activity. As the order parameter field becomes increasingly distorted, the elastic force grows, until both forces cancel out. This defines a new steady state with laminar flow and different defect positions.

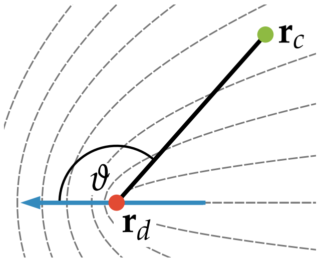

Figure 4.10: We describe the orientation of the defect (blue) in terms of the angle ϑ. The cylinder center $\mathbf{r}_c$ is marked in green, the defect position $\mathbf{r}_d$ in red.

Since with circular anchoring the defects face outward, here R increases with extensile activity. Radial anchoring has the defects facing inward, leading to a decrease of R with increasing Λ.

If the anchoring director angle is tilted at a 45° angle the defect configuration becomes chiral. Since the defects are no longer oriented along a symmetry axis of the system, the elastic force and the active force are not antiparallel. Consequently, they cannot cancel out and a net force on the defect remains. We observe the formation of a non-equilibrium steady state. The uncompensated force component drives each defect roughly in a circle around the center. Figure 4.11 shows the trajectories of both defects at low and high activity. They turn from circles (close to equilibrium) into ellipses, as $|\Lambda|$ increases. In contractile systems the defects deviate more from circular trajectories, resulting in higher eccentricity. In extensile systems the ellipses are less pronounced, but the trajectories of the two defects separate. Independently of the activity, each defect enters its final trajectory within the first 40 000 time steps. After completing an orbit, it retraces its steps, exactly. A closer look at the defects' polar coordinates over time (figs. 4.12 and 4.13) reveals that they orbit the center at varying velocities, depending on Λ. Starting at activities $|\Lambda| \approx 0.02$, both the defects' distances from the center, and their velocities v_d (fig. 4.14), begin to oscillate. The oscillation period matches a half-orbit, implying that once both defects have swapped positions, the system is back in the same state. However, this symmetry is broken at high extensile activity. Figure 4.14 shows that for $\Lambda > 0.1$ a period turns into a half-period. At such a large activity the trajectories of both defects are no longer identical, as illustrated in figure 4.11 **(c)**.

The trajectories vary in their average radii. Figure 4.15 compares this effect to the shifts we observed for circular and radial anchoring. For tilted anchoring, R seems to be roughly centrally symmetric with respect to the activity Λ. As contractile activity increases, it appears to approach a value of $R_- = 0.82$ asymptotically. R reaches a minimal value $R_{\text{min}} = 0.54$ at extensile activity $\Lambda_c = 0.035$, before slowly increasing back to values near R_0. The critical value Λ_c is the same for all boundary conditions and marks the onset of capillary flow (see below). If the anchoring is circular, the steady state is always static in terms of the velocity and

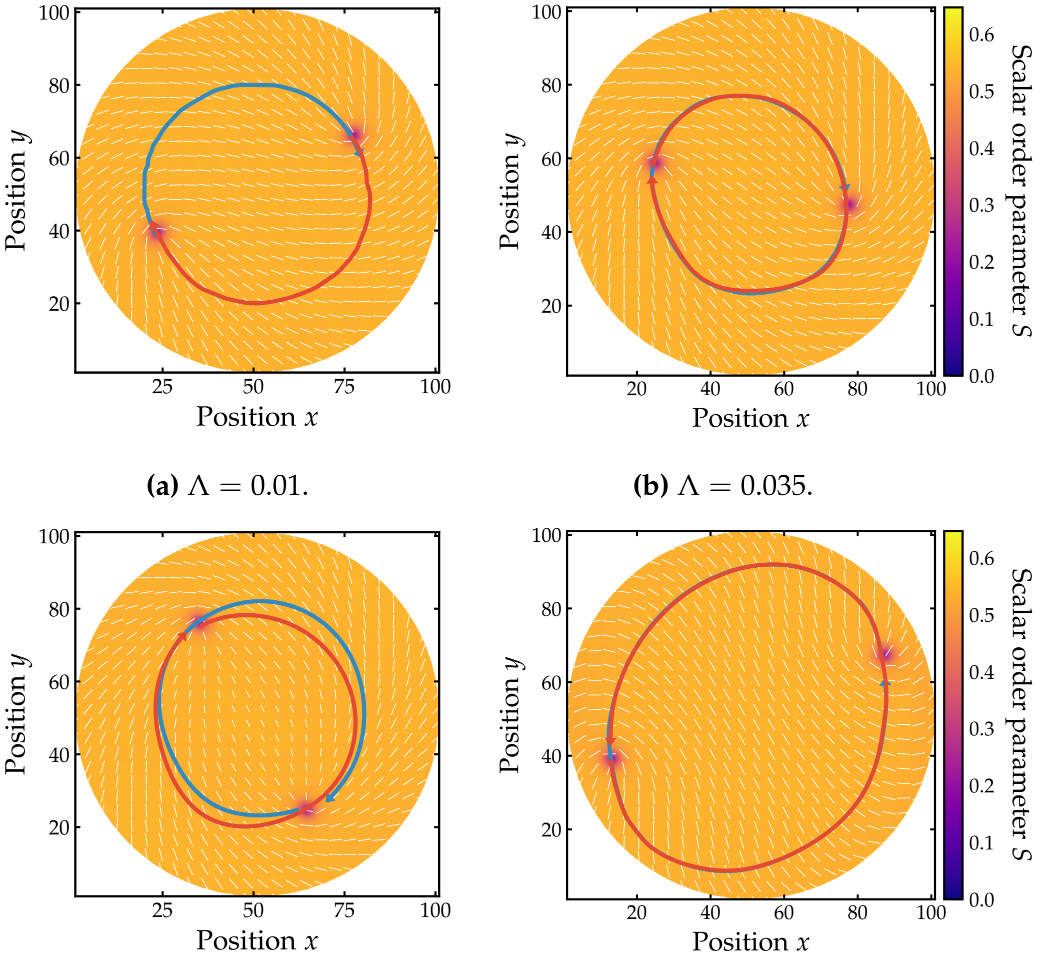

(a) $\Lambda = 0.01$. **(b)** $\Lambda = 0.035$.

(c) $\Lambda = 0.11$. **(d)** $\Lambda = -0.11$.

Figure 4.11: Trajectories of both defects (blue and red arrows) for tilted anchoring at **(a)** low activity, **(b)** moderate activity, **(c)** high contractile activity, and **(d)** high extensile activity.

order parameter fields. R is not centrally symmetric with respect to activity. Contractile stress has a significantly greater effect for this type of anchoring, reducing R to less than 0.4. The large anchoring strength W_A could be responsible for the low maximal distance $R = 0.81$ we observe, by keeping defects away from the walls.

In the case of radial anchoring, the pattern of defect shifts described above continues up until moderate extensile stress and even for high contractile activity. Interestingly, at critical value $\Lambda_c = 0.035$ the radially anchored system breaks its axial symmetry about the line through both defects. The laminar flow becomes unstable, the defects orient sideways in opposite directions, and begin orbiting the center, as if the anchoring was tilted. Comparing the defect velocity with the tilted anchoring (fig. 4.17), we see that they have similar values, until at about $\Lambda = 0.1$

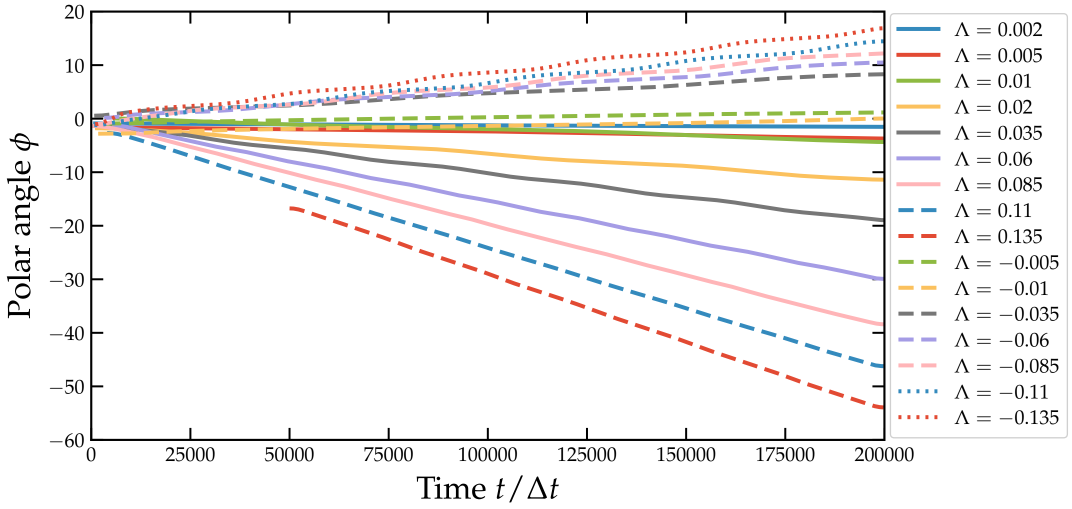

Figure 4.12: Average polar angle (in radians) of both defects over time for tilted anchoring at different activities Λ. Constant phases have been applied for an approximate initial alignment.

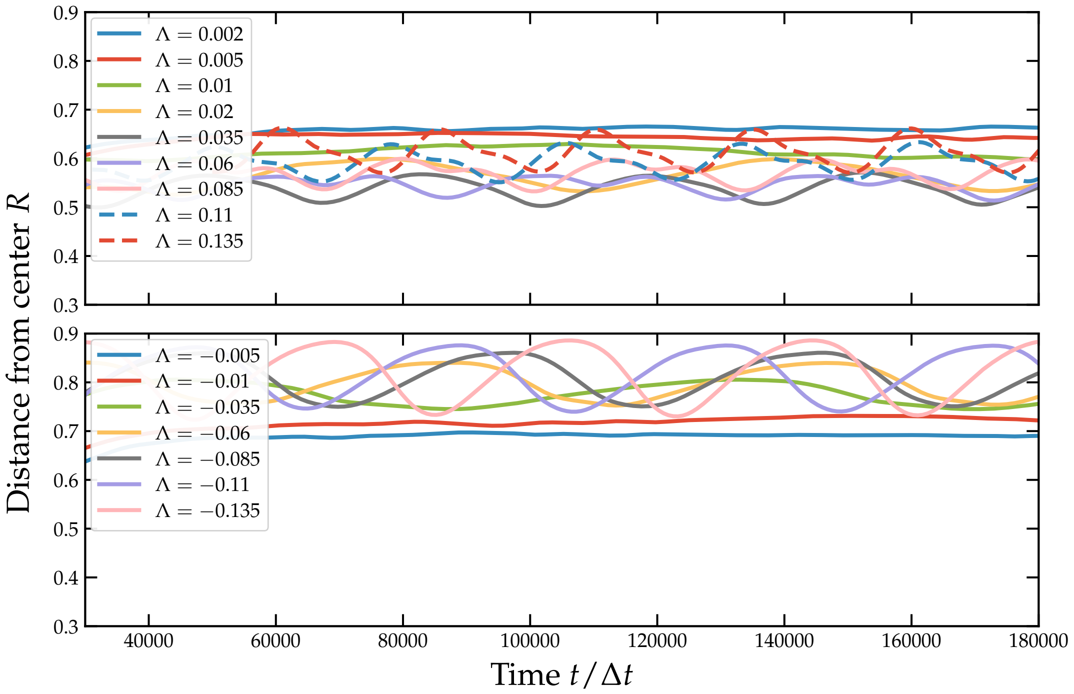

Figure 4.13: Normalized defect separation from the center R for tilted anchoring as a function of time at different activities Λ. Systems with extensile active stress are shown in the upper panel, systems with contractile stress are below.

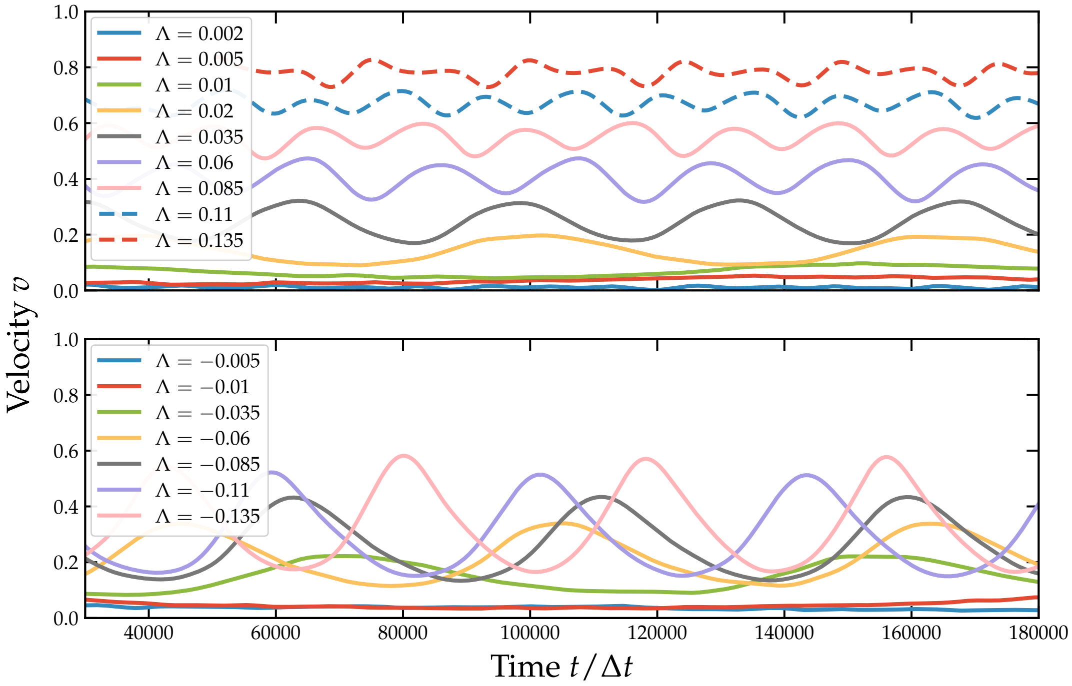

Figure 4.14: Average velocities of both defects for tilted anchoring as a function of time at different activities Λ.

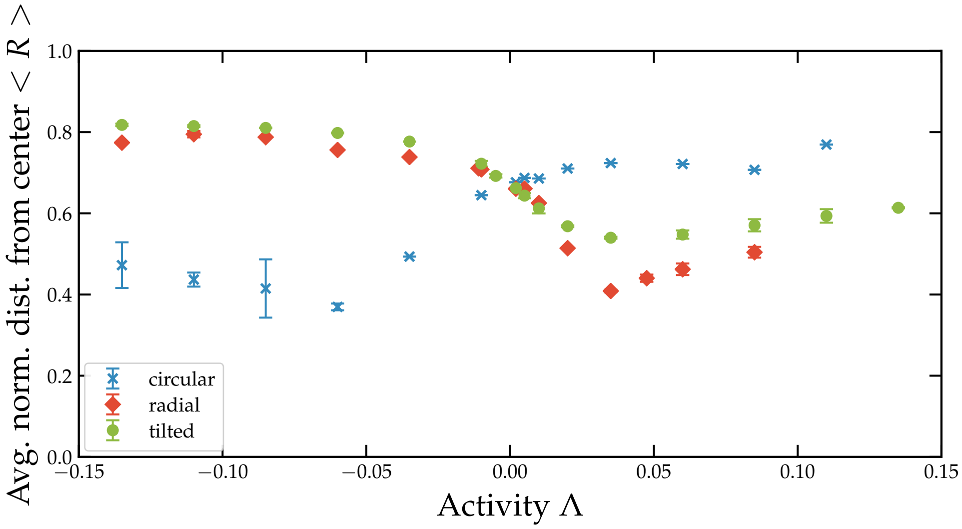

Figure 4.15: Time averages of normalized defect separation from the center R at differing activities Λ for different anchoring conditions.

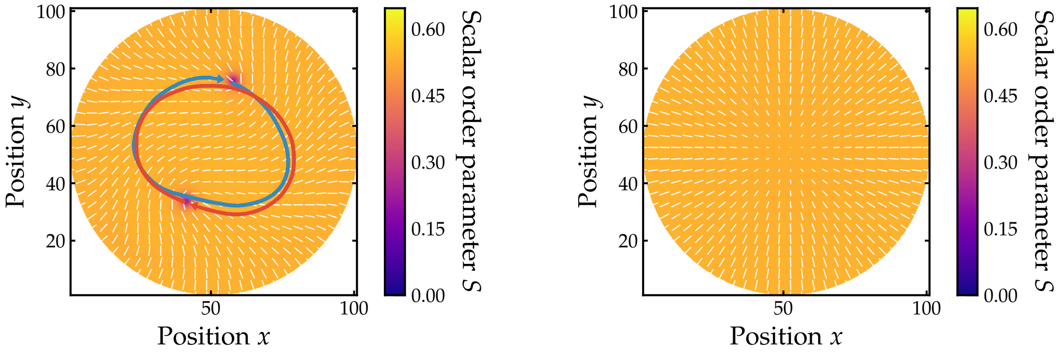

(a) The trajectories of the defects (blue and red arrows) at $\Lambda = 0.085$ do not overlap, but remain close to the central axis.

(b) At activity $\Lambda > 0.1$, after a brief damped oscillation, the defects escape in the third dimension.

Figure 4.16: At high activity the radially anchored system exhibits an oscillating steady state, and an escape of the defects.

the defects escape in the third dimension (fig. 4.16 **(b)**) for radial anchoring. The trajectory of the highest activity we recorded for the steady state is shown in figure 4.16 **(a)**. As with tilted anchoring, the trajectories of both defects separate at high activity. The emergence of this state is clearly visible in the $R(\Lambda)$ diagram (fig. 4.15). At ($\Lambda_c = 0.035$, $R_c = 0.4$) the free energy seems to heavily penalize further convergence of both defects, creating an elastic force exactly opposed to the active one. The forces become so large, that thermal fluctuations reorienting the forces cause an instability, which grows, until the new steady state is reached.

For tilted anchoring, the defect velocity v_d seems to be linear in the activity parameter Λ, with different proportionality constants $k_\pm$ in the extensile ($+$) and in the contractile ($-$) case. A linear regression suggests $k_+ = 6.3$ and $k_- = -2.5$ with quotient $-k_+/k_- = 2.6$. The oscillation frequency f_d, shown in figure 4.18, follows a similar pattern. For radial anchoring above Λ_c the defect velocity is similar to the tilted system, before leveling off quickly, as the defects escape in the third dimension. With these boundary conditions the oscillation frequency is higher, because the defects stay closer to the capillary center $\mathbf{r}_c$. This becomes apparent with consideration of the trajectory length $C = 2v_d/f_d$ of a period, given in figure 4.19. Assuming convexity, the longest trajectory possible for a disclination line is a circle with length $C_0 = 314$. If the activity is contractile, C saturates at around $\Lambda = -0.05$ for a maximal value of 253, corresponding to $C_{\max} = 0.80C_0$. Close to equilibrium we have $C = 2\pi R_0 R_c = 210 = 0.67C_0$. For extensile activity C drops to a minimal value $C_{\min} = 168 = 0.54C_0$ at Λ_c, before slowly increasing. In the case of radial anchoring $C(\Lambda)$ follows a similar pattern, but is consistently about 20% smaller.

The velocity field in the xy-plane cannot be resolved well given our system dimensions, but similarly to Ravnik *et al.* [70] we observe different modes of flow along the capillary axis. Given circular anchoring and extensile activity of

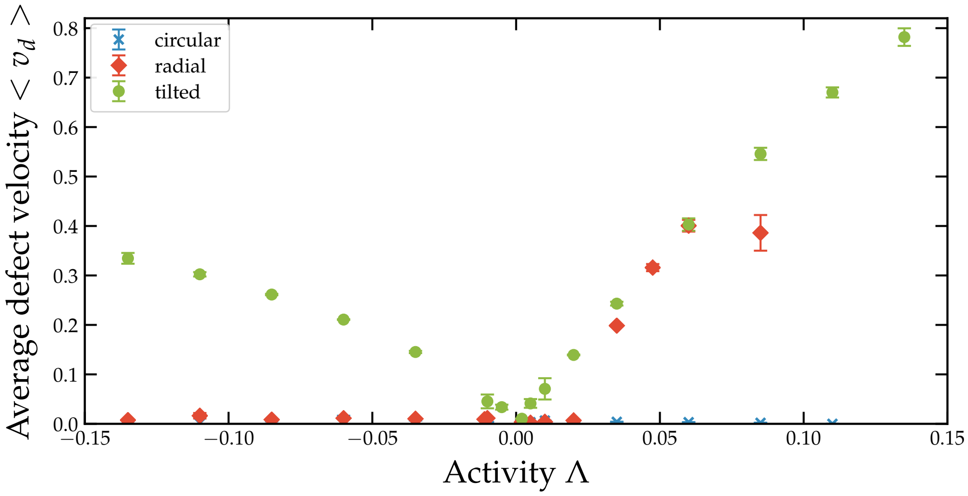

Figure 4.17: Time averages of defect velocity $< v_d >$ at differing activities Λ for different anchoring conditions.

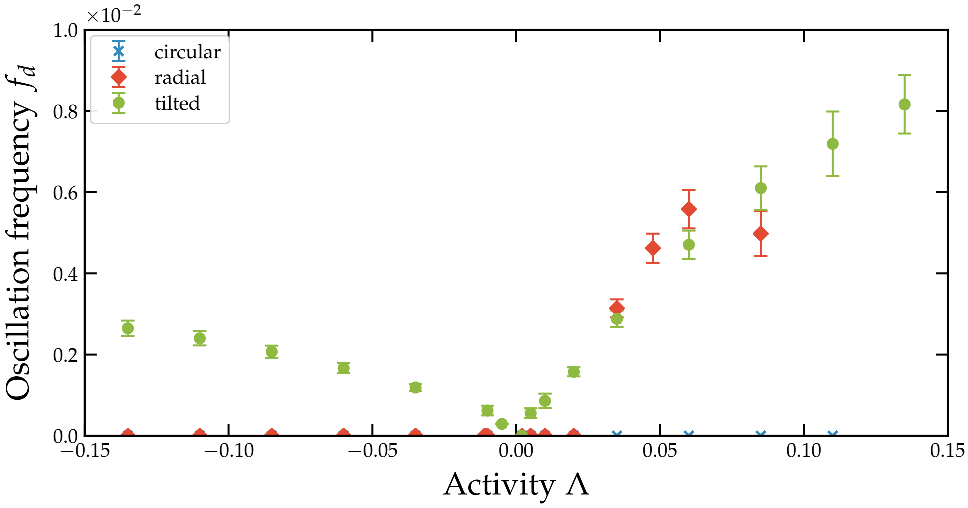

Figure 4.18: The oscillation frequency f_d of a half-orbit applies to the defect velocity v_d and the distance from the center (R). The plot shows time averages of f_d for varying boundary conditions and activity. Non-oscillating configurations, are defined to have $f_d \equiv 0$.

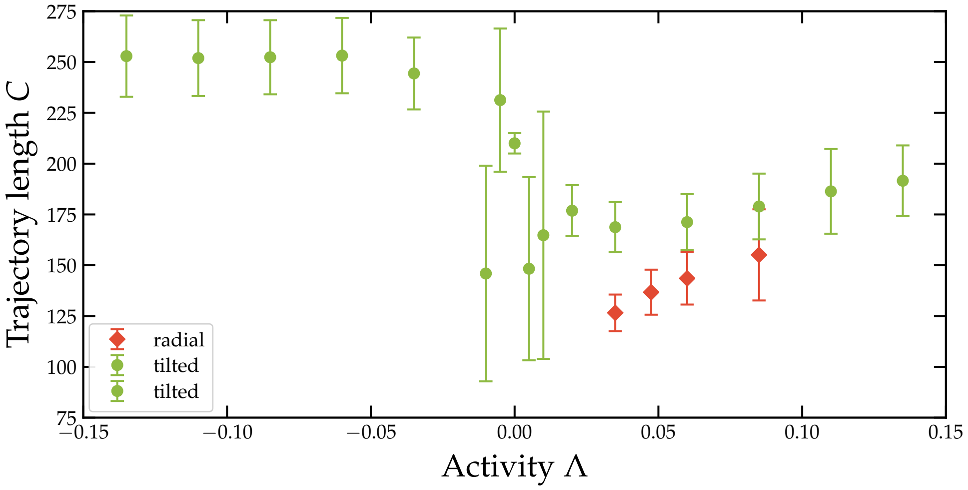

Figure 4.19: Distance traveled by a defect doing a single orbit around the center $C = 2v_d / f_d$ for different activities and anchoring conditions.

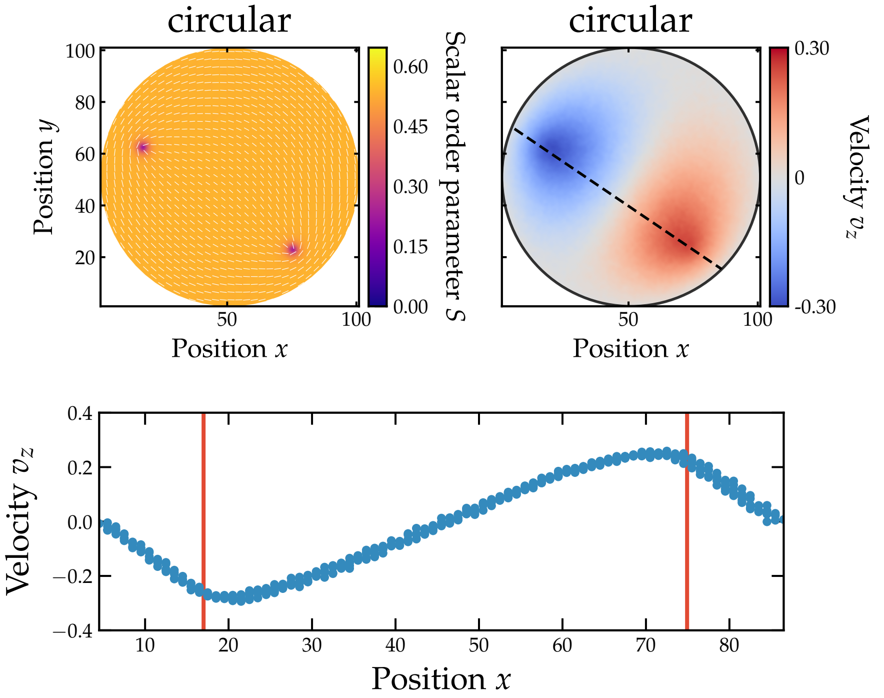

Figure 4.20: Order parameter field (top left), capillary velocity field (top right), and cross-section of the velocity at activity $\Lambda = 0.06$. The cross-section is marked by a dashed line in the upper right image. The defect positions are pointed out by red vertical lines in the plot.

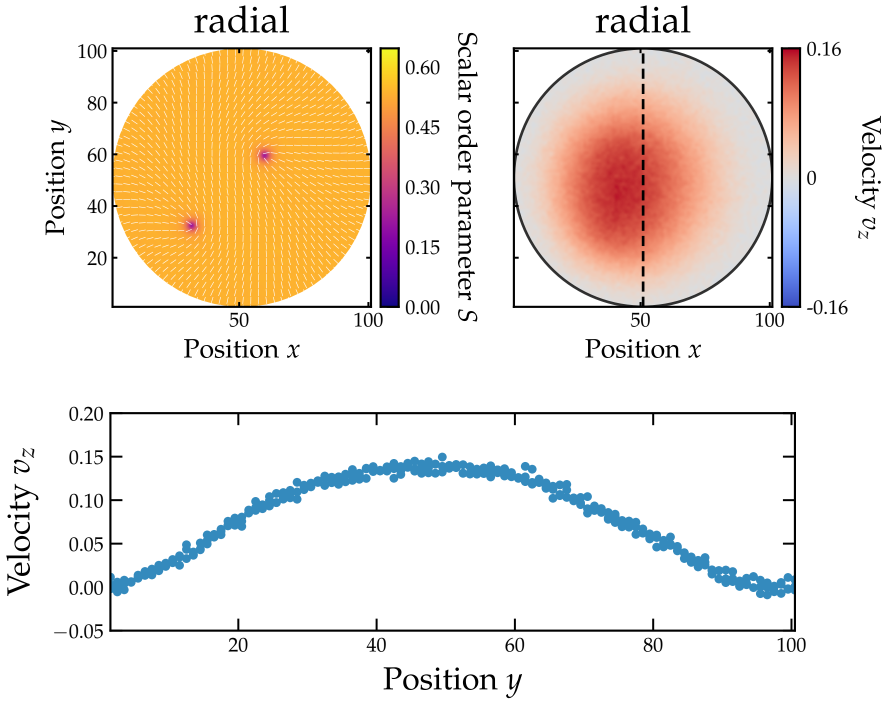

Figure 4.21: Order parameter field (top left), capillary velocity field (top right), and cross-section of the velocity at activity $\Lambda = 0.035$.

$\Lambda \geq \Lambda_c$, a bidirectional flow pattern forms. It reaches its extremal values close to the defects. Figure 4.20 shows the order parameter and flow field at $\Lambda = 0.06$, as well as a cross-section of the capillary velocity v_z. At activities of this magnitude the defects tend to deviate slightly from their mirror-symmetric positions. The cross-section is, therefore, superimposed on the line connecting both defects. The velocity changes almost linearly from 0 at the walls to the minimum (maximum). Between the extrema the velocity gradient $\partial_x v_z$ is also close to constant. Given radial anchoring, we observe three different modes of capillary flow. At activity $\Lambda = \Lambda_c$ a unidirectional flow emerges (fig. 4.21). Exhibiting an inflection point ca. 20 units from the walls, it differs considerably from the Poiseuille flow seen in section 4.1.1. The direction of the flow is sensitive to the randomized initial conditions and thermal fluctuations. At $\Lambda \geq 0.085$ the disclination lines orbiting the center are accompanied by a bidirectional flow pattern that appears to differ slightly from the one we observe for circular anchoring (fig. 4.22). The increase in velocity near the walls and the cylinder axis is stronger than linear. As with circular anchoring, the two channels are induced by, and co-localized with the defects. Therefore, they revolve around the center, together. When the defects escape in the third dimension, the capillary flow field changes again to the unidirectional flow we saw earlier. Here, the maximal z-velocity is reached at the line (position in the xy-plane) where the local director is parallel to the z-axis $\mathbf{n} \parallel \hat{\mathbf{e}}_z$. Figure 4.23 shows a system that recently transitioned out of the orbiting steady state into the

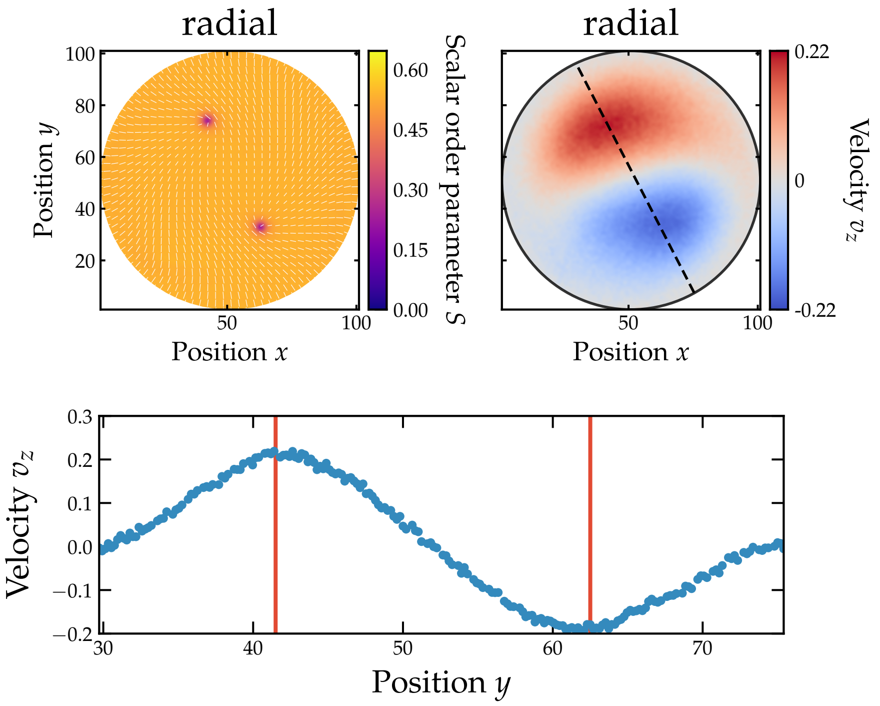

Figure 4.22: Order parameter field (top left), capillary velocity field (top right), and cross-section of the velocity at activity $\Lambda = 0.085$.

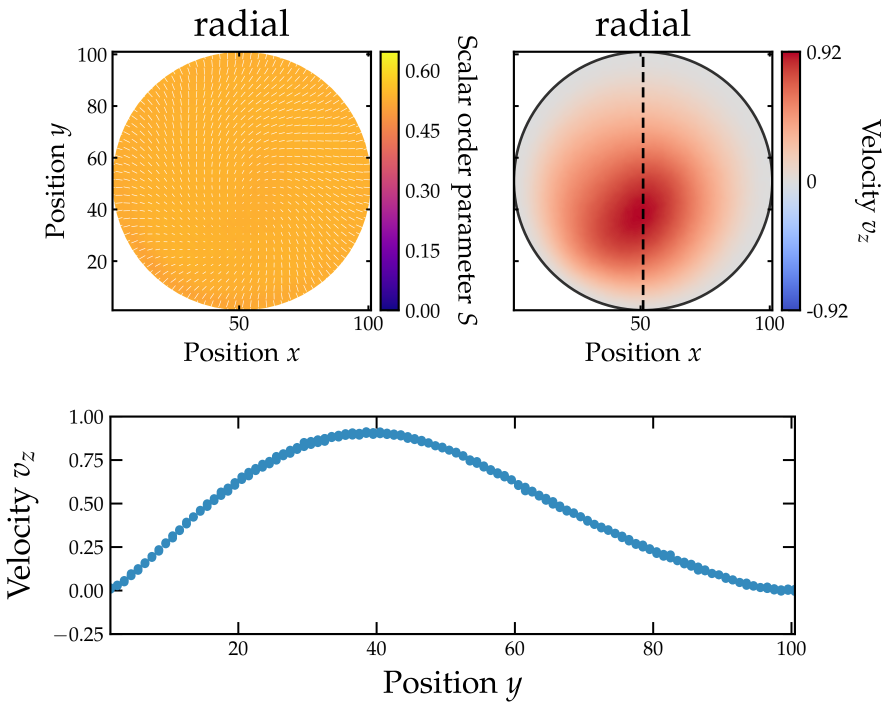

Figure 4.23: Order parameter field (top left), capillary velocity field (top right), and cross-section of the velocity at activity $\Lambda = 0.09$.

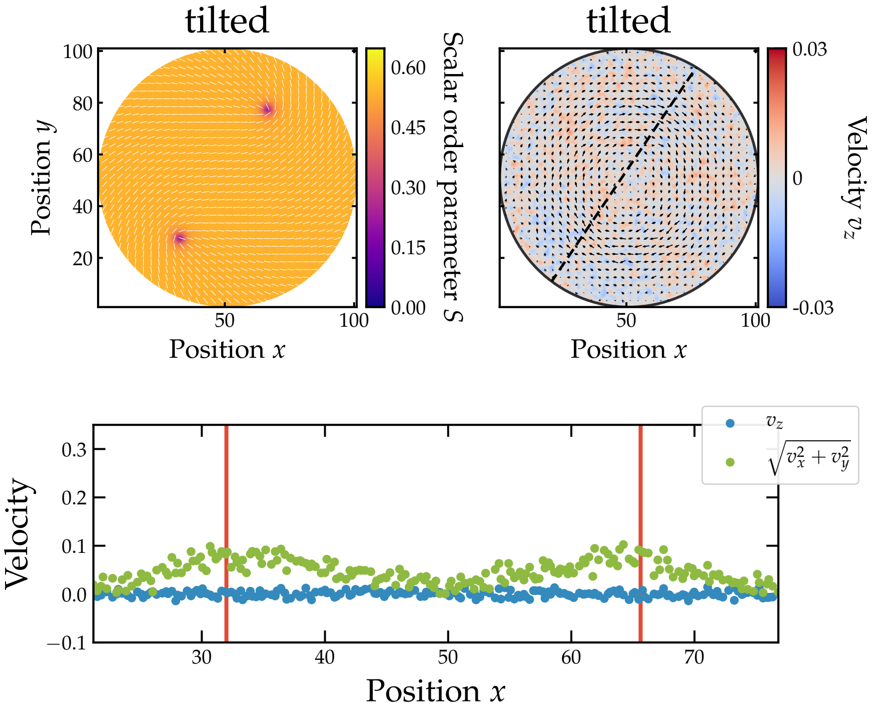

Figure 4.24: Order parameter field (top left), velocity field (top right), and cross-section of the velocity at activity $\Lambda = 0.01$.

defect-less state and still has a twist in the director, as well as an off-center flow maximum.

If the anchoring is tilted, capillary flow also starts to form at activity Λ_c. Since the flow in the xy-plane is less delicate for this anchoring, we can resolve it to a sufficient degree. Figure 4.24 shows a simulation below Λ_c. The only movement along the capillary axis is thermal noise. In the xy-plane, however, a vortex rotates the NLC. As the critical value Λ_c is reached, a bidirectional capillary flow emerges (fig. 4.25). Unlike for circular and radial anchoring, the lines of maximum flow seem to coincide with the disclination lines. The planar flow peaks at the same locations. Its flanks appear flat. This changes, as activity is increased further. At $\Lambda = 0.085$ (fig. 4.26) the flow magnitude has grown in all components. The absolute value of the planar velocity has a Poiseuille-like profile in each half-plane, as there is no inflection point. The two opposed channels revolve around the central axis, together with the defects.

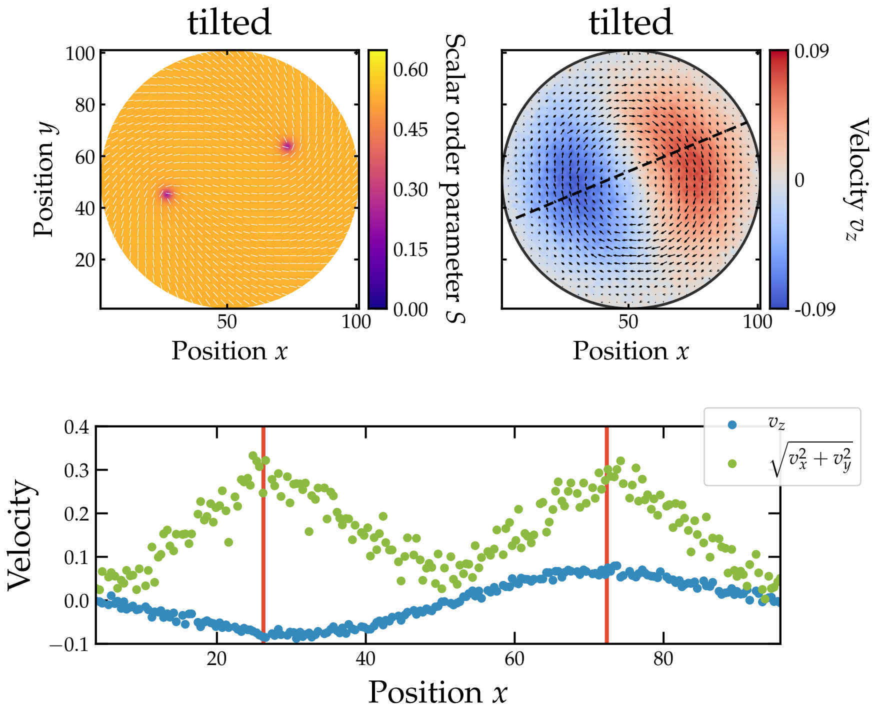

Figure 4.25: Order parameter field (top left), velocity field (top right), and cross-section of the velocity at activity $\Lambda = \Lambda_c = 0.035$.

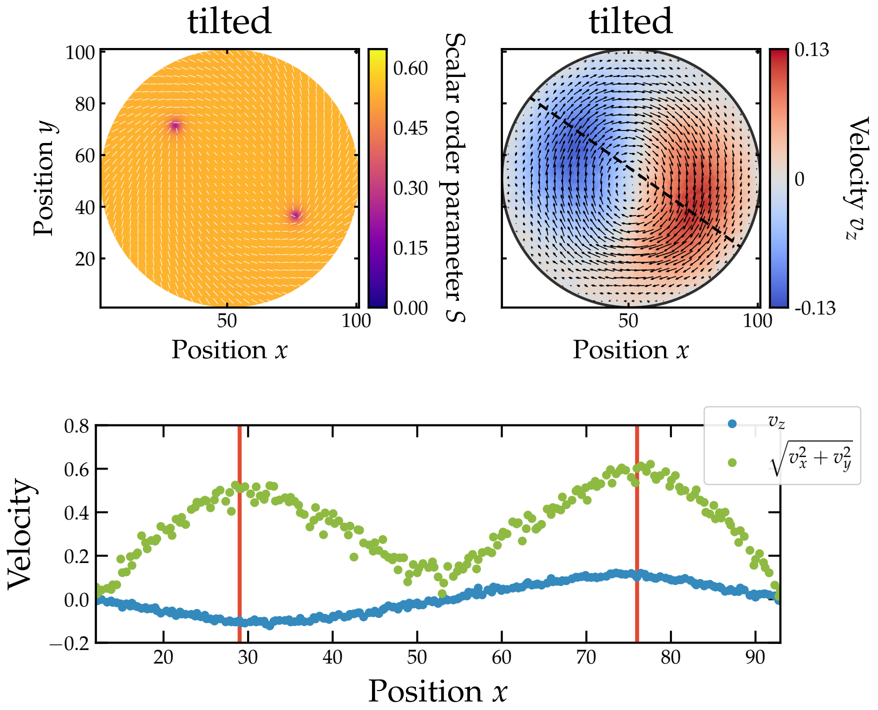

Figure 4.26: Order parameter field (top left), velocity field (top right), and cross-section of the velocity at activity $\Lambda = 0.085$.

4.2.2 Elliptical Cross-Section

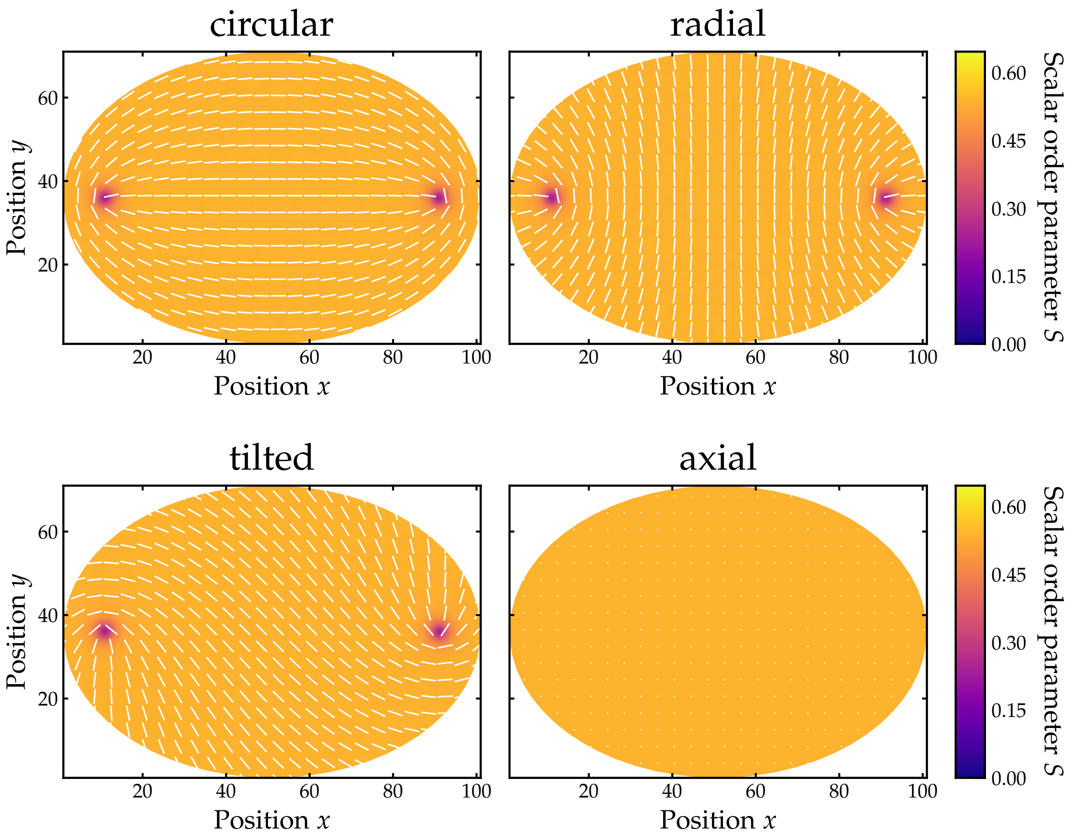

Figure 4.27: Equilibrium order parameter fields in our simulations of an elliptical channel. For each of the four anchorings the director (white lines) and the scalar order parameter (background color) are given.

In addition to the systems described above, we briefly investigated capillaries with an elliptical cross-section. Choosing a major axis $2R_e = 100$ and a minor axis $2r_e = 70$ for the ellipse, we found that the reduced symmetry of the system forces the defects in the same positions, independently of initial conditions and thermal fluctuations. They always align along the major axis, with a distance $\bar{R} = 40$ from the center. Normalizing with R_e, this corresponds to $R = 0.8$. Figure 4.27 shows the equilibrium order parameter fields for all examined types of anchoring.

Outside of equilibrium, steady states with static order parameter configurations also have fixed defect polar angles of $\phi_{1,2} = \pm\pi$. Besides this loss of symmetry, the deformation of the capillary does not change the behavior we observe qualitatively, irrespective of the anchoring condition. The most significant quantitative change is a shift in the critical activity Λ_c, where the radially anchored system enters an orbiting steady state, to ca. $\Lambda_c^{\text{ell}} = 0.06$.

For tilted anchoring, the defects move in an ellipse, even at low activity. They accelerate very distinctly when traveling parallel to the (elongated) x-axis, and

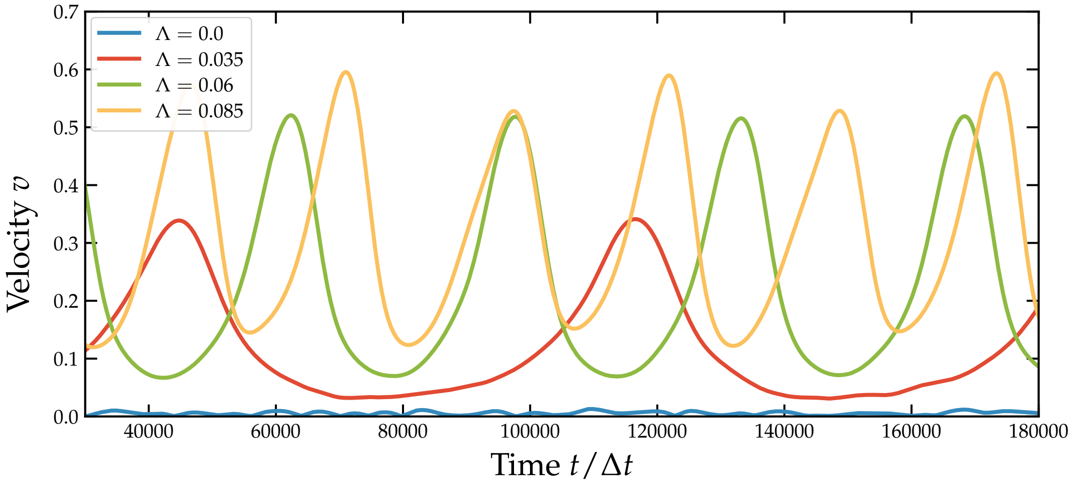

Figure 4.28: Average velocities of both defects over time at different activities Λ. In cylindrical confinement with elliptical cross-section.

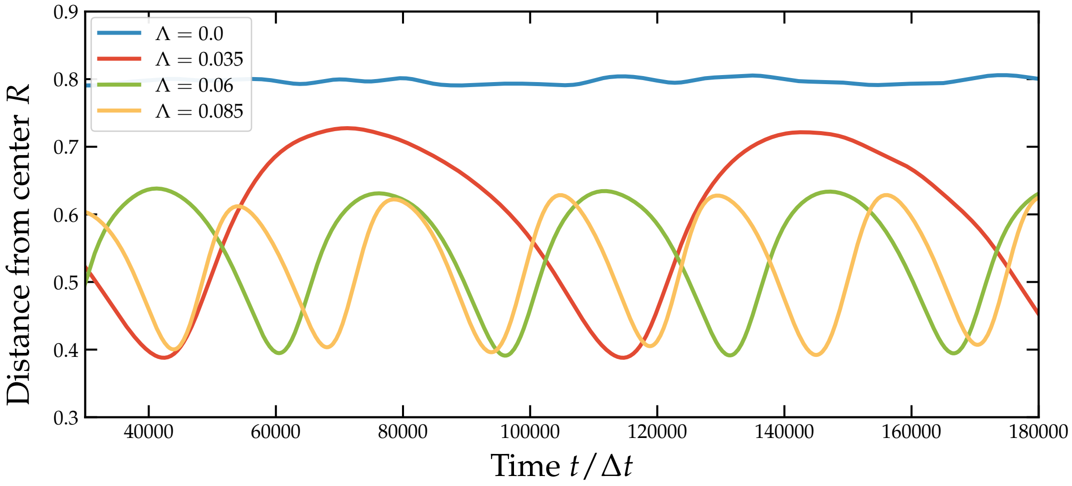

Figure 4.29: Normalized defect separation from the center R as a function of time at different activities Λ and for different anchoring conditions in the elliptical channel.

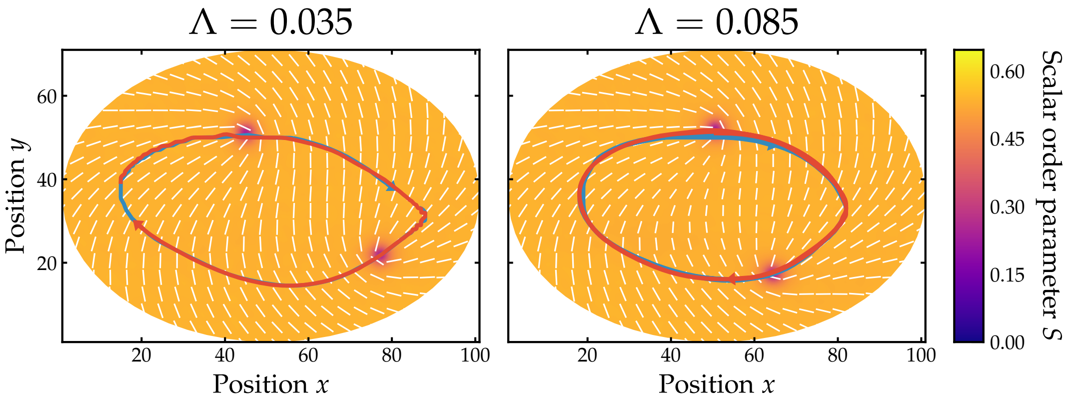

Figure 4.30: Trajectories of both defects (blue and red arrows) for tilted anchoring in confinement with elliptical cross-section.

slow down enormously when close to the high curvature apex. Figure 4.28 shows that the difference between the maximal and the minimal velocity is about a factor of 6. For comparison, in the cylindrical capillary the maximal velocity was only 15 % to 50 % larger. The effect is most pronounced at $\Lambda = 0.035$, where the maximal velocity is 10 times higher than the turning velocity. The defects are unable to turn smoothly and overshoot their minima in the energy landscape. As a result, they reverse orientations rather sharply and asymmetrically, even after a long simulation time (see figure 4.30). Another consequence is, that the defects are much further from the center when turning in a $\Lambda = 0.035$ system, than when turning at higher activity (see figure 4.29). They also spend much more time there. Comparing the proportionality constant between v_d and Λ to the setups with circular cross-section, we arrive at a large discrepancy of $k_+^{\text{ell}} = 3.6 = 0.57k_+$ (see figure 4.31). As we saw, this is mostly due to a difference in minimal velocity, rather than maximal velocity. The onset of the capillary flow field is shifted to $\Lambda = 0.06$, just as for the oscillating state. Qualitatively, the behavior remains the same. Figure 4.32 gives the axial velocity field for radial anchoring with $\Lambda = 0.85$. At this activity, after 175 000 time steps in a damped version of the oscillating state, the defects escaped in the third dimension. The flow remained unidirectional for the entire time.

For axial anchoring, variations in the activity parameter Λ had no effect. In both the circular and elliptical capillary the equilibrium state was maintained. More details are given in the discussion (chapter 5).

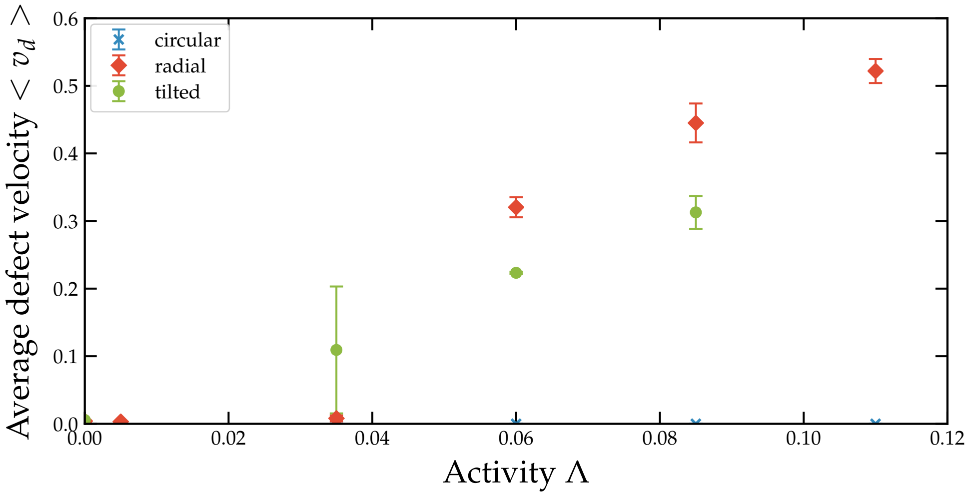

Figure 4.31: Average velocities of both defects for tilted anchoring as a function of time at different activities Λ in the elliptical channel.

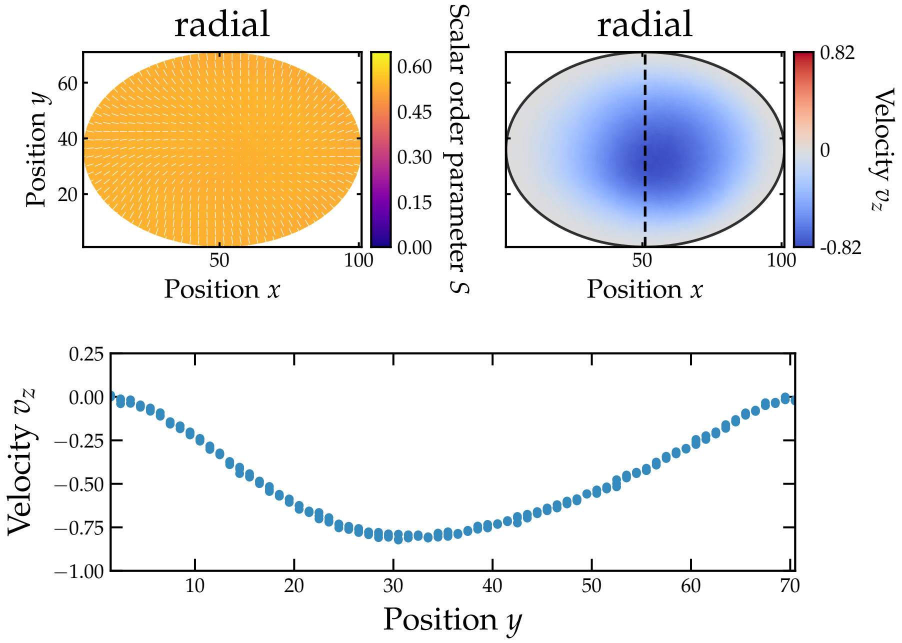

Figure 4.32: Order parameter field (top left), capillary velocity field (top right), and cross-section of the velocity at activity $\Lambda = 0.085$ for the deformed cylinder.

Chapter 5

Discussion

Initially, we tried to implement an SRD-version of Ericksen-Leslie nematodynamics. With this formulation in terms of the director $\mathbf{n}$ we encountered many problems. When anchoring $\mathbf{n}$ at a boundary, there was no practical way to allow both $\mathbf{n}$ and $-\mathbf{n}$ equally. Since a choice had to be made, this choice would impose a director configuration on the system, that was not necessarily physical. This is because the opposite choice could permit lower free energy configurations. Another issue was the miscalculation of spatial derivatives in the presence of $n = \pm 1/2$ defects. Since the director only rotates by an angle $\pm\pi$ on any contour around them, it has to change sign discontinuously at some point. This problem is only solved by considering a quantity quadratic in $\mathbf{n}$, such as the order parameter $\boldsymbol{Q}$.

Our algorithm has shown to be sufficiently robust. Specifically, many alternatives corresponding to physical initial conditions or computational variations have no impact on the results of simulations. If, for example, instead of setting the ghost particles' velocities to 0 at each time step, we redistribute them normally, the behavior of the system is unchanged. To initialize the system isotropically, we can set $\boldsymbol{Q}_i(t = 0) = \mathbf{0}$ for every particle i, or we can choose a random director $\mathbf{n}_i(t = 0)$ for each particle and use eq. (2.12) for uniaxial NLCs with $S = 1$ to construct $\boldsymbol{Q}_i(t = 0)$. Both evolve toward equilibrium in the same way.

In equilibrium the number density of MPCD-particles was constant across the whole domain. At high activity, however, the distribution was no longer homogeneous. Since circular anchoring orients the defects with their heads facing outwards, the active force drives particles to the bounds of the domain. The effect was not strong in our simulations. Average cell number density varied from $N_\alpha = 55$ at the center to around 65 near the walls. For radial anchoring the effect is reversed. The generally high number density peaks around halfway from the center and drops dramatically at the border with similar magnitudes as in the circular case. Both distributions are shown in appendix A.3. In oscillating systems with tilted anchoring we observed much larger inhomogeneities. Independently of the sign of Λ (see appendix A.3), at high absolute values, the outer half of the cylinder had almost twice as many particles per cell as the inner volume.

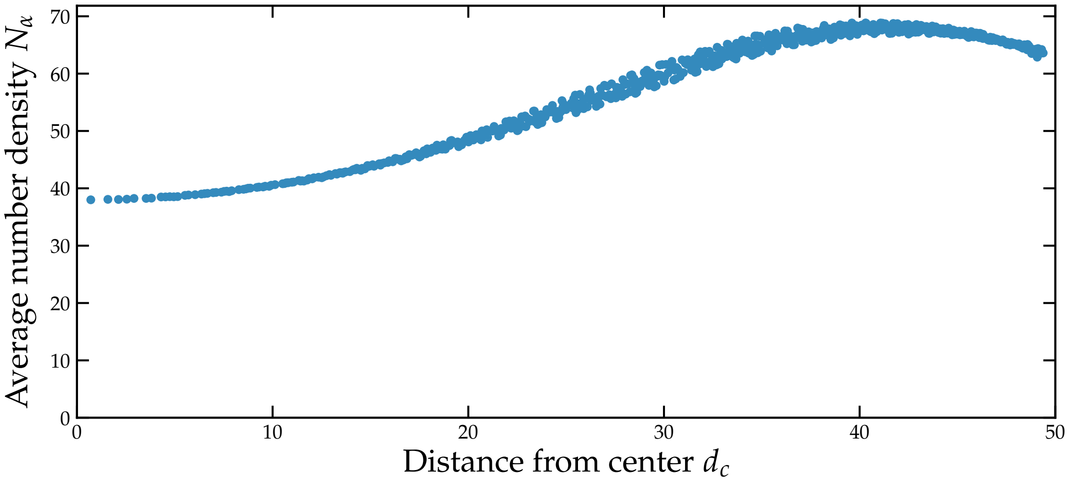

Figure 5.1: Average cell number density N_α for tilted anchoring at high activity ($\Lambda = 0.135$).

Figure 5.1 shows how number density increases gradually with distance from the center d_c, and peaks near the boundary. This means, that the average number of MPCD-particles per cell N of the simulation has to be chosen high enough to remain meaningful in dilute regions of active systems. In our case, a value of $N_\alpha^{\text{min}} = 37$ should be high enough.

In the scope of this thesis we were able to develop an algorithm capable of modeling active NLCs on the mesoscale. It captures microscopic fluctuations, is highly tunable, and suited for complex boundary conditions. We used it to study the behavior of an active NLC in cylindrical confinement, as well as in a deformed capillary with a compressed axis. For circular and radial anchoring at low extensile activity the defects were shifted in the direction of their heads with increasing Λ. The same behavior has been observed in lattice Boltzmann simulations by Ravnik *et al.* [70]. We were able to cover a wider range of activities, including contractile stress, and saw the trend of shifted defects continue. For a previously unstudied type of tilted anchoring and for radial anchoring at high activity we discovered a new non-equilibrium steady state, in which the disclination lines orbited the capillary center in ellipses of varying aspect ratios. This dynamical mode has features resembling those Keber *et al.* [1] found for active NLCs confined to a vesicle surface (see section 2.8). Strong topological confinement with sharply defined minima in the energy landscape come in conflict with the active force, driving the system out of equilibrium. Our simulations of the deformed capillary demonstrated that along the major axis of the system the defects were able to accelerate with few constraints. As they encountered the opposed stress emanating from the boundaries, they were very fast, overshooting the energetic minimum imposed by the elastic forces. Consequently, for a while, the active and the elastic force facilitate one another, accelerating both defects. The result is an oscillating steady state. Like Keber *et al.* we found the oscillation frequency to be linear in the activity parameter Λ.

We were not able to confirm the findings of Ravnik *et al.* for axial anchoring. While they observed two different modes of flow, in our simulations no convective velocity field emerged. The same modes did, however, appear for radial and circular anchoring. At high activity we saw, both, a unidirectional flow, and a bidirectional flow, pinned by the defects.

Our study of extensile and contractile active stresses revealed large asymmetries between the two. For tilted anchoring and given $|\Lambda|$ the positive value results in a high frequency, low amplitude oscillation, whereas a negative value has the opposite effect. Further, we observed the separation of both defects' trajectories. This happened exclusively at high extensile activity. In all other cases, the trajectories of both defects traced identical paths. Although extensile forces in radially anchored systems act in the same direction as contractile forces in circular anchoring, the behavior of both was different quantitatively, as well as qualitatively, with circularly anchored systems never entering an oscillating state.

The (non-deformed) geometry we investigated is identical to the one explored by Ravnik *et al.* in [70]. In addition to the many commonalities described above, there were some discrepancies. Especially, the absence of flow in our capillaries with axial anchoring was surprising. Moreover, we saw no difference in the defects' equilibrium positions between circular and radial anchoring. Apart from us studying a broader range of activities, the main physical differences to Ravnik *et al.* were a high rotational diffusion constant (low rotational viscosity), very strong anchoring, and a different capillary radius in our case. It would be useful to look at different regimes for these parameters. More suggestions for extending the scope of this project are given in the outlook.

Chapter 6

Outlook

Our algorithm allows the study of rather complex geometries. For example, it would be interesting to incorporate boundary conditions matching those of an active NLC confined to the surface of a lipid vesicle, as in [1]. A weak homogeneous anchoring that is agnostic of the in-plane angle could be implemented, to keep the directors pointed mostly parallel to the sphere. However, the surface would have a finite thickness, and be incapable of deforming.

It would be interesting to drop the one-constant approximation. Our algorithm can be easily extended to solve for a more complex free energy. As seen in section 2.5, the relationship between the elastic constants determines which director patterns are stable. A generalization to $K_2 \neq K_1 = K_3$ would not even require expanding to a higher order in $\boldsymbol{Q}$ (see section 2.4), and is important in confined geometries where strong deformation is imposed by the boundaries [34]. Here, an energetically cheaper twist will replace other types of deformations and might lead to the emergence of chiral structures [86]. It has also been found to introduce an explicit coupling between the director and the order parameter [87, 88]. In reality, for different types of LCs, the splay-, twist- and bending viscosities $\eta_{1,2,3}$ can also differ substantially. In our model this would lead to the introduction of multiple rotational diffusion constants Γ_i. However, since the relevant parameter for the dynamics is the characteristic director relaxation time $t_i = \eta_i / K_i = 1/\Gamma_i K_i$ the variation in η_i can be absorbed into the elastic constants K_i. To model lyotropic chromonic LCs, for example, the modification $K_3 \gg K_1 \gg K_2$ would have to be made, since $t_3 \ll t_1 \ll t_2$.

Overall, the main advantage of our adapted NLC-MPCD algorithm is that it can be tuned and modified to include a limitless variety of additional boundary conditions, and interactions, even with foreign particles submerged within, while remaining computationally efficient.

References

[1] F. C. Keber, E. Loiseau, T. Sanchez, S. J. DeCamp, L. Giomi, M. J. Bowick, M. C. Marchetti, Z. Dogic, and A. R. Bausch, *Topology and dynamics of active nematic vesicles*, Science **345**, 1135 (2014).

[2] G. H. Koenderink, Z. Dogic, F. Nakamura, P. M. Bendix, F. C. MacKintosh, J. H. Hartwig, T. P. Stossel, and D. A. Weitz, *An active biopolymer network controlled by molecular motors*, Proceedings of the National Academy of Sciences **106**, 15192 (2009).

[3] H.-P. Zhang, A. Be'er, E.-L. Florin, and H. L. Swinney, *Collective motion and density fluctuations in bacterial colonies*, Proceedings of the National Academy of Sciences **107**, 13626 (2010).

[4] T. Müller, D. de las Heras, I. Rehberg, and K. Huang, *Ordering in granular-rod monolayers driven far from thermodynamic equilibrium*, Physical Review E **91**, 062207 (2015).

[5] G. Duclos, C. Blanch-Mercader, V. Yashunsky, G. Salbreux, J.-F. Joanny, J. Prost, and P. Silberzan, *Spontaneous shear flow in confined cellular nematics*, Nature Physics 1 (2018).

[6] D. Marenduzzo, E. Orlandini, M. E. Cates, and J. M. Yeomans, *Steady-state hydrodynamic instabilities of active liquid crystals: Hybrid lattice boltzmann simulations*, Phys. Rev. E **76**, 031921 (2007).

[7] V. Narayan, S. Ramaswamy, and N. Menon, *Long-lived giant number fluctuations in a swarming granular nematic*, Science **317**, 105 (2007).

[8] Y. Sasaki, V. Jampani, C. Tanaka, N. Sakurai, S. Sakane, K. V. Le, F. Araoka, and H. Orihara, *Large-scale self-organization of reconfigurable topological defect networks in nematic liquid crystals*, Nature Communications **7**, 13238 (2016).

[9] K.-T. Wu, J. B. Hishamunda, D. T. Chen, S. J. DeCamp, Y.-W. Chang, A. Fernández-Nieves, S. Fraden, and Z. Dogic, *Transition from turbulent to coherent flows in confined three-dimensional active fluids*, Science **355**, eaal1979 (2017).

[10] L. Giomi, *Geometry and topology of turbulence in active nematics*, Physical Review X **5**, 031003 (2015).

[11] Z. Krajnik, *Active turbulence*, Ph.D. thesis, Univerza v Ljubljani (2018).

[12] P. A. Pullarkat, P. A. Fernández, and A. Ott, *Rheological properties of the eukaryotic cell cytoskeleton*, Physics Reports **449**, 29 (2007).

[13] A. Frey-Wyssling, *The submiceoscopic structure of the cytoplasm*, Journal of Microscopy **60**, 128 (1940).

[14] G. W. Scarth, *The structural organization of plant protoplasm in the light of micrurgy*, Protoplasma **2**, 189 (1927).

[15] W. J. Schmidt, *Die Doppelbrechung von Karyoplasma, Zytoplasma und Metaplasma*, vol. 11 (Gebrüder Borntraeger, 1937).

[16] H. Ullrich, *Einige Beobachtungen über Doppelbrechung am lebenden Protoplasten, an verschiedenen Zellorganellen sowie der Zellwand*, Planta **26**, 311 (1936).

[17] B. Alberts, *Molecular biology of the cell* (Garland Science, 2017).

[18] B. Wickstead and K. Gull, *The evolution of the cytoskeleton*, The Journal of Cell Biology **194**, 513 (2011).

[19] G. M. Cooper, *Actin, myosin, and cell movement*, in *The Cell: a molecular approach* (Sinauer Associates, Inc., Sunderland (MA), 2000).

[20] D. A. Fletcher and R. D. Mullins, *Cell mechanics and the cytoskeleton*, Nature **463**, 485 (2010).

[21] M. I. Geli and H. Riezman, *Endocytic internalization in yeast and animal cells: similar and different*, Journal of Cell Science **111**, 1031 (1998).

[22] T. Sanchez, D. T. Chen, S. J. DeCamp, M. Heymann, and Z. Dogic, *Spontaneous motion in hierarchically assembled active matter*, Nature **491**, 431 (2012).

[23] K. Kruse and F. Jülicher, *Actively contracting bundles of polar filaments*, Physical Review Letters **85**, 1778 (2000).

[24] C. Hentrich and T. Surrey, *Microtubule organization by the antagonistic mitotic motors kinesin-5 and kinesin-14*, The Journal of Cell Biology **189**, 465 (2010).

[25] M. Kleman and O. D. Laverntovich, *Soft matter physics: an introduction* (Springer Science & Business Media, 2007).

[26] V. Tsvetkov, *On molecular order in the anisotropic liquid phase*, Acta Physicochimica URSS **16**, 132 (1942).

[27] J. Prost and P.-G. de Gennes, *The physics of liquid crystals*, vol. 83 (Oxford University Press, 1995).

[28] L. D. Landau and E. Lifshitz, *Theory of elasticity, vol. 7*, Course of Theoretical Physics **3**, 109 (1986).

[29] D. Andrienko, *Introduction to liquid crystals*, Journal of Molecular Liquids (2018).

[30] F. C. Frank, *I. liquid crystals. on the theory of liquid crystals*, Discussions of the Faraday Society **25**, 19 (1958).

[31] J. Ericksen, *Nilpotent energies in liquid crystal theory*, Archive for Rational Mechanics and Analysis **10**, 189 (1962).

[32] B. Edwards and A. Beris, *Note: Order parameter representation of spatial inhomogeneities of polymeric liquid crystals*, Journal of Rheology **33**, 1189 (1989).

[33] B. J. Edwards, A. N. Beris, and M. Grmela, *Generalized constitutive equation for polymeric liquid crystals part 1. model formulation using the hamiltonian (poisson bracket) formulation*, Journal of Non-Newtonian Fluid Mechanics **35**, 51 (1990).

[34] S. Zhou, *Elasticity, viscosity, and orientational fluctuations of a lyotropic chromonic nematic liquid crystal disodium cromoglycate*, in *Lyotropic Chromonic Liquid Crystals*, 77–92 (Springer, 2017).

[35] P. A. Lebwohl and G. Lasher, *Nematic-liquid-crystal order—a Monte Carlo calculation*, Phys. Rev. A **6**, 426 (1972).

[36] G. Lasher, *Monte Carlo results for a discrete-lattice model of nematic ordering*, Physical Review A **5**, 1350 (1972).

[37] G. Luckhurst and S. Romano, *Computer simulation study of a nematogenic lattice model based on an elastic energy mapping of the pair potential*, Liquid Crystals **26**, 871 (1999).

[38] N. D. Mermin, *The topological theory of defects in ordered media*, Reviews of Modern Physics **51**, 591 (1979).

[39] K. Kruse, J.-F. Joanny, F. Jülicher, J. Prost, and K. Sekimoto, *Generic theory of active polar gels: a paradigm for cytoskeletal dynamics*, The European Physical Journal E **16**, 5 (2005).

[40] T. J. Spencer, *Lattice Boltzmann method for Q-tensor nemato-dynamics in liquid crystal display devices.*, Ph.D. thesis, Sheffield Hallam University (2005).

[41] T. W. Kibble, *Topology of cosmic domains and strings*, Journal of Physics A: Mathematical and General **9**, 1387 (1976).

[42] H. Pleiner, *Dynamics of a disclination point in smectic-c and-c* liquid-crystal films*, Physical Review A **37**, 3986 (1988).

[43] I. Chuang, B. Yurke, A. N. Pargellis, and N. Turok, *Coarsening dynamics in uniaxial nematic liquid crystals*, Physical Review E **47**, 3343 (1993).

[44] D. Svenšek and S. Žumer, *Hydrodynamics of pair-annihilating disclination lines in nematic liquid crystals*, Physical Review E **66**, 021712 (2002).

[45] I. Muševič, M. Škarabot, U. Tkalec, M. Ravnik, and S. Žumer, *Two-dimensional nematic colloidal crystals self-assembled by topological defects*, Science **313**, 954 (2006).

[46] W. Maier and A. Saupe, *Eine einfache molekular-statistische Theorie der nematischen kristallinflüssigen Phase.*, Zeitschrift für Naturforschung A **14**, 882 (1959).

[47] G. Luckhurst and C. Zannoni, *Why is the Maier–Saupe theory of nematic liquid crystals so successful?*, Nature **267**, 412 (1977).

[48] B. Cullity and C. Graham, *Introduction to Magnetic Materials* (Wiley, 2009).

[49] D. Allender and L. Longa, *Landau–de Gennes theory of biaxial nematics reexamined*, Physical Review E **78**, 011704 (2008).

[50] J. L. Ericksen, *Anisotropic fluids*, Archive for Rational Mechanics and Analysis **4**, 231 (1959).

[51] J. Ericksen, *Inequalities in liquid crystal theory*, The Physics of Fluids **9**, 1205 (1966).

[52] F. M. Leslie, *Some constitutive equations for anisotropic fluids*, The Quarterly Journal of Mechanics and Applied Mathematics **19**, 357 (1966).

[53] F. M. Leslie, *Some constitutive equations for liquid crystals*, Archive for Rational Mechanics and Analysis **28**, 265 (1968).

[54] C. Oseen, *The theory of liquid crystals*, Transactions of the Faraday Society **29**, 883 (1933).

[55] H. Zocher, *The effect of a magnetic field on the nematic state*, Transactions of the Faraday Society **29**, 945 (1933).

[56] I. W. Stewart, *The static and dynamic continuum theory of liquid crystals: a mathematical introduction* (CRC Press, 2004).

[57] S. Chandrasekhar, *Liquid crystals* (Cambridge University Press, 1993).

[58] A. N. Beris and B. J. Edwards, *Thermodynamics of flowing systems: with internal microstructure*, 36 (Oxford University Press on Demand, 1994).

[59] M. Miesowicz, *Der Einfluß des magnetischen Feldes auf die Viskosität der Flüssigkeiten in der nematischen Phase*, Bull Acad Pol A 228–247 (1936).

[60] V. Zwetkoff, *Bewegung anisotroper Flussigkeiten im rotierenden Magnetfeld*, Acta Physiochimica, URSS **10**, 555 (1939).

[61] G. Smith and R. S. Rivlin, *The anisotropic tensors*, Quarterly of Applied Mathematics **15**, 308 (1957).

[62] O. Parodi, *Stress tensor for a nematic liquid crystal*, Journal de Physique **31**, 581 (1970).

[63] H. Lodish, A. Berk, S. L. Zipursky, P. Matsudaira, D. Baltimore, J. Darnell, et al., *Molecular cell biology*, vol. 3 (WH Freeman New York, 1995).

[64] T. B. Liverpool and M. C. Marchetti, *Instabilities of isotropic solutions of active polar filaments*, Physical Review Letters **90**, 138102 (2003).

[65] Y. Hatwalne, S. Ramaswamy, M. Rao, and R. A. Simha, *Rheology of active-particle suspensions*, Physical Review Letters **92**, 118101 (2004).

[66] R. Voituriez, J.-F. Joanny, and J. Prost, *Spontaneous flow transition in active polar gels*, EPL (Europhysics Letters) **70**, 404 (2005).

[67] L. Giomi, M. J. Bowick, X. Ma, and M. C. Marchetti, *Defect annihilation and proliferation in active nematics*, Physical review letters **110**, 228101 (2013).

[68] M. C. Marchetti, J.-F. Joanny, S. Ramaswamy, T. B. Liverpool, J. Prost, M. Rao, and R. A. Simha, *Hydrodynamics of soft active matter*, Reviews of Modern Physics **85**, 1143 (2013).

[69] L. Giomi, M. J. Bowick, P. Mishra, R. Sknepnek, and M. C. Marchetti, *Defect dynamics in active nematics*, Phil. Trans. R. Soc. A **372**, 20130365 (2014).

[70] M. Ravnik and J. M. Yeomans, *Confined active nematic flow in cylindrical capillaries*, Physical review letters **110**, 026001 (2013).

[71] S. P. Thampi, R. Golestanian, and J. M. Yeomans, *Instabilities and topological defects in active nematics*, EPL **105** (2014).

[72] A. Doostmohammadi, M. F. Adamer, S. P. Thampi, and J. M. Yeomans, *Stabilization of active matter by flow-vortex lattices and defect ordering*, Nature Communications **7**, 1 (2016).

[73] A. Malevanets and R. Kapral, *Mesoscopic model for solvent dynamics*, Journal of Chemical Physics **110**, 8605 (1999).

[74] T. Ihle and D. Kroll, *Stochastic rotation dynamics: a Galilean-invariant mesoscopic model for fluid flow*, Physical Review E **63**, 020201 (2001).

[75] J. F. Ryder, *Mesoscopic simulations of complex fluids*, Ph.D. thesis, University of Oxford (2005).

[76] G. Gompper, T. Ihle, D. Kroll, and R. Winkler, *Multi-particle collision dynamics: a particle-based mesoscale simulation approach to the hydrodynamics of complex fluids*, in *Advanced computer simulation approaches for soft matter sciences III*, 1–87 (Springer, 2008).

[77] M. Theers, E. Westphal, G. Gompper, and R. G. Winkler, *Modeling a spheroidal microswimmer and cooperative swimming in a narrow slit*, Soft Matter **12**, 7372 (2016).

[78] K. Rahul and S. Bhattacharyya, *One-sided finite-difference approximations suitable for use with richardson extrapolation*, Journal of Computational Physics **219**, 13 (2006).

[79] H. Noguchi and G. Gompper, *Transport coefficients of off-lattice mesoscale-hydrodynamics simulation techniques*, Physical Review E **78**, 016706 (2008).

[80] D. S. Bolintineanu, J. B. Lechman, S. J. Plimpton, and G. S. Grest, *No-slip boundary conditions and forced flow in multiparticle collision dynamics*, Physical Review E **86**, 066703 (2012).

[81] C. Denniston, E. Orlandini, and J. Yeomans, *Lattice boltzmann simulations of liquid crystal hydrodynamics*, Physical Review E **63**, 056702 (2001).

[82] G. Tóth, C. Denniston, and J. Yeomans, *Hydrodynamics of domain growth in nematic liquid crystals*, Physical Review E **67**, 051705 (2003).

[83] N. Kuzuu and M. Doi, *Constitutive equation for nematic liquid crystals under weak velocity gradient derived from a molecular kinetic equation*, Journal of the Physical Society of Japan **52**, 3486 (1983).

[84] M. Doi, *Explanation for the 3.4-power law for viscosity of polymeric liquids on the basis of the tube model*, Journal of Polymer Science: Polymer Physics Edition **21**, 667 (1983).

[85] M. Doi and S. F. Edwards, *The theory of polymer dynamics*, vol. 73 (Oxford University Press, 1988).

[86] L. Tortora and O. D. Lavrentovich, *Chiral symmetry breaking by spatial confinement in tactoidal droplets of lyotropic chromonic liquid crystals*, Proceedings of the National Academy of Sciences **108**, 5163 (2011).

[87] Y.-K. Kim, S. V. Shiyanovskii, and O. D. Lavrentovich, *Morphogenesis of defects and tactoids during isotropic–nematic phase transition in self-assembled lyotropic chromonic liquid crystals*, Journal of Physics: Condensed Matter **25**, 404202 (2013).

[88] S. Zhou, S. V. Shiyanovskii, H.-S. Park, and O. D. Lavrentovich, *Fine structure of the topological defect cores studied for disclinations in lyotropic chromonic liquid crystals*, Nature Communications **8**, 14974 (2017).

Acknowledgments

I would like to express my gratitude to the people who supported me in the process of creating this thesis. To my advisor Dr. Marco G. Mazza for his guidance and comments. To Dr. Shubhadeep Mandal for the stimulating conversations and help. Thanks to my colleagues at university and at the MPI DS. A special thank you to my parents and sister for their continued love and support.

Declaration

I declare that this thesis has been composed solely by myself, no other materials except the ones listed in this thesis were used. This thesis is until now neither handed in nor will it be used to apply for any other degrees. The digital copy received by the registrar's office is identical to the physical version.

Göttingen, February 18, 2019

Joscha Tabet

Chapter A

Appendix

A.1 Macroscopic Responses of Nematic Liquid Crystals

Studying the electric polarizability, the dielectric constant or magnetic response, one finds the same order parameter as the nematic order parameter in eq. (2.14) [27]. The order parameter of the magnetic properties for example can be obtained from the relation between the magnetic field **H**, the magnetic moment **M** and the magnetic susceptibility χ

$$M_i = \chi_{ij} H_j. \tag{A.1}$$

Requiring that the tensor order parameter $\boldsymbol{Q}$ vanishes in the isotropic state yields

$$Q_{ij} \propto \chi_{ij} - \frac{1}{3}\delta_{ij}\chi_{kk}. \tag{A.2}$$

A.2 Computational Grids

Some of the computational grids used for simulations are given here.

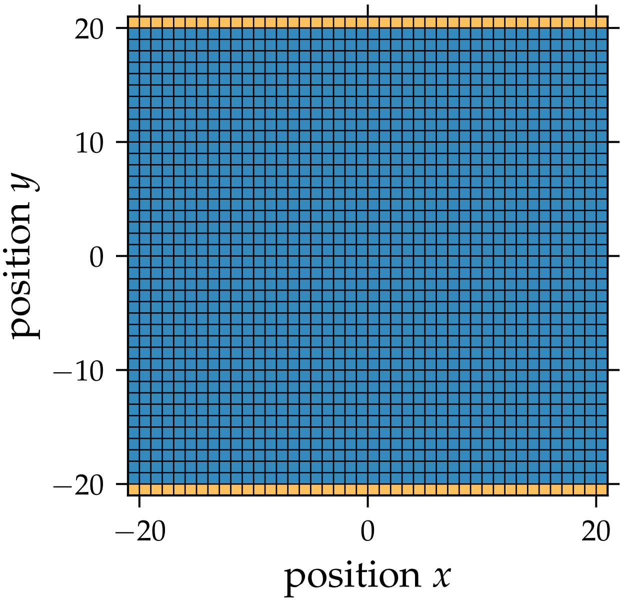

Figure A.1: Computational grid used for Poiseuille flow. The domain of the LC comprises of normal cells (blue), bound by ghost cells (yellow) on one axis. Along the other axes the system is periodic.

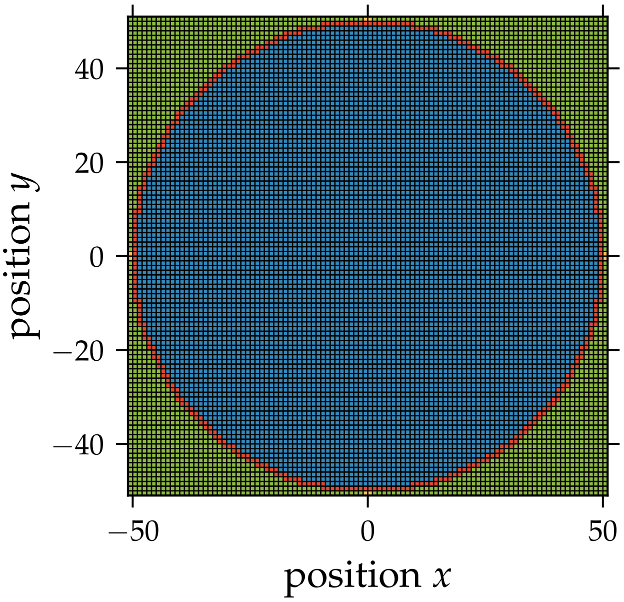

Figure A.2: Computational grid used to simulate a cylindrical compartment. The domain of the LC comprises of normal cells (blue), bound by border cells (red) and ghost cells (yellow). Along the axis perpendicular to the plane of projection the system is periodic after a length of 4 cells.

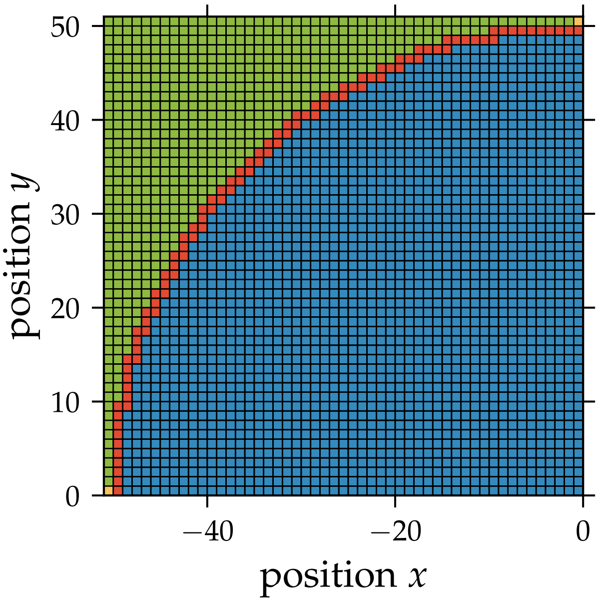

Figure A.3: Zoomed in version of the computational grid used to simulate a cylindrical compartment. The domain of the LC comprises of normal cells (blue), bound by border cells (red) and ghost cells (yellow). Along the axis perpendicular to the plane of projection the system is periodic after a length of 4 cells.

A.3 MPCD-Particle Density

In passive systems we saw a completely homogeneous MPCD-particle distribution. In active systems there was a large variance.

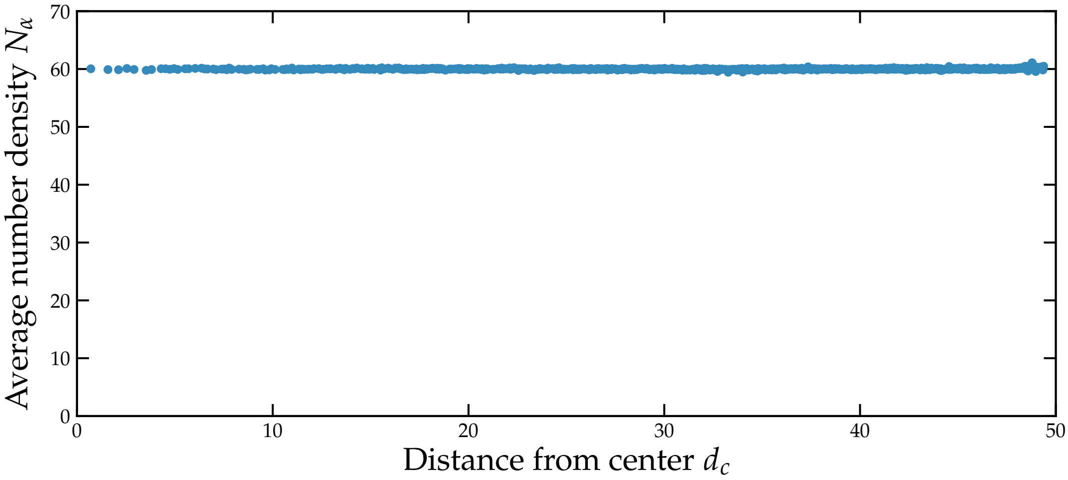

Figure A.4: Average cell number density N_α for passive systems in cylindrical confinement.

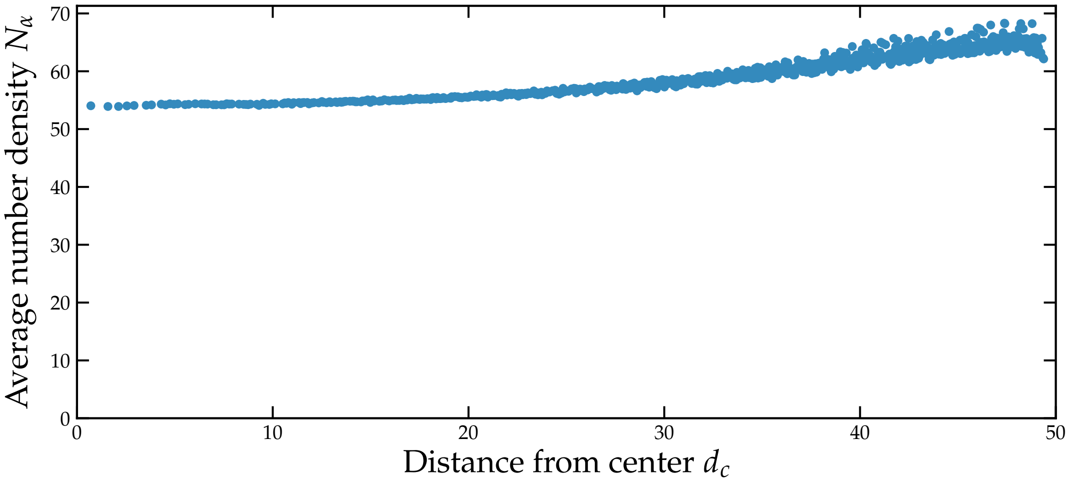

Figure A.5: Average cell number density N_α for circular anchoring at activity $\Lambda = 0.09$.

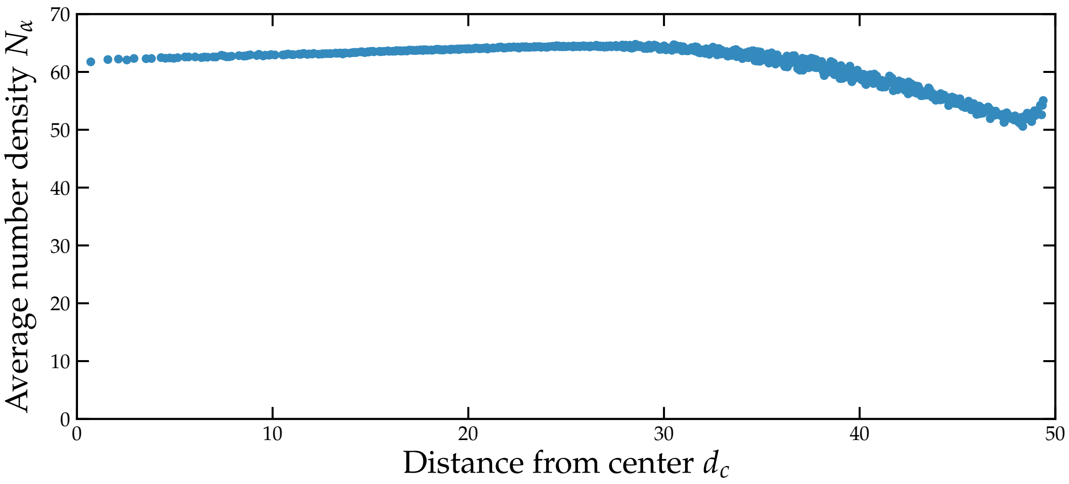

Figure A.6: Average cell number density N_α for radial anchoring at activity $\Lambda = 0.09$.

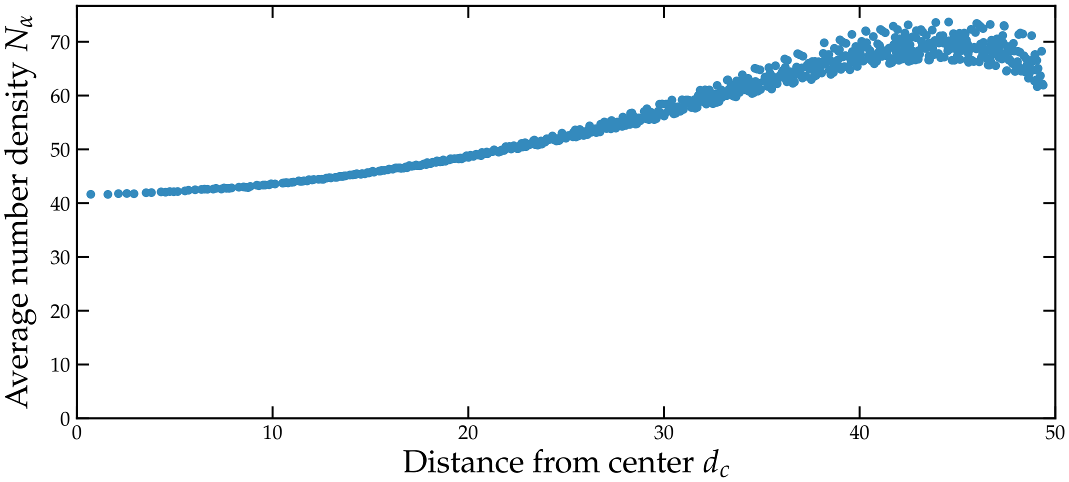

Figure A.7: Average cell number density N_α for tilted anchoring at contractile activity $\Lambda = -0.135$.